Design, analysis and experimental evaluation of a vibration energy generator

JAE de Beer

orcid.org/0000-0002-6630-0079

Dissertation accepted in fulfilment of the requirements for the degree *Master of Engineering in Mechanical Engineering* at the North-West University

Supervisor: Prof M van Eldik

Graduation: August 2023

Student number: 22754105

Abstract

Generating energy from ambient vibration is a method of harvesting green energy. Harvesting energy in this manner is similar to that of solar and wind energy harvesting. The vibration energy generator discussed in this dissertation illustrates a thorough example of a method to harvest green energy and the required components for the design of a vibration energy generator. Through the investigation of the design, and further analysis and experimental evaluation, the technical behaviour of an electromagnetic vibration energy generator is predicted and determined.

The design of a vibration energy harvester is considered in literature - more specifically, the design of an electromagnetic vibration generator. Multitudes of concepts have been published and compared in studies. For the mechanical system in this study, the design of the vibration energy generator is obtained through the use of a subwoofer (loudspeaker).

The mechanical system is studied to determine the typical mechanical properties under varying electrical load. The parameters, for this study, were determined by different methods with aid of mathematical models for characterization and verification.

The electrical components were simply measured and implemented into mathematical models. The electrical properties together with the mechanical properties are incorporated for analysis of the generator in context of the mechanical and electrical response.

The generator design is analysed in the form of mathematical models. Two mathematical models predict the usable electrical power to be harvested at specific load conditions. The usable electrical power is determined from both a mechanical and an electrical perspective. To evaluate the mathematical models, measurements were made to record the usable electrical power from the systems. The measured values under varying electrical loads are compared to the predicted values from the mechanical and electrical models respectively.

To arrive at a design for a vibration energy generator it is essential to address certain design considerations proactively for each specific application, as harmonic tuning and optimal electrical load choice have intricate effects on both the mechanical and electrical systems for performance of the system to produce usable power. Furthermore, it is shown that a loudspeaker can be used as a vibration energy generator. However, changes will be required for use as a vibration energy generator.

Keywords: Generator, Finite Element Analysis, Vibration energy generator, Base excitation, Loudspeaker, Coupling factor, Magnetic induction, electromagnetic harvester.

Samevatting

Die opwekking van energie uit omgewingsvibrasie is 'n metode om groen energie te oes, soortgelyk aan dié van son- en windenergie tegnologie. Die vibrasie-kragopwekker, met die nodige koponente, wat in hierdie artikel bespreek word, is 'n uitstekende voorbeeld van 'n metode om groen energie te oes. Die ontwerp word ondersoek en met verdere analise en eksperimentele evaluering word die tegniese werksverrigting van ‘n elektromagnetiese vibrasie-energieopwekker bepaal.

Die ontwerp van 'n vibrasie-energie oes-eenheid word in literatuur bespreek, met spesifieke fokus op die ontwerp van 'n elektromagnetiese vibrasie-kragopwekker. Menige konsepte is in studies gepubliseer en vergelyk wat vir hierdie studie bestudeer is. In hierdie studie is die ontwerp van die vibrasie-energieopwekker vervolgens gebaseer op die gebruik van 'n luidspreker (“subwoofer”) vir die meganiese stelsel.

Die meganiese stelsel word bestudeer om die tipiese meganiese eienskappe onder wisselende elektriese ladings te bepaal. Die parameters, vir die studie, is volgens verskillende metodes bepaal met behulp van wiskundige modelle vir karakterisering en verifikasie, en daarna vergelyk met vervaardigingspesifikasies. Die elektriese komponente is eenvoudig gemeet en geïmplementeer in wiskundige modelle en met die meganiese komponente geinkorporeer vir die analise van die opwekker in die konteks van meganiese en elektriese reaksies

Die generatorontwerp word geanaliseer deur middel van wiskundige modelle. Twee wiskundige modelle voorspel die bruikbare elektriese krag wat tydens spesifieke vragtoestande geoes word. Die elektriese drywing word bepaal uit beide die meganiese perspektief en die elektriese perspektief. Om die wiskundige modelle te evalueer, is metings geneem om die bruikbare elektriese krag van die stelsel op te teken. Die meetwaardes onder verskillende laste word onderskeidelik met die voorspelde waardes van die meganiese en elektriese modelle vergelyk.

Om 'n ontwerp vir 'n vibrasie-kragopwekker te bepaal, is dit noodsaaklik om sekere ontwerpoorwegings proaktief, vir elke spesifieke toepassing, aan te spreek. Dit is aangesien harmoniese resonansie en optimale elektriese ladingskeuse ingewikkelde effekte op beide die meganiese en elektriese stelsels het vir werkverrigting vir bruikbare krag. Verder word aangetoon dat 'n luidspreker as 'n vibrasie-kragopwekker gebruik kan word. Veranderinge sal egter voordelig wees vir gebruik as 'n vibrasie-kragopwekker

Sleutelwoorde: Generator, eindige elementanalise, vibrasie-energie-generator, basis-opwekking, luidspreker, koppelfaktor, magnetiese induksie, elektromagnetiese oes-eenheid.

Table of contents

List of figures

List of tables

Nomenclature

Capital letters

$\vec{A}$	Area vector perpendicular to differential Area dA	m^2
A	Area enclosed a conductor loop	m^2
$\vec{B}$	Magnetic field vector	T
B	Magnetic field strength magnitude	T
BL	Force / coupling factor	Tm
C_{ms}	Compliance of a speaker	$\frac{m}{N}$
F	Applied force	N
$F_{m,k,c,in}$	Dynamic forces at mechanical components	N
F_e	Excitation motors resultant force	N
F_s	Free air resonance of a speaker	Hz
F_0	Excitation force	N
I_s	Induced current in circuit, RMS value	A
$\mathbf{I}_s$	Induced current in circuit with magnetic inductance	A
L	Wire length for Faraday's law	m
L_c	Voice coil inductance	mH
M_{ms}	Moving mass of a speaker	kg
N	Number of turns in a coil	$-$
P	Mechanical power amplitude	W
$P_{m,k,c,in,con}$	Power amplitude at mechanical components	
P_e	Average electrical power amplitude	W
P_{um}	Usable power in mechanical model	W
P_{ue}	Usable power from electrical model	W
P_u	Measured usable power	W

R_c	Coil direct current resistance	Ω
R_l	Electrical load resistance	Ω
R_{ms}	Mechanical resistance of a speaker	$\frac{Ns}{m}$
T_d	Displacement transmissibility	$-$
UB	Unbalance setting at the vibration motors	%
$\mathbf{V}_l$	Voltage across the load resistor R_l	V
V_s	Induced voltage due to magnetic inductance, RMS value	V
$\mathbf{V}_s$	Induced voltage due to magnetic inductance	V
X_b	Steady state displacement amplitude of excitation	m
X_g	Steady state displacement amplitude of generator	m
$X_{g_{before}}$	Plane wave tube response in open circuit	m
$X_{g_{after}}$	Plane wave tube response in closed circuit	m
X_{avg}	Average response, used in characterization	m
$\ddot{X}_b$	Steady state acceleration amplitude of excitation	$\frac{m}{s^2}$
$\ddot{X}_g$	Steady state acceleration amplitude of generator	$\frac{m}{s^2}$
$\ddot{X}_{g1}$	Acceleration amplitude of generator used in characterization	$\frac{m}{s^2}$
$\ddot{X}_{gn+1}$	Second acceleration amplitude used for characterization	$\frac{m}{s^2}$
$\dot{X}_r$	Relative velocity amplitude of generator system to excitation	$\frac{m}{s}$
Z_c	Coil impedance	Ω
Z_t	Total impedance in circuitry	Ω

Lower-case letters

c_{cg}	Critical damping coefficients of generator system	$\frac{Ns}{m}$
c_{be}	Equivalent damping coefficient of excitation system	$\frac{Ns}{m}$
c_{ge}	Equivalent damping coefficient of generator system	$\frac{Ns}{m}$
dt	Change in time	s
dW	Represents the change in work done	J
f_n	Natural frequency	Hz
h_c	Height of voice coil	m
k	Stiffness coefficient of an oscillating body	$\frac{N}{m}$
k_{be}	Equivalent stiffness coefficient of excitation system	$\frac{N}{m}$
k_{ge}	Equivalent stiffness coefficient of generator system	$\frac{N}{m}$
m	Mass of an oscillating body	kg
m_{be}	Equivalent moving mass in excitation system	kg
m_{ge}	Equivalent moving mass in generator system	kg
m_u	Unbalanced mass in excitation motors	kg
n	Integer used in characterization	$-$
$p_{m,k,c,in,con}$	Instantaneous power at mechanical components	W
r	Impedance ratio	$-$
r_c	Radius of a voice coil	m
r_u	Radial position of unbalanced mass m_u	m
t	Represents time	s
dt	Change in time	s
t_1	Time at specific instance $\ddot{X}_{g1}$	s
t_{n+1}	Time at a specific instance $\ddot{X}_{gn+1}$	s

v	Velocity of a conducting loop in Faradays law	$\frac{m}{s}$
x_g	Vertical displacement of generator system	m
x_b	Vertical displacement of base excitation system	m
$\dot{x}$	Velocity of a body	$\frac{m}{s}$
$\dot{x}_g$	Vertical velocity of generator system	$\frac{m}{s}$
$\dot{x}_b$	Vertical velocity of base excitation system	$\frac{m}{s}$
$\ddot{x}_g$	Vertical acceleration of generator system	$\frac{m}{s^2}$
$\ddot{x}_b$	Vertical acceleration of excitation system	$\frac{m}{s^2}$
x_r	Relative displacement of generator system and excitation system	m
$\dot{x}_r$	Relative velocity of generator system and excitation system	$\frac{m}{s}$

Greek symbols

ω_d	Damped frequency, used for characterization	rad/s
τ_d	Periodic time of damped free vibration	s
ω_n	Natural frequency	rad/s
ω_o	Forced frequency	rad/s
ϕ	Phase angle between displacement vectors X_g and X_b	rad
ξ	Induced electromotive force	V
Φ	Magnetic flux	Wb
π	Pi constant	$-$
ζ_g	Damping ratio of generator system	$-$
ζ_{mec}	Damping ratio of generator system mechanical component	$-$
ζ_{ele}	Damping ratio of generator system electrical component	$-$
θ_i	Phase of induced current I_s	$degrees$
θ_v	Phase of induced voltage V_s	$degrees$
μ_0	Air permeability	H/m

Abbreviations

AC	Alternating Current
BCE	Before Common Era
DC	Direct Current
FEA	Finite Element Analysis
FEM	Finite Element Method
FFT	Fast Fourier Transform
FEMM	Finite Element Method Magnetics
IEEE	Institute of Electrical and Electronic Engineers
IMPP	Injection-Moulded Poly Propylene
ISO	International Standards Organisation
IOT	Internet of things
IRENA	International Renewable Energy Agency
LEDS	Light Emitting Diodes
MEMS	Micro-Electro-Mechanical System
RMS	Root Mean Squared
SECE	Synchronous Electric Charge Extraction
SMFE	Synchronous Magnetic Flux Extraction

Chapter 1 Introduction and literature review

1.1 Aim and relevance

1.1.1 Aim

The aim of the dissertation is the design, analysis and experimental evaluation of a vibration energy generator, as captured in the title, with three specific tasks as outlined below and as described in the detailed problem statement as formulated in Chapter 1.

- *Design:* Identify the structures and features that constitute a typical vibration energy generator.
- *Analysis:* Through mathematical models, analyse the typical behaviour of a vibration energy generator.
- *Experimental evaluation:* Use experimental methods to evaluate the mathematical models used for analysis of a vibration energy generator.

1.1.2 Relevance

This dissertation is relevant and of importance with regards to two primary aspects and it will have worldwide implications. First implication is the modern socio-political drive toward green energy solutions. Second is the possible commercial application, and financial reward for this type of technology in the foreseeable future. The anticipated application is underpinned by the transition to sustainable energy. More so, this technology provides an alternative source of energy. Most obvious use of the vibration energy generator is applicable in the category of digital technology, more specifically in the internet of things (IOT) as listed by the International Renewable Energy Agency (IRENA, 2019).

1.2 Literature review

1.2.1 Introduction

Vibration energy harvesters transform vibration energy into usable electrical energy. Alternatively, a machine that produces electrical energy is referred to as an electrical generator. Extensive research has been documented in literature to understand the design, analysis and dynamic behaviour of a vibration energy harvester as an electrical generator. The available literature review is structured according to, the function and application, mechanical and electrical design and analysis, and experimental evaluation of a vibration energy generator. Furthermore, the literature review includes typical instrumentation used in relevant experimentation and analysis. Lastly, literature contains details regarding the design and characterization of a loudspeaker that could be used as a vibration energy generator.

1.2.2 Function and application

An electrical vibration generator, also known as a vibration energy harvester, is a mechanism that converts vibration energy into electrical energy (Wei & Jing, 2017). Utilizing relative motion, electrical energy is produced using transducers, of which the most common are electromagnetic, electrostatic and piezoelectric transducers (Mitcheson *et al.*, 2008). These transducers primarily determine the function and application.

MEMS (micro-electro-mechanical systems) is the most prominent application for vibration energy harvesters, as is typically used in wireless sensor networking. Other portable electronic devices can be identified to replace their batteries by use of a feasibility study as proposed by Mitcheson *et al.* (2004). Four factors determine the feasibility: typical power consumption, usage pattern, device size and motion of the device (Mitcheson *et al.*, 2008).

Comparatively the different transducers have varying attributes and application. Piezoelectric material is expensive and fragile. However, due to its simple structure, the material is easily installed and can be manufactured in very small sizes. The piezoelectric material is better suited for high frequency applications (Cepnik *et al.*, 2013). An example of the application of the piezoelectric transducer is in intelligent tyre sensor modules. Singh *et al.* (2012) assessed the feasibility of a battery-less power supply unit in the realisation of an intelligent tyre concept.

Electrostatic transducers are compatible with MEMS and do not require smart, and expensive materials. As an example, Ichikawa & Hijikata (2019) illustrates the possibility of an electrostatic generator in a mouthguard to power sensors that monitor healthcare-related parameters. Disappointedly, electrostatic generators have a small energy density compared to other transducers such as the electromagnetic transducer. Furthermore, electrostatic transducers require an external voltage source which is another downside to using electrostatic transducers in a vibration energy generator (Wei & Jing, 2017).

The electromagnetic transducer shows comparatively high energy densities and low cost of manufacturing. The electromagnetic transducer structure becomes complex when downsizing for limited space. Furthermore, the electromagnetic transducer can be affected by electromagnetics which makes it difficult to integrate with MEMS (Poulin *et al.*, 2004; Wang *et al.*, 2015). An example where this type of transducer is used, is reported by Shahhaidar *et al.* (2015). The transducer is used in an application of an electromagnetic harvester and biosensor to continually measure the respirator function of a subject.

1.2.3 Mechanical design features and analysis

1.2.3.1 Mechanical components

The mechanical design pertains to the mechanical structures with dynamic properties such as springs and viscous damper components. The mechanical components enable relative motion required for

energy harvesting. The mechanical components, mass, stiffness and damping are prevalent in the designs discussed in the survey by Naifar *et al.* (2017). In their survey, the different electromagnetic harvesters are grouped in four different architectures: cantilever spring, linear mechanical spring, spiral spring and magnetic spring (Naifar *et al.*, 2017). The mechanical components are representative of structures that consist of different shapes, sizes and materials (De Silva, 2000; Den Hartog, 1985; Inman & Singh, 2014; Kelly, 2012; Rao, 2011). The variety in designs are clear in the classification approach by Cepnik *et al.* (2013). Who attempts to group several energy harvesters. The challenge to design an electromagnetic vibration energy harvester is to compete with other transducers in downsizing. More specifically, there are limits as to the required architecture for an effective coupling coefficient and the viability of manufacturing (Mitcheson *et al.*, 2008).

The mechanical structures reported in study aforementioned are primarily of the single degree of freedom. However, a study by Tang and Zuo (2011) investigates the benefits of a dual-mass structure analytically. The results of the study suggest conditions for operating at optimum harvesting rates and that harvesting power improves significantly with use of a dual-mass structure.

1.2.3.2 Natural frequency and resonance

Since the mechanical structures have the dynamic components described above, an important mechanical design criteria to consider is operation at resonance (Ashraf *et al.*, 2013; Liu *et al.*, 2021; Tang & Zuo, 2011; Yildirim *et al.*, 2017). Maximum power is harvested when the excitation frequency is the same as the natural frequency. The natural frequency is the undamped natural frequency (Stephen, 2006). Yildirim *et al.* (2017) propose resonance tuning techniques - either effectively changing the mass in the system or alternatively changing the effective stiffness. In accordance with the equation

$$\omega_n = \sqrt{\frac{k}{m}} \tag{1.1}$$

Cammarano *et al.* (2010) shows that it is possible to tune a vibration energy harvester with a generalised electrical load, instead of using the proposed method of tuning by Yildirim *et al.* (2017). It is not necessary to change the mechanical system mass or stiffness (Cammarano *et al.*, 2010).

Due to the nature of materials and the consideration to operate at resonance, it is important to understand amplitude dependency. Amplitude dependency is a phenomenon commonly seen in rubber mounts (Austrell & Olsson, 2012). It describes the dynamic properties that are dependent upon the operating amplitude (Lin *et al.*, 2005; Nel & Van Wyngaardt, 2014). These dynamic properties are directly related to the operation condition of resonance for maximum power as discussed by French (1971). The importance of operation at resonance with consideration of amplitude dependency is enforced by the experimentally validated electromagnetic energy harvester by Elvin and Elvin (2011).

1.2.3.3 Power

The power absorbed by a dynamic mechanical system is discussed at length in the book *Vibrations and waves* by A.P. French. French (1971) shows the calculation for average power of an oscillating body and illustrates that the maximum power is at resonance, dissipated through the damping element only. Stephen (2006) demonstrates theory on calculating the power consumed by a mechanical dynamic system in a variety of applications, as in the case of a single degree of freedom base excited system.

1.2.3.4 Damping

Damping is the phenomenon by which vibrational energy is dissipated, commonly in the form of heat, sound, fluid motion, friction at contacting surfaces, or other mechanisms (Rao, 2011; Schmitz & Smith, 2012). The response of a free vibrating system gradually decreases due to the dissipation of energy. To accurately predict the vibration response of a dynamic system, a suitable damping model must represent the associated energy dissipation. To address damping is difficult, with most uncertainty in vibration analysis and structural dynamics, because its physical origins have a large variety and complexity (Inman & Singh, 2014; Kelly, 2012).

The common models to represent the damping in practical systems are viscous damping, Coulomb or dry friction damping, material or solid or hysteretic damping. The damping force that is associated with the decaying motion is represented by a damper and is assumed to have neither mass nor elasticity. Furthermore, the damping force is only perceived given the relative velocity between the two ends of the damper component (Rao, 2011; Schmitz & Smith, 2012; Inman & Singh, 2014; Kelly, 2012).

Viscous damping is typically encountered when a mechanical system vibrates in a fluid medium. The damping force is proportional to the velocity of the vibrating body. Coulomb damping is due to dry sliding or friction between two surfaces. The damping force, in the case of Coulomb damping, is constant in magnitude but always in the opposing direction of motion. Material damping occurs due to material deformation. Material damping energy is dissipated due to the damping force and is represented by the area within the hysteresis loop that is inherent to the phenomenon. Other forms of damping such as aerodynamic drag, radiation damping and anelastic damping exist, gives rise to non-linear terms in the governing differential equations. Dynamic systems with these forms of damping present can be approximated with an equivalent viscous damping coefficient as proposed by Kelly (2012), Rao (2011) and De Silva (2000).

Methods to measure damping to be represented as an equivalent damping coefficient in the governing equations are generally grouped into either time-response methods or frequency-response methods. The time-response methods include the logarithmic decrement method, step-response method and the hysteresis loop method. The frequency-response method includes the magnification factor method, bandwidth method and the Nyquist plot that is normally used in modal analysis (De Silva, 2000).

The methods of measuring damping as an equivalent damping coefficient are open to uncertainty. For example with the logarithmic decrement method, the damping estimate uncertainty is dependent on the standard uncertainties in the measurement of the peak points in the decaying time single (Schmitz & Smith, 2012). In practice, to apply the aforementioned techniques, the approximation of equivalent viscous damping for a dynamic system has certain disadvantages.

The comparison of equivalent viscous damping and nonlinear damping in discrete and continuous vibrating systems was investigated by Bandstra (1981). Bandstra (1981) reports four basic concerns, starting with the equivalent viscous method that underpredicts both the steady state amplitude and dissipated energy per cycle in forced vibration. Secondly, the decay in transient vibrations have different shapes in comparison to the equivalent viscous damping, Coulomb damping, displacement squared and solid damping. Thirdly, the damped natural frequency is different on the two cases of equivalent and nonlinear damping, albeit with a small difference. Fourthly, the frequency at which a correlation between the equivalent viscous damping and nonlinear damping is evaluated plays a significant role. The correlation becomes less accurate the closer the forcing frequency is to the natural frequency due to the dynamic amplification where damping is of importance (Bandstra, 1981).

The justification to use an equivalent viscous damping model is shown in the accurate approximation to the actual nonlinear solution at sufficiently small amounts of damping. The significant small amount of damping is in the range of 10-20 percent equivalent viscous damping. Fairly accurate solutions can be obtained by the equivalent viscous damping method for values below 10 percent. Bandstra (1981) advises a conscious decision with reasons grounded in physical reality when choosing a method for damping representation. However, the use of linear models is chosen for reasons of simplicity, cost and understanding and it is accepted in practice in most applications pertaining to damping models. This supports the assertion by Kelly (2012) and Rao (2011) in using the equivalent viscous damping method.

The effect of varying amount of damping on the response and phase of a base excited system is illustrated in Figure 1-1 and Figure 1-2. The figures are reproduced using equations proposed by Rao (2011) showing displacement transmissibility T_d and phase angle changes ϕ. The frequency ratio in Figure 1-1 refers to the simple ratio of the operating frequency to the natural frequency of the system.

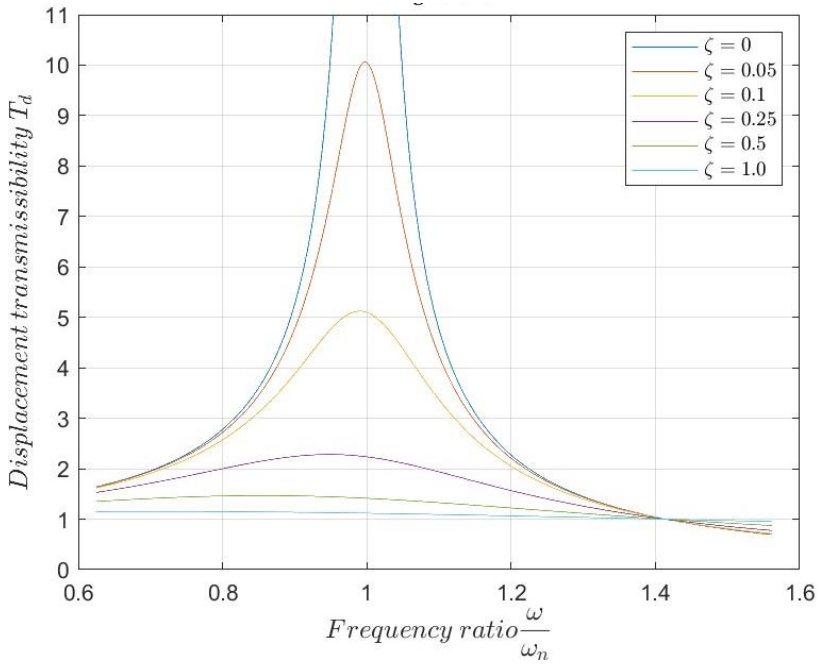

Figure 1-1 Base excited system displacement transmissibility.

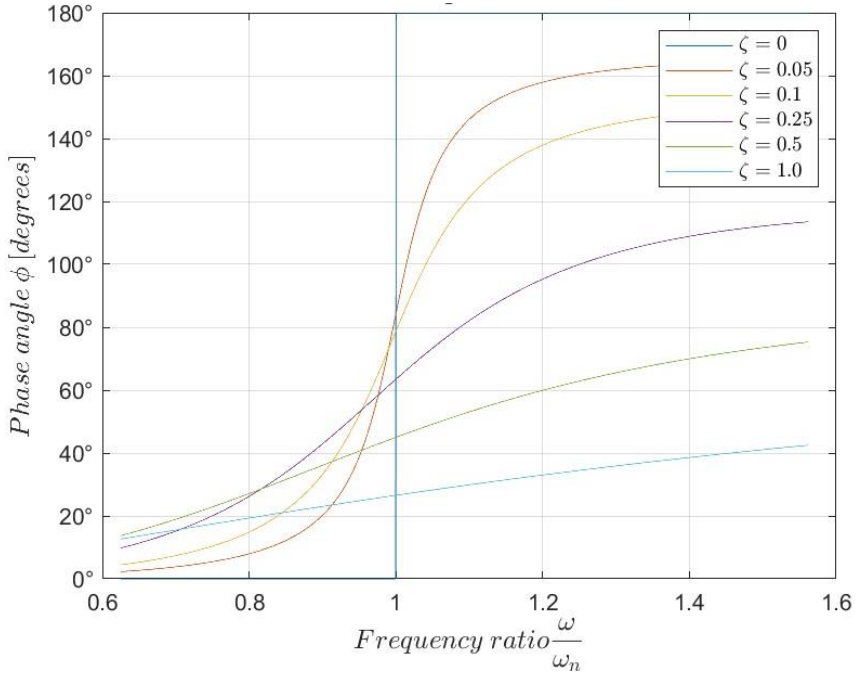

Figure 1-2 Base excited system phase angle

1.2.4 Electrical design features and analysis

In the study of the electrical design of the generator, the concept of electromagnetism and induction is important. The application of electromagnetism and induction is shown in context with linear cyclic motion of a conductor within a magnetic field. The architectures of such a conductor are considered in the discussion of a study completed by Spreemann *et al.* (2008) (discussed later in this paper). The typical model used for analysis is shown with the electrical components. In the model the cyclic induced voltage is shown, achieved through electromagnetic induction.

1.2.4.1 Magnetic material and magnets

Magnetic fields can be created by electric current, flow of electrons, i.e. solenoids, through a wire or by the resultant orbital magnetic dipole moment and spin magnetic dipole moment of electrons in an atom. If all magnetic dipole moments combine vectorially in a material sample to produce a magnetic field, then the material is deemed to be magnetic. Magnetic material is grouped into three general types of magnetism: diamagnetism, paramagnetism and ferromagnetism (Askeland & Wright, 2016; Smith *et al.*, 2011; Walker *et al.*, 2014).

Permanent magnets are generally made from materials that exhibit ferromagnetism and ferrimagnetism. Commercially available permanent magnets are made from materials which are typically named Ferrite/Ceramic, Neodymium, ALNICO and Samarium Cobalt, each with different manufacturing processes and magnetic properties (First4magnets, 2021; HSMAG, 2021a-e; Integrated Magnetics, 2021; Magnetshop, 2021).

Ceramic/ferrite magnets are composed of strontium carbonate and iron oxide. Ceramic/ferrite magnets are manufactured with powder technology techniques and a sintering process (Eclipse Magnetics, 2021a; HSMAG, 2021b; Stanford Magnets, 2021a). Neodymium magnets are comprised of neodymium, which is a member of the rare earth family elements, mixed with primarily iron and boron. The neodymium magnets are also manufactured by a sintering process (Eclipse Magnetics, 2021c; HSMAG, 2021d; Stanford Magnets, 2021d). ALNICO is the acronym for the three primary elements used in the manufacturing of ALNICO magnets. These elements are aluminium, nickel, and cobalt. ALNICO is either manufactured using a casting or a sintering process (Eclipse magnetics, 2021b; HSMAG, 2021e; Stanford magnets, 2021b). The Samarium cobalt magnet was the first rare earth magnet, it was three times stronger than any other magnet at the time, consisting of samarium and cobalt, with traces of iron, copper, and other elements (Eclipse Magnetics, 2021b; First4magnets, 2021; HSMAG, 2021a; HSMAG, 2021c; Integrated Magnetics, 2021; Magnetshop, 2021; Stanford Magnets, 2021b; Askeland & Wright, 2016; Smith *et al.*, 2011).

Each magnet type has advantages and disadvantages in application with regards to operating temperatures and operating conditions. Permanent magnets do lose their magnetisation over time, but the loss is so slow that it is rightly named a permanent magnet. A permanent magnet that is exposed to a polar opposite magnetic field could, however, lose its magnetisation. The coercivity of the material is its ability to withstand demagnetisation in this manner. Permanent magnets exposed to temperatures above the Curie temperature will also lose its magnetisation. Each magnetic material has different coercivity and Curie temperatures. Thus, environmental conditions are criteria for the application of magnets. Due to the different elements and manufacturing processes, the cost by magnets differ by magnetic strength, weight and the type of material used. The magnets are manufactured in a variety of shapes and dimensions. The commercial availability of magnets can be viewed in the referenced websites.

1.2.4.2 Electromagnetism and induction

Hans Christian Oersted coined the terms electromagnetic and electromagnetism in the articles he wrote during 1820 and 1821. These articles were preceded by the article published in July 1820 (Karwatka, 2011), "Experiments on the Effect of the Electric Conflict on the Magnetic Needle" in which he described his discovery that electric current flowing in a wire had an effect on a magnetic needle (Mitolo & Araneo, 2019). This lead to the discovery of electromagnetic induction by Michael Faraday.

Michael Faraday was known as an exceptional experimental scientist. It was during an experiment that he observed electromagnetic induction in a secondary coil in the transient conditions when switching the current on and off. He devised an experiment consisting of two coils that can be moved in such a way to vary the magnetic flux through the secondary coil in a controlled manner to successfully illustrate electromagnetic induction (James, 1991; Mitolo & Araneo, 2019).

Faraday's equation is described in typical physics text books (Walker *et al.*, 2014):

$$\xi = -\frac{d\Phi}{dt} \tag{1.2}$$

$$\Phi = \int \vec{B} \cdot d\vec{A} \tag{1.3}$$

where ξ is the electromagnetic force or more plainly the voltage developed in the loop, and Φ is the magnetic flux through the loop enclosed in an area A. It is better described in the integral of Equation 1-2. $\vec{B}$ represents the magnetic field in unit Tesla. The unit Tesla, is named after Nikola Tesla for his exceptional contributions to the field of electricity and magnetics. Nikola Tesla was the first to invent an induction motor. Rightly so, understanding electromagnetic induction leads to the coupling between the mechanical and electrical systems (Walker *et al.*, 2014) The magnetic coupling is addressed simply in coil induction that follows..

1.2.4.3 Coil induction

The coupling of an energy harvester is obtained from Faraday's law as it pertains to linear cyclic motion of a conductor in a magnetic field. The coupling coefficient is a term that defines the interaction or the interchange of energy from mechanical energy to electrical energy. A simplified example is a conducting loop moving in a uniform magnetic field as illustrated in Figure 1-3. The induced electromotive force ξ measured in volts is given by the product of the magnetic field strength B in unit Tesla, length of conducting wire L in unit meter and the velocity v in unit meter per second of the conducting loop in the magnetic field as in Equation 1-4 (John, 2012).

$$\xi = BLv \tag{1.4}$$

Assuming the loop is closed, it forms an electrical circuit which allows current to flow. This current flow is referred to as the induced current. The induced current creates a magnetic field that acts against the uniform field and can be seen as a force such that it opposes the direction of motion (Walker *et al.*, 2014).

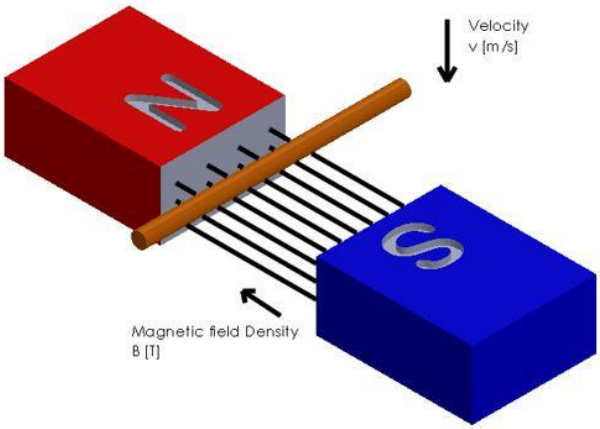

Figure 1-3 Illustration of induction.

The coupling factor is primarily determined by the architecture of the coil and magnetic field. Preceding the study of Challa *et al.* (2013), Spreemann *et al.* (2008) investigated the comparative performance in voltage output and power output of different architectures of a conducting wire loop in a magnetic field. It was shown for the variety of architectures that two different optima exist for voltage and power output, respectively. More generally with correct architectural choice under optimized conditions, one could increase the generated voltage two-fold and the power output three-fold. This study of Spreemann *et al.* (2008) primarily focused on the orientation of the magnetic field to the coil and the relative motion of the

two. The study completed by Spreemann *et al.* (2008), however, only address the architecture in terms of electrical goals. Practically the coil and magnetic field requires a mechanical system that can act dynamically with vibrations for harvesting (Spreemann *et al.*, 2008).

The wide variety of architecture types addressed in the review done by Cepnik *et al.* (2013) shows a design of mostly a moving magnet or a moving coil. The advantages and disadvantages of the different designs are not clearly discussed in terms of a moving magnet or moving coil. The advantages and disadvantages only become prevalent when looking at design considerations like component size, fabrication and wire bonding (Cepnik *et al.*, 2013).

1.2.4.4 Performance metrics

To determine the architectural design success of an energy harvester, different performance metrics or figures of merit have been developed. The ratio of electrical power output to mechanical power input, equals power efficiency. However, this method neglects that the input mechanical power is dependent on the design of the device. The potential mechanical power available from the source cannot be used instead because this is effectively limitless. This is evident as the harvester has negligible effect on the source. Mitcheson *et al.*, (2004) mention other metrics than efficiency that have been developed, Cao *et al.* (2007) looks at power density, Beeby *et al.* (2007) propose a normalized power density and Roundy (2005) proposes a measure of effectiveness.

After discussion of the advantages and disadvantages of each method, Mitcheson *et al.* (2008) propose an alternative definition for harvester effectiveness and the ratio of useful power output to maximum possible power output. Together with the variant of volume figure of merit FoMv, different designs with proof mass density and geometry can be compared as a function of their overall size. Mitcheson *et al.* (2008) conclude that larger devices achieve highest values of effectiveness using the alternative harvester effectiveness metric (Mitcheson *et al.*, 2008).

Challa *et al*. (2013) show the importance of the coupling strength in a study that is validated experimentally. The dimensionless design parameter is shown to determine the performance of power generation in electrodynamic vibration energy harvesters, proposing that a high coupling strength is the best for maximum device efficiency (Wang *et al.*, 2016).

Given the discussion on efficiency, Challa *et al.* (2013) and Hendijanizadeh *et al.* (2013) use a device efficiency defined by real electrical power to the load divided by the mechanical power absorbed by the harvester, which is highly dependent on the coupling of the system. They show the maximum efficiency for a linear vibration harvester to be 50%. Hendijanizadeh *et al.* (2013) go on to compare linear and rotation devices, showing that rotational devices could achieve efficiencies above 50% in favourable conditions. Furthermore, the studies show that the maximum output power is not at the maximum

efficiency point for linear devices. However, for rotational systems the maximum power is at the maximum efficiency point (Challa *et al.*, 2013; Hendijanizadeh *et al.*, 2013).

1.2.4.5 Electrical circuit and components

A method for modelling the equivalent electrical circuit of a generator is represented in Figure 1-4. The equivalent circuit contains an inductor L_c, DC (direct current) resistance R_c and a load resistor R_l (Joyce *et al.*, 2014; Von Büren & Tröster, 2007). Several of the experimentally evaluated vibration harvesters only report a load resistor of a purely resistive component. The resistive load component is used to evaluate the power extracted from the vibration source (Wang *et al.*, 2015).

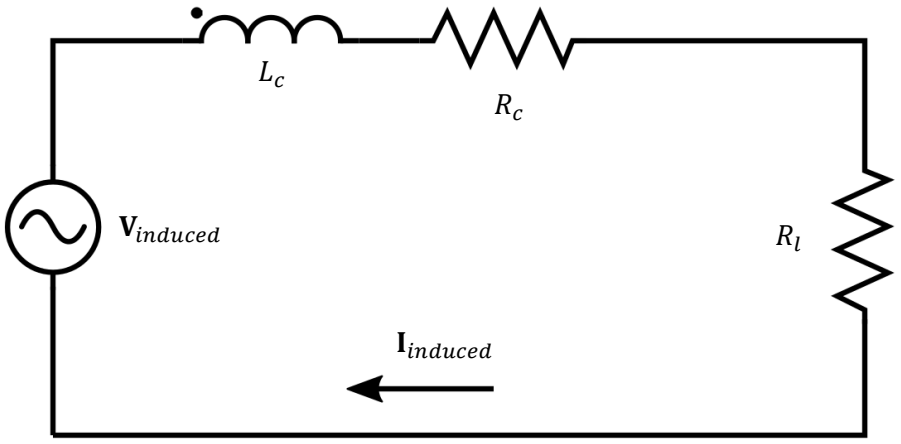

Figure 1-4 Equivalent electrical circuit of a generator.

Further study in complex electrical circuits lead to Arroyo and Badel (2011) who proposes a circuit named SMFE (synchronous magnetic flux extraction). With this circuit it is predicted to harvest 2.5 times more energy. The SMFE is a harvesting technique that is adapted for electromagnetic generators. The SMFE was adapted from the SECE (synchronous electric charge extraction) technique used for piezoelectric generators (Arroyo & Badel, 2011).

Another example of a complex circuit for microgeneration was studied by Dayal *et al.* (2011), who utilised a single-stage AC-DC converter for power processing. Implementing the converter not only boosts the low AC (alternating current) voltage to a nominal DC (direct current) voltage that is mostly required by electronic equipment, but the simple converter allows for a compact system as well (Dayal *et al.*, 2011).

Different load resistors have been implemented in the experimental design of a vibration energy harvester. For example, Joyce *et al.* (2014) used a 48 Ω load resistor and Von Büren and Tröster (2007) used a 10 $k\Omega$ resistor. However, Ashraf *et al.* (2013) report that matching the load impedance with the equivalent impedance of the coil and mechanical impedance, delivers maximum power to the load.

Yildirim *et al.* (2017) support the impedance matching technique for the performance enhancements to harvest from ambient vibrations. Furthermore, the concept of impedance matching is well known in general electric theory (Nilsson & Riedel, 2020).

1.2.4.6 Inductance

Models developed for vibration energy harvesters mostly neglect the effects of coil reactance. It is motivated by the low operating frequencies and that the reactance is relatively small compared to the contributing resistance of the coil (Dayal *et al.*, 2011; Elvin & Elvin, 2011; Hendijanizadeh *et al.*, 2013; John, 2012; Khan & Izhar, 2016; Mitcheson *et al.*, 2004; Nilsson & Riedel, 2020; Spreemann *et al.*, 2008; Xuezheng *et al.*, 2013). In the case that it is not negligible, Cammarano *et al.* (2010) proposes to counteract the effects of the coil inductance by inserting a capacitor in series (Cammarano *et al.*, 2010). Other models calculate the inductance of a coil by using Equation 1-5 and 1-6 where μ_0 is the air permeability, N the number of wire turns, r_c the radius of the coil and h_c the height of the coil (Poulin *et al.*, 2004; Wei & Jing, 2017).

$$L_c = \mu_0 N^2 \pi r_c^2 / h_c \tag{1.5}$$

Furthermore, the operating frequency ω_o is used to calculate the coil impedance:

$$Z_c = \sqrt{R_c^2 + (\omega_o L_c)^2} \angle \arctan\left(\frac{R_c}{\omega_o L_c}\right) \tag{1.6}$$

1.2.5 Experimental evaluation examples

Several experimental values of power harvested from a vibration source was reported, of which the most relevant is highlighted in this section. Salim *et al.* (2016) measured $710\ \mu W$ at $34 - 40\ Hz$ in a low frequency hybrid harvester with ring magnets. Using a magnet and coil array, Zhang and Kim (2014) measured $263\ mW$ at $65\ HZ$. In a second paper looking at flexible coils and a magnetic spring, Zhang *et al.* (2015) report a power output of $4.3\ mW$ at $5.5\ Hz$. In the application to monitor wind turbine blades Joyce *et al.* (2014) produced $80\ mW$ at $2.5\ Hz$. In a study to determine the role of coupling strength, Challa *et al.* (2013) recorded $1.06\ mW$ at $28.1\ Hz$. Liu *et al.* (2021) harvested $18\ W$ at $2\ Hz$ in the application of an energy harvesting backpack. During the survey of low frequency excited vibration energy harvesters, Naifer *et al*. (2017) showed that power harvested is mostly in the mW range.

1.2.6 Instrumentation

Vibrations were first discovered in the form of sound, that was created by musical instruments, as long ago as 4000 BCE (Before Common Era). Later, Galileo discussed vibrating bodies in *Discourses Concerning Two New Sciences* in 1638. In his publication, Galileo discusses frequency dependency of the vibration from a simple pendulum and the phenomenon of sympathetic vibrations known as resonance in modern time (Rao, 2011).

Since the time of Galileo and his predecessors the definition of a vibration has taken a specific form: A vibration or oscillation is any motion that is repetitive within a time interval. In the repetitive motion there is an alternating transfer of energy between kinetic and potential energy. Some energy is dissipated if there is damping present in the system (Inman & Singh, 2014; Kelly, 2012).

The effects of vibrations can be visible, tangible, and audible, and sometimes detected by the human senses. However, more often, the vibration cannot be detected or quantified, nor can the severity be determined by human senses. Instrumentation for vibration measurement offer improvement to measure vibrations and overcome the human limitation. The instrumentation mainly consists of different types of transducers as well as FFT (fast Fourier transform) data collectors and real-time spectrum analysers (Nel & Wyngaardt, 2014, De Silva, 2000; Den Hartog, 1985).

The use of instrumentation varies greatly, depending on the application. To illustrate this remark, Yu *et al.* (2011) uses four PCB Piezotronics pressure transducers and an MTI Instruments laser displacement sensor, to monitor the dynamic characteristics of a loudspeaker. All measurements taken by the transducer and laser were recorded directly using a computer acquisition card (Yu *et al*., 2011).

More so, Verma and Li (2003) presents a laboratory technique to measure resonant frequencies, vibrations and noise, in a paper, for measurement of vibration and radiated acoustic noise of electrical machines. The technique proposed by Verma and Li (2003) uses accelerometers, microphones and search coils in accordance with ISO and IEEE standards.

Rahman and Kok (2011) make use of the 3-dimensional wireless accelerometer node G-Link in harmony with the ADXL 321 accelerometer. However, the latter was merely used for calibration purposes. The G-Link was used in the search for useful ambient vibration sources in a variety of locations such as moving vehicles and household electronics (Rahman & Kok, 2011).

Van Niekerk *et al.* (2000) studied the vibration levels humans are exposed to in the South African mining industry. They studied hand-transmitted vibrations and whole-body vibrations. To measure the whole-body vibrations of a seated operator a seat pad with tri-axial accelerometer was employed as defined in ISO 2631-1 (Van Niekerk *et al.*, 2000).

Nel and Wyngaardt (2014) designed a dynamic vibration absorber for a motor pump that was very close to pure resonance. Utilising a CTC acceleration meter coupled to a diagnostics instrument 2200 FFT, Nel and Wyngaardt (2014a) were able to measure time and frequency domain signals (Nel & Wyngaardt, 2014a).

No matter the variety of instrumentation, the measurement scheme can be compared to the basic vibration measurement scheme as proposed in Rao (2011). The measurement scheme is a flow chart that starts with the motion of the vibrating body that is converted to an electrical signal via the vibration

transducer. The small output signal from the transducer is amplified by a signal conversion instrument. The amplified signal can then be displayed or recorded after which the data can then be analysed (Rao, 2011).

1.2.7 Loudspeaker design and analysis

Loudspeakers are commercially available electromagnetic motors that are used to produce sound. The motion is reciprocal, driven by an amplifier that supplies the current. This is the opposite side of the coin in respect to electromagnetic induction used for energy harvesting. By mechanically exciting the speaker diaphragm, a voltage will be generated across the terminals of the coil on the basis of Faraday's law as described earlier (Dickason, 2007; Eargle, 2002; Kinsler *et al.*, 1982).

There are a few different architectural configurations used in a loudspeaker design. Only a specific design is addressed in this study. A schematic drawing of the cross section of the speaker used in this study is shown and labelled in Figure 1-5.

The dynamic system of the speaker is represented by the Aramid fibre interlaced IMPP cone together with the copper coil wrapped around the aluminium voice coil former as the effective moving mass. The meta-aramid fibre spider is the effective stiffness element that supports the moving mass.

The electromagnetic coupling is created by the magnetic field inside the air gap where the voice coil would translate to-and-fro. The magnetic field and air gap is formed by the top plate and yoke saturated with magnetic flux from the permanent ring magnets (Marinescu *et al.*, 2016).

The industry has developed the Thiele small parameters for performance comparison between products. The relevant Thiele small parameters for this study are tabulated below with their respective units of measure.

Table 1-1 Thiele small parameters

Parameter	Symbol	Units
Voice coil DC resistance	R_c	Ω
Voice coil Inductance	L_c	mH
Force factor/ coupling factor	BL	Tm
Moving mass	M_{ms}	kg
Free-air resonance	F_s	Hz
Compliance of driver	C_{ms}	m/N
Mechanical resistance	R_{ms}	Ns/m

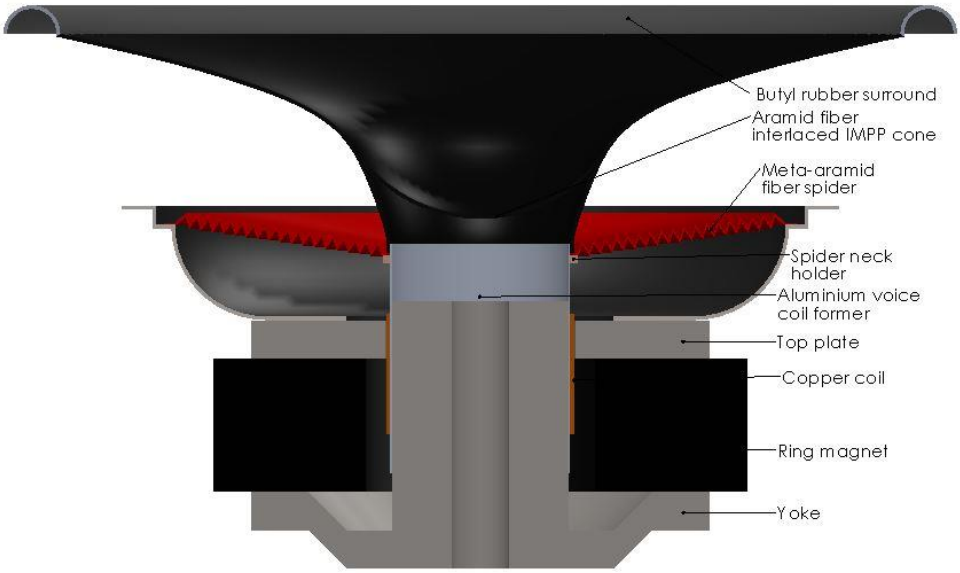

Figure 1-5 Labelled dissection of a loudspeaker

Loudspeakers have been extensively studied to optimise the parameters to produce maximum energy transfer from electrical to sound energy. Klippel (2018) reports several methods and design criteria to maximize the efficiency in active loudspeakers systems. Specific attention is drawn to the gap-coil topology. This pertains to the gap depth, coil height and coil material. The design to optimise the magnetic circuit can be done with finite element analysis (Marinescu *et al.*, 2016).

The measurement of the Thiele small parameters is thoroughly discussed in the *Loudspeaker design cookbook* by Dickason (2007). Several alternative methods are proposed by different authors (Anderson & Leishman, 2003; Moreno, 1991; Tsai *et al.*, 2013). The measuring instruments include laser velocity transducers and a signal analyser or a plane wave tube with relevant equipment to measure the response of the diaphragm of the loudspeaker and pressure change on either side of the diaphragm.

The plane wave tube technique can be used to characterise a loudspeaker for the application of a linear alternator as a thermoacoustic electrical generator. The characterised loudspeaker can be used in the application of an electricity generator and a linear model is useful to predict the behaviour of such an electrical generator (Yu *et al.*, 2011).

1.2.8 Plane wave tube

Anderson et al discusses the use of the plane wave tube, as apparatus, for an acoustical measurement method. The method derives the parameters of a loudspeaker. Further ASTM and AES standards are available for the use of a plane wave tube. The method requires the use of an impedance tube, the use of the two-microphone method and a digital frequency analysis system. The AES freely documents the design practice with regards to usable bandwidth, tube assembly and measurement practice. (Audio Engineering Society, Inc. ,1991; ASTM-E1050, 2019)

Due to the lack of equipment the two-microphone method is replaced by an accelerometer that is mounted on the diaphragm. This reduces the possibility to determine many parameters. In the determination for mechanical resistance R_{ms} a known pressure difference across the diaphragm is required. The known pressure difference is related to the force acting on the system. The force acting on the system is required to complete the calculation. Some parameter can still be determined without the pressure measurements obtained by the two-microphone method. The coupling factor BL, the natural frequency F_s and the compliance of the driver C_{ms} are parameters that can be determined utilizing only the accelerometer.

1.3 Problem statement

In order to arrive at the design of a vibration energy generator, an investigation must be done to understand the technical behaviour thereof. Firstly, an electrical approach should reveal the relevant electrical alternating properties including the power generated. This should be done for the generator subjected to different cyclic loading conditions. A mathematical model for this electrical approach should be developed and implemented in a computer program to allow for predictions to be made for usable power. This should be done for certain input characteristics provided. In addition, a Finite Element Model should be constructed to also allow predictions for certain input characteristics. The results obtained from the computer program based on the mathematical model should be compared to corresponding data obtained from the Finite Element Model. These theoretical models should be experimentally evaluated.

Secondly a mechanical approach should reveal the relevant mechanical properties including the power transmitted to the different mechanical components and the power consumed. This should be done for the generator subjected to different cyclic loading conditions. These conditions are influenced by the different forced frequencies where structural resonance at the generator is also included. The different properties of the mechanical components must be characterised using a feasible experimental procedure. A mathematical model for this mechanical approach should be developed and implemented in a computer program to allow the construction of these power signals. This should be done for the different loading conditions and measured mechanical component characteristics provided. The different electrical power magnitudes should then be compared to the corresponding mechanical power magnitudes.

1.4 Study demarcation

1.4.1 Mechanical

The study is demarcated with certain boundaries with regards to the mechanical systems present. The boundaries of concern are that of linear versus nonlinear vibrations and model development of the excitation system and generator system.

Linear vibrations are assumed for ease of calculation as the analytical tools and mathematical models are well developed and known. The assumption will remain relevant within the parameters as proposed by Banstra (1981), who refers specifically to a mathematical model for damping as discussed in paragraph 1.2.3.4.

The dynamic response of the excitation system is only of concern for a controlled vibration source on which the evaluation of the generator system can be performed. The excitation system is designed with a shaker bench test principle in mind. The operation frequency of the generator system is far above the

bounce mode of the excitation system and far below any structural modes. The displacement transmissibility curve in Figure 1-1 is used to illustrate a principle, that greater the frequency ratio, the less the displacement transmitted. This permits the systems to be modelled as two separate single degree models. One with a fixed base and an the other with an oscillating base. Therefore, a two degrees of freedom model is not considered for the excitation system and generator system together. This ensures that this study focuses on the generator system as a vibration energy generator that is placed on any suitable vibration source.

1.4.2 Electrical

The demarcation of the electrical system and the model thereof is primarily to validate the usable power values predicted by the model of the mechanical system. Therefore, no part of the mechanical system will be modelled in the electrical model even though possible through equivalent circuitry.

Furthermore, the plausible assumption that inductance is negligible is supported by literature and preliminary calculation shown in Chapter 4 during characterization. If inductance of the coil is not negligible, a fix with capacitor is plausible as proposed by Cammarano *et al.* (2010) to maintain simplicity.

1.5 Conclusion

The important aspect of Faraday's law and typical electrical concepts was introduced as it pertains to the design and analysis of a vibration energy generator through an electrical perspective. The mechanical aspects of resonance and amplitude dependency were reviewed as it pertains to the design and analysis of a vibration energy generator through a mechanical perspective. In combination, the parameters and properties of a loudspeaker is shown to be sufficient to utilise the loudspeaker as a vibration energy generator.

Chapter 2 Mathematical models

2.1 Introduction

Mathematical models are required for the analysis of a vibration energy generator. The mathematical models depict the behaviour of a vibration energy generator in a controllable environment. The models are representative of two separate systems, the generator system and the excitation system. The models of the generator system are grouped according to an electrical and mechanical perspective of analysis. This leads to two sub-systems in the generator system - a mechanical system in a generator and an electrical system in a generator. Both the mechanical system and the electrical system are modelled to reveal analytical properties and the relevant power values, including usable power. The excitation system is modelled to address the controllable environment and the predictability thereof for a safe experimental setup. Furthermore, characterization procedures are modelled to determine specific parameters used in the mathematical models describing the systems.

2.2 Mechanical system in the generator

2.2.1 Mechanical model

Following the analytical examples found in literature, the mechanical system is modelled as a single degree of freedom, base excited model as depicted in Figure 2-1. The rigid body with mass m_{ge} in Figure 2-1 is representative of the equivalent mass that is oscillating in the generator system that can store kinetic energy. The cumulative mass of the moving coil and a fraction of the support structures, such as the spider and surround, equate to the equivalent mass that is moving (Rao, 2011). The rigid body in Figure 2-1 is supported by a spring element and a viscous damper element. The spring element is representative of the supporting structures that contribute to the equivalent stiffness coefficient k_{ge} in the generator system that can store potential energy. The structures that contribute to the equivalent stiffness coefficient include the spider, the surround and the magnetic field. The viscous damper element is representative of the supporting structures and effects that contribute to the equivalent viscous damping coefficient c_{ge} in the generator system that dissipates energy. The structures that contribute to the viscous damping coefficient include the surround, the spider and circuitry through forms such as heat, sound and friction. The spring element and viscous damper element are connected to an oscillating base (Kelly, 2012)

The vertical displacement from a static equilibrium point at time t of the rigid body with mass m_{ge} and the oscillating base are depicted by $x_g$and x_b respectively. The velocity and acceleration of the rigid body and oscillating base are $\dot{x}_g$, $\ddot{x}_g$ and $\dot{x}_b$, $\ddot{x}_b$, respectively. It follows that the relative displacement and relative velocity are x_r and $\dot{x}_r$ with amplitude X_r and $\dot{X}_r$.

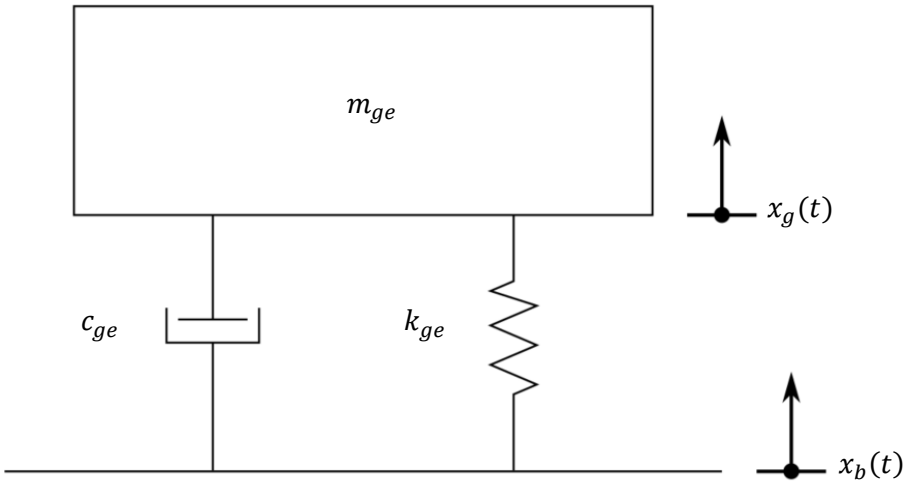

Figure 2-1 Mechanical model

With reference to Figure 2-1 and according to Newton's second law for equilibrium of dynamic forces, the equation of motion for the generator system is

$$m_{ge}\ddot{x}_g + c_{ge}(\dot{x}_g - \dot{x}_b) + k_{ge}(x_g - x_b) = 0 \tag{2.1}$$

with X_b as the steady state displacement amplitude of the base and ω_o the forced frequency. The response of the base is written as

$$x_b(t) = X_b \sin(\omega_o t) \tag{2.2}$$

The equation of motion for the generator system can be written such that

$$m_{ge}\ddot{x}_g + c_{ge}\dot{x}_g + k_{ge}x_g = k_{ge}X_b \sin(\omega_o t) + c_{ge}\omega_o X_b \cos(\omega_o t) \tag{2.3}$$

Each grouped term represents the dynamic force, F_m, F_c, F_k and F_{in} respectively. It can be shown that

$$x_g(t) = X_g \sin(\omega t - \phi) \tag{2.4}$$

where the steady state amplitude of the generator X_g is given by

$$\frac{X_g}{X_b} = \left[\frac{k_{ge}^2 + (c_{ge}\omega_o)^2}{(k_{ge} - m_{ge}\omega_o^2)^2 + (c_{ge}\omega_o)^2}\right]^{\frac{1}{2}} \tag{2.5}$$

and the phase angle ϕ between displacement vectors X_g and X_b is

$$\phi = \tan^{-1}\left[\frac{m_{ge}c_{ge}\omega_o^3}{k_{ge}\left(k_{ge} - m_{ge}\omega_o^2\right)^2 + (c_{ge}\omega_o)^2}\right] \tag{2.6}$$

The displacement amplitudes X_g and X_b can be written

$$X_g = \frac{\ddot{X}_g}{\omega_o^2} \tag{2.7}$$

and

$$X_b = \frac{\ddot{X}_b}{\omega_o^2} \tag{2.8}$$

where $\ddot{X}_g$ and $\ddot{X}_b$ are the corresponding acceleration amplitudes. The critical damping coefficient is

$$c_{cg} = 2\sqrt{k_{ge} m_{ge}} \tag{2.9}$$

The damping ratio ζ_g is the ratio between the equivalent damping coefficient c_{ge} and the critical damping coefficient c_{cg} of the generator system:

$$\zeta_g = \frac{c_{ge}}{c_{cg}} \tag{2.10}$$

The natural frequency of the system can be defined as

$$\omega_n = \sqrt{\frac{k_{ge}}{m_{ge}}} \tag{2.11}$$

and

$$f_n = \frac{\omega_n}{2\pi} \tag{2.12}$$

2.2.2 Usable power

Power can be defined as the change in work done dW over change in time dt, such that the mechanical power P (Walker *et al.*, 2014) is expressed as

$$P = \frac{dW}{dt} \tag{2.13}$$

leading to an expression of force F and velocity $\dot{x}$

$$P = F\dot{x} \tag{2.14}$$

The equation of motion in Equation 2-1 is representative of force in each component as described in paragraph 2.2.1 (Kelly, 2012). Multiplying each term by the velocity of the rigid body $\dot{x}_g$ gives the expression of instantaneous power at time $p(t)$ for each component:

$$m_{ge}\ddot{x}_g\dot{x}_g + c_{ge}(\dot{x}_g - \dot{x}_b)\dot{x}_g + k_{ge}(x_g - x_b)\dot{x}_g = 0 \tag{2.15}$$

with

$$\dot{x}_g = (\dot{x}_g - \dot{x}_b) + \dot{x}_b \tag{2.16}$$

Rearranging leads to an expression that is representative of the instantaneous power in each component (Stephen, 2006).

$$\begin{aligned} m_{ge}\ddot{x}_g\dot{x}_g + c_{ge}(\dot{x}_g - \dot{x}_b)^2 + k_{ge}(x_g - x_b)(\dot{x}_g - \dot{x}_b) \\ = k_{ge}(x_b - x_g)\dot{x}_b + c_{ge}(\dot{x}_b - \dot{x}_g)\dot{x}_b \end{aligned} \tag{2.17}$$

such that the instantaneous power at the rigid body mass p_m, the power at the spring element p_k, the power at the damping element p_c and the power supplied p_{in} can be written as

$$p_m(t) + p_c(t) + p_k(t) = p_{in}(t) \tag{2.18}$$

The total power dissipated by an oscillating body is equivalent to the power dissipated in the damping element (French, 1971). Thus

$$p_m = m_{ge}\ddot{x}_g\dot{x}_g \tag{2.19}$$

$$p_c = c_{ge}(\dot{x}_g - \dot{x}_b)^2 \tag{2.20}$$

$$p_k = k_{ge}(x_g - x_b)(\dot{x}_g - \dot{x}_b) \tag{2.21}$$

$$p_{in} = k_{ge}(x_b - x_g)\dot{x}_b + c_{ge}(\dot{x}_b - \dot{x}_g)\dot{x}_b \tag{2.22}$$

The amplitude values of the power values are P_m, P_k, P_c and P_{in}. The damping ratio ζ_g in Equation 2-10 can be separated into mechanical and electrical contribution. The mechanical damping ratio ζ_{mec} incorporates mechanical components and the electrical damping ratio ζ_{ele} incorporates electrical components and is written

$$\zeta_g = \zeta_{mec} + \zeta_{ele} \tag{2.23}$$

leading to an expression for the average consumed power p_{con} through substitution (Stephen, 2006).

$$P_{con} = \frac{1}{2} \times \left[P_c \times \left(\frac{\zeta_{ele}}{\zeta_g} \right) + P_c \times \left(\frac{\zeta_{mec}}{\zeta_g} \right) \right] \tag{2.24}$$

The first term in Equation 2-24 is representative of the electrical power in the circuit. Given the nature of the electrical circuit as described in paragraph 2.3.1 and the use of Kirchhoff's laws, the average

usable power that is dissipated over a load resistor is equivalent to usable power P_{um} (Stephen, 2006). The variable r is the ratio of the load resistor to the total resistance in the circuit, as discussed in paragraph 2.3.2:

$$P_{um} = \frac{1}{2} \times \left[P_c \times \left(\frac{\zeta_{ele}}{\zeta_g} \right) \times (r) \right] \tag{2.25}$$

2.3 Electrical system in a generator

2.3.1 Electrical model

With aid of literature and acceptable assumptions as discussed in the demarcation section, the simple electrical system is modelled to reveal electrical properties. The electrical system is the circuitry that is in motion within the magnetic field. The circuitry consists of the moving coil with electrical impedance Z_c, and the load resistor with electrical resistance R_l coupled in series. Electrical switches are incorporated to change between the different load configurations with varying electrical resistance R_l. The schematics of the electrical circuity is included in Chapter 4. Figure 2-2 illustrates a single configuration for the electrical model.

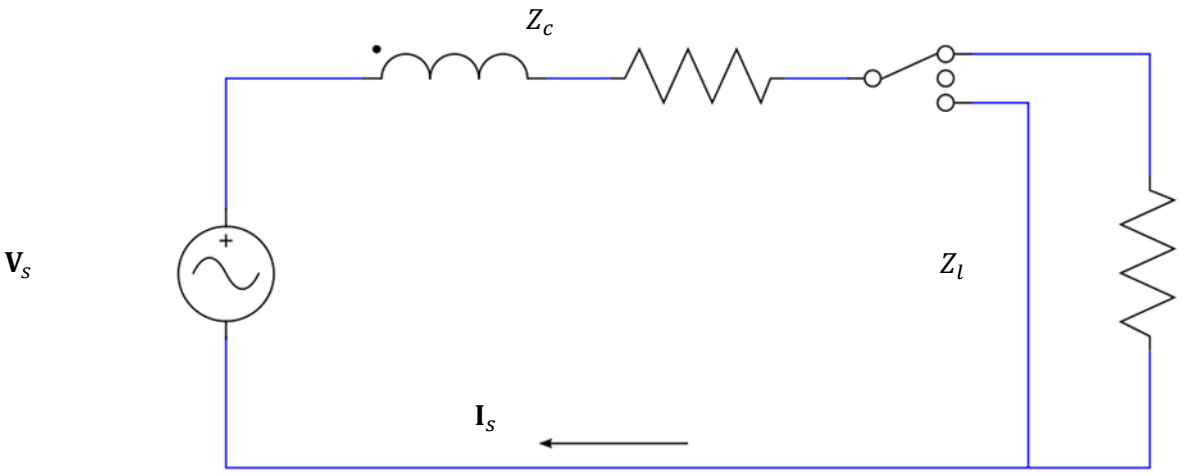

Figure 2-2 Electrical model

The relative velocity between the moving coil and the magnetic field, $\dot{x}_r$ is the same relative velocity $\dot{x}_r$ between the rigid body mass of the generator and the oscillating excitation system. The relative velocity $\dot{x}_r$ induces a voltage represented in Figure 2.2 as a voltage source $\mathbf{V_s}$ according to Faraday's law as discussed in paragraph 1.2.4.3. The moving coil interacts with the magnetic field such that a coupling factor BL is apparent. The coupling factor BL is a grouped parameter of the magnetic field strength B in unit Tesla and L the length of wire in unit meter that is in the magnetic field B. The induced voltage $\mathbf{V}_s$ is determined by

$$\mathbf{V}_s = BL\dot{x}_d \tag{2.26}$$

The closed condition with any of the variable load resistors R_l allows current $\mathbf{I}_s$ to flow when the circuitry is excited by a voltage source $\mathbf{V}_s$. The application of Kirchhoff's voltage law gives the following equation describing the current that flows in the circuitry as

$$\mathbf{V}_s = \mathbf{I}_s Z_t \tag{2.27}$$

and the potential difference across the load resistor as

$$\mathbf{V_l} = \mathbf{I}_s R_l \tag{2.28}$$

The total impedance of the circuit

$$Z_t = Z_c + R_l \tag{2.29}$$

is given by the sum of the coil impedance Z_c and load resistance R_l, respectively. The coil impedance is given by the expression

$$Z_c = \sqrt{R_c^2 + (\omega_o L_c)^2} \angle \arctan\left(\frac{R_c}{\omega_o L_c}\right) \tag{2.30}$$

where ω_o is the operating frequency and L_c is the inductance of the coil.

2.3.2 Usable power

The average electrical power in the electrical circuit is given by the use of the root mean square (RMS) amplitude values of the induced current I_s and induced voltage V_s

$$P_e = V_s I_s \cos(\theta_v - \theta_i) \tag{2.31}$$

where $\theta_v - \theta_i$ is the power factor angle, which is the phase angle between the induced current $\mathbf{I}_s$ and induced voltage $\mathbf{V}_s$, and the power factor pf is

$$pf = \cos(\theta_v - \theta_i) \tag{2.32}$$

The average usable electrical power is given by

$$P_{ue} = |\mathbf{I}_s|^2 (R_l) \tag{2.33}$$

2.4 Excitation system and model

To effectively introduce base excitation for the generator system, a mechanical structure is conceived by aid of Figure 2-3. Similar to a shaker apparatus the excitation system model is a single degree of freedom structure mounted upon a fixed base. The excitation system response $x_b(t)$ defined in Chapter 2.1 is the steady state response of a rigid body mass m_{be} in Figure 2-3. The base consists of a steel structure with excitation motors firmly attached. The structure is considered to be very stiff in order to assume a rigid body. The rigid body (including the excitation motors), part of the loudspeaker that is not considered to be part of the generator system, and contributing mass of the coils springs have the equivalent mass m_{be}. The excitation system is supported by numerous coil springs. The coil springs establish the support of the excitation system and is represented in Figure 2-3 as the spring element with equivalent stiffness coefficient k_{be}. The viscous damper element represents the damping characteristics in the excitation system with equivalent damping coefficient c_{be}. The dynamic elements are attached to a fixed base as shown in Figure 2-3.

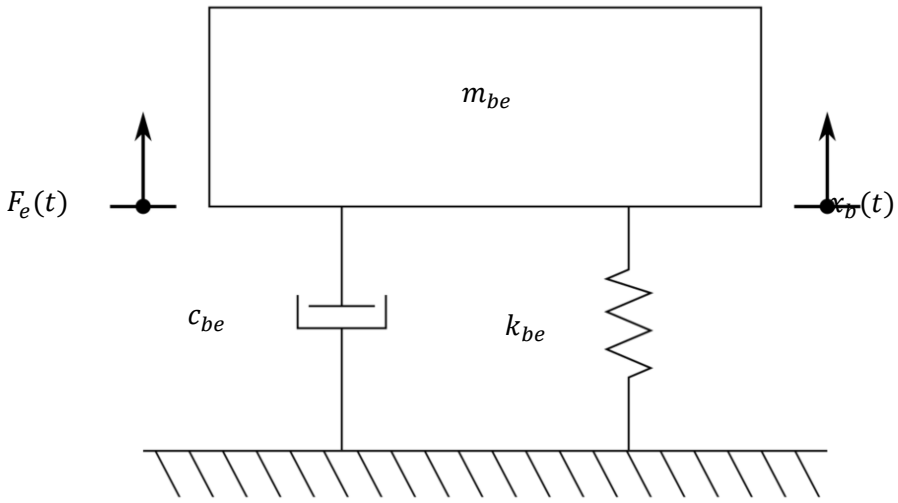

Figure 2-3 Excitation model

Two excitation motors that are mounted symmetrically on the excitation system produce a resultant force $F_e(t)$. With Newton's second law and the conservation of equilibrium of the dynamic forces, the equation of motion for the excitation system is

$$m_{be}\ddot{x}_b + c_{be}\dot{x}_b + k_{be}x_b = F_e\, sin(t) \tag{2.34}$$

The steady state response amplitude X_b of the excitation system is given by

$$X_b = \frac{F_e}{\sqrt{(k_{be} - m_{be}{\omega_o}^2)^2 + c_{be}^2{\omega_o}^2}} \tag{2.35}$$

The magnitude of the resultant excitation force F_e with a rotational speed of the motors defined as ω_o and the unbalanced mass m_u at the radial position r_u is

$$F_e = m_u r_u {\omega_o}^2 \sin(\omega_o t) \tag{2.36}$$

2.5 Characterization models

2.5.1 Free response decay analysis

The mathematical model described below is used to determine the dynamic properties of the generator system with no electrical load attached. The generator system mounted to a fixed base is observed schematically in Figure 2-4. The figure is representative of the loudspeaker being mounted to the floor. Inducing a free vibration response of the vertical mode allows characterization of the dynamic properties of the generator system. The periodic time of the damped free vibration is described with the variable τ_d. The damped frequency ω_d is calculated as follows:

$$\omega_d = \frac{2\pi}{\tau_d} \tag{2.37}$$

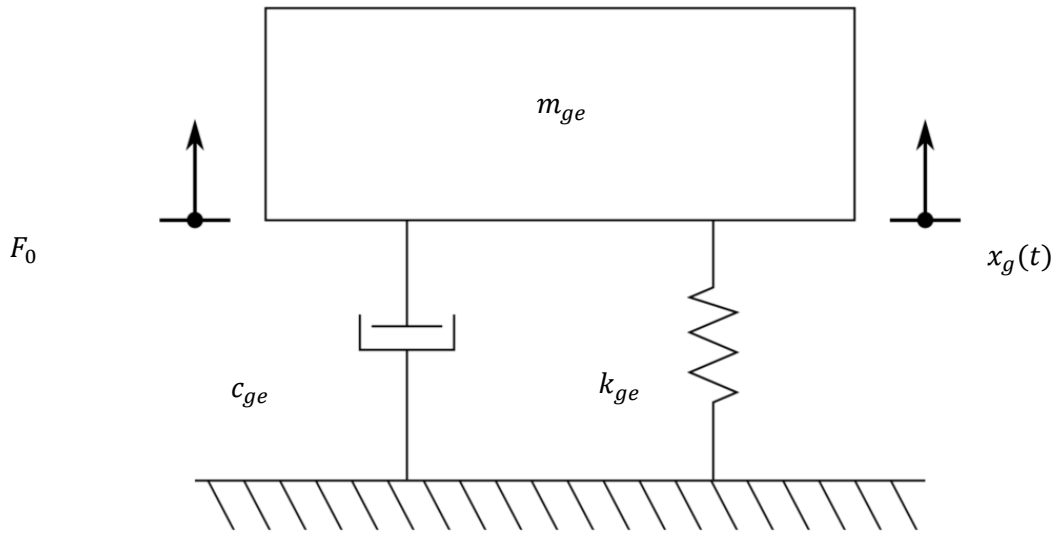

Figure 2-4 Fixed base generator

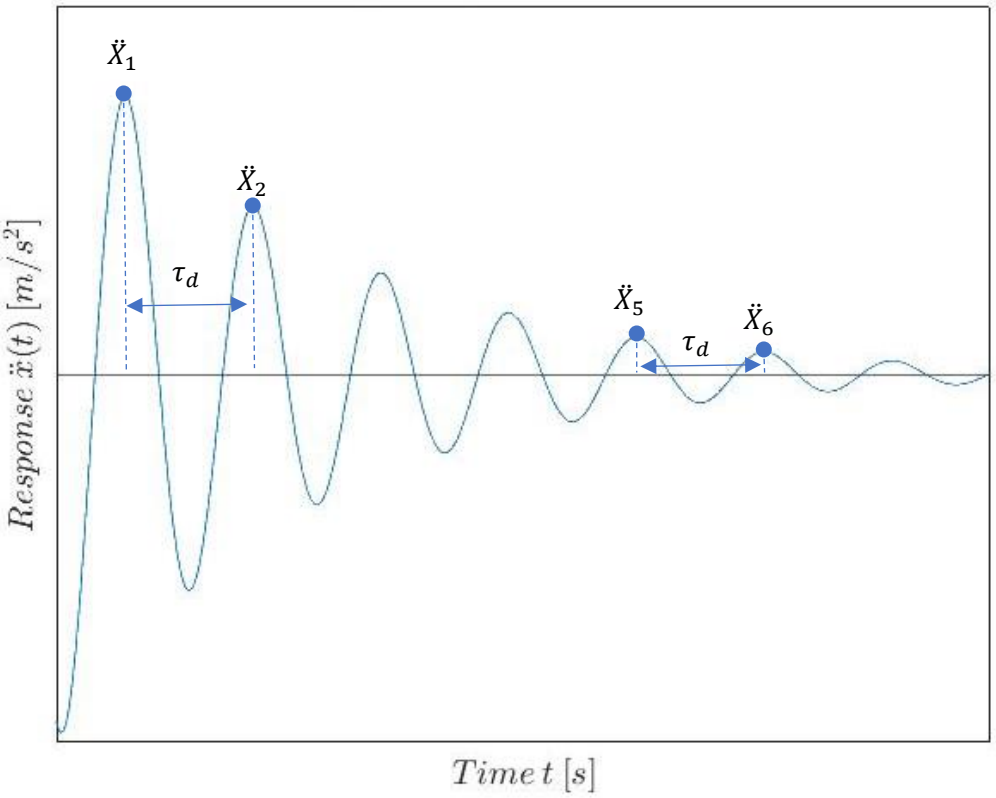

Figure 2-5 Free decay response

Two acceleration amplitudes $\ddot{X}_{g1}$ and $\ddot{X}_{gn+1}$ corresponding to time t_1 and t_{n+1} is noted in the time domain of the measured signal. The variable n is an integer for the complete cycles between the respective acceleration amplitudes. The acceleration ratio is expressed in terms of the periodic time τ_d , damping ratio ζ_{mec}, number of cycles n and the natural frequency ω_n:

$$\frac{\ddot{X}_{g1}}{\ddot{X}_{gn+1}} = e^{n\zeta_{mec}\omega_n\tau_d} \tag{2.38}$$

The natural or resonant frequency ω_n is

$$\omega_n = \frac{\omega_d}{\sqrt{1-\zeta_{mec}^2}} \tag{2.39}$$

Solving Equations 2-38 and 2-39 simultaneously gives the natural frequency ω_n, the equivalent stiffness coefficient k_{ge}, equivalent damping coefficient c_{ge} and the damping ratio ζ_{mec}.

$$k_{ge} = m_{ge}\omega_n^2 \tag{2.40}$$

Critical damping coefficient c_{cg} is expressed with the equivalent moving mass of the generator m_{ge} and the equivalent stiffness k_{ge} in Equation 2-41. The equivalent damping coefficient is then described by the damping ratio ζ_{mec} in Equation 2-42.

$$c_{cg} = 2\sqrt{m_{ge}k_{ge}} \tag{2.41}$$

$$c_{ge} = \zeta_{mec}c_{cg} \tag{2.42}$$

The average response between the peaks is

$$X_{avg} = \frac{(\ddot{X}_{g1} + \ddot{X}_{gn+1})}{2\omega_0^2} \tag{2.43}$$

2.5.2 *In situ* analysis

Figure 2-1 in paragraph 2.2.1 is representative of the generator system, which is used to characterise the dynamic properties of the generator *in situ* as installed on the excitation system. The acceleration response amplitude of the generator system $\ddot{X}_g$, excitation system $\ddot{X}_b$, and the phase angle ϕ are used to solve Equations 2-5 and 2-6 simultaneously. This determines the dynamic properties of the generator k_{ge}, c_{ge} and the natural frequency f_n.

2.5.3 Frequency Sweep

Utilizing Equation 2-40 and associated Figure 2-4 to obtain the equivalent stiffness coefficient k_{ge} entails a frequency sweep of the system. Through incrementally changing the frequency, maximum response and frequency is obtained, the natural frequency f_n is then determined. Equation 2-40 can be solved using the equivalent mass m_{ge} to determine the equivalent stiffness coefficient k_{ge}.

2.5.4 Electrical damping

The generator system moved to a fixed base setup and a disassociated force $F_0(\mathrm{t})$ acting on the rigid body similar to that of the free decay response model in Figure 2-5. However, the force is continuously acting and creates a steady state response in the generator. With Newton's second law and the conservation of equilibrium of the dynamic forces, the equation of motion for the generator system becomes

$$m_{ge}\ddot{x}_g + c_{ge}\dot{x}_g + k_{ge}x_g = F_0\, sin(t) \tag{2.44}$$

The response with no electrical load connected is given by

$$X_{g_{before}} = \frac{F_0}{\sqrt{\left(k_{ge} - m_{ge}{\omega_o}^2\right)^2 + c_{ge}^2{\omega_o}^2}} \tag{2.45}$$

After a switch is flipped the response of the generator is given by

$$X_{g_{after}} = \frac{F_0}{\sqrt{\left(k_{ge} - m_{ge}{\omega_o}^2\right)^2 + c_{ge}^2{\omega_o}^2}} \tag{2.46}$$

The damping in the generator system is given by

$$\zeta_g = \frac{c_{ge}}{c_{cg}} \tag{2.47}$$

With electrical load and response $X_{g_{before}}$ the damping is given by

$$\zeta_g = \zeta_{ele} + \zeta_{mec} \tag{2.48}$$

With no electrical load and response $X_{g_{after}}$ the damping is

$$\zeta_g = \zeta_{mec} \tag{2.49}$$

The response before $X_{g_{before}}$ and after $X_{g_{after}}$ the addition of a variable load resistor is used to solve Equation 2-45 and 2-46 sequentially for associated damping values ζ_g, assuming stiffness and mechanical damping ζ_{mec}remain constant. The difference in the damping values give the approximate value of electrical damping ζ_{ele}.

2.5.5 Coupling factor parameter

A potential difference $\mathbf{V}_s$ is generated across the generator coil when it is in motion $\dot{x}_r$ within a magnetic field BL. The Equation 2-26 is utilised in characterization of the coupling factor BL , by disregarding the load resistor such that the representing Figure 2-2, is an open circuit.

2.6 Conclusion

Mathematical models have successfully been developed with aid of basic literature principles to predict mechanical and electrical cyclic properties and usable power. Other models were developed to characterise dynamic properties and the coupling factor for the respective mechanical and electrical systems. These models will be incorporated into computer programs for simulation purposes within the MATLAB environment. The mathematical models are then addressed in computer implementation described in Chapter 3.

Chapter 3 Computer implementation

3.1 Introduction

The mathematical models described in Chapter 2 were successively implemented into computer programs within the MATLAB software environment. This implementation is elaborated on in Chapter 3. Each model is addressed in the same manner by stipulating the relevant Input and Output parameters with the required intermediate steps such as logical computations and numerical iterations. The implementation of Finite Element Analysis within the FEMM4.2 software environment for the simulation of the coupling factor was done similarly.

3.2 Mechanical system

3.2.1 Mechanical response and usable power

The flow chart in Figure 3-1 describes the computer program *Pred_mec.m* which was used to predict the response (acceleration, velocity and displacement) of the mechanical system and the usable power. The program is included in Annexure A. The second order differential Equation 2-1 was converted to two first-order differential equations. These equations were then implemented in the MATLAB environment and solved by numerical integration with the built-in MATLAB algorithm namely *ode.23m*. The input data and associated variables are listed below, connected to the output data and variables through a list of equation used as a transitional step.

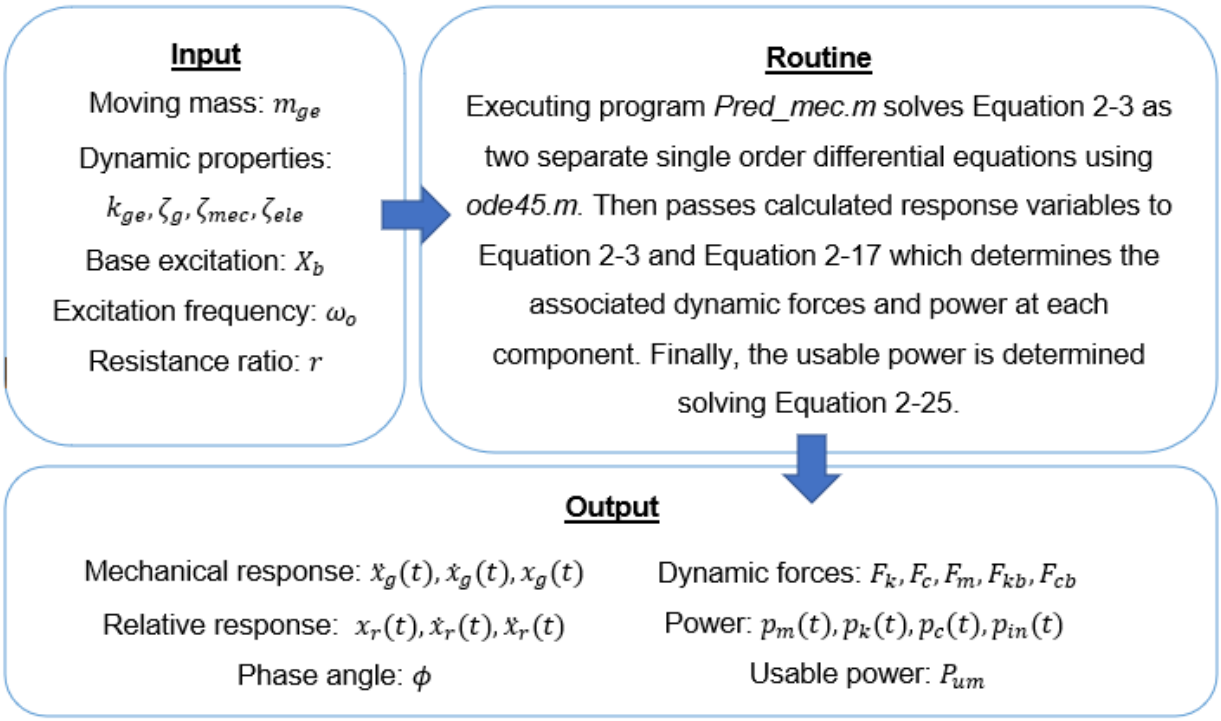

Figure 3-1 Pred_mec.m flowchart - Mechanical system

3.3 Electrical system

3.3.1 Electrical response and usable power

The flow chart in Figure 3-2 describes the computer program *Pred_elec.m* which was used to predict the response (voltage and current) of the electrical system and the usable power. The model was implemented into the MATLAB environment for consecutive execution of Equation 2-26 to Equation 2-33. The three shapes below contain the input variables and the output variables separated by the routine that the program follows in Figure 3-2.

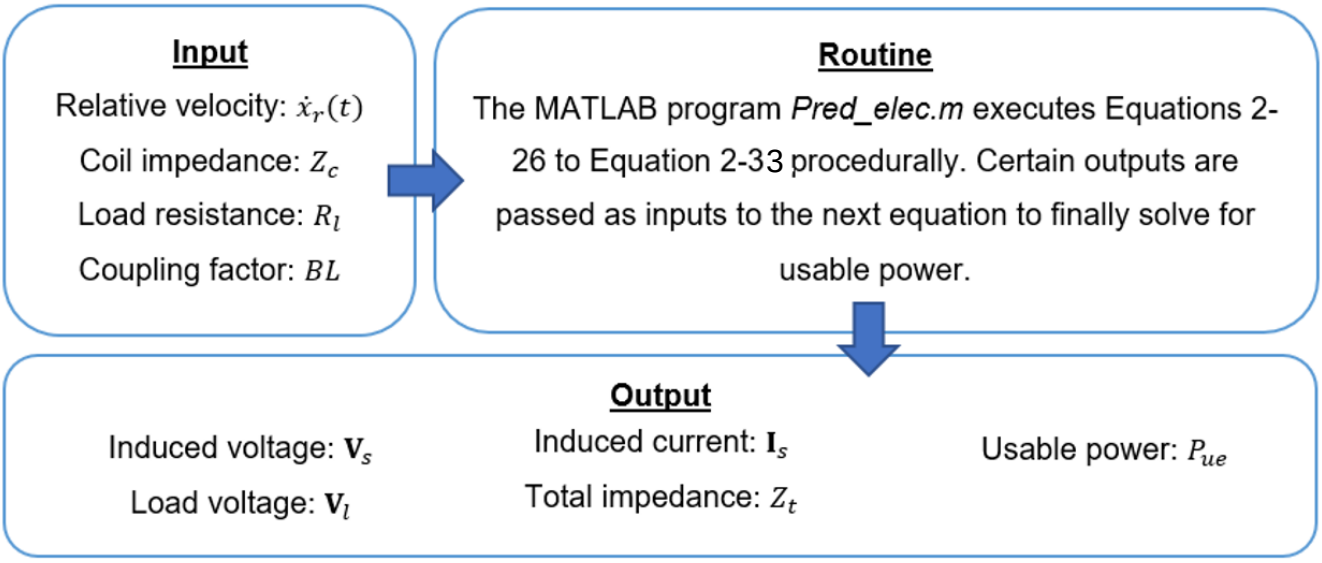

Figure 3-2 Pred_elec.m flowchart - Electrical System

3.4 Excitation system

3.4.1 Excitation response

The flow chart in Figure 3-3 describes the computer program, *step_base.m*, which was used to approximate the response (acceleration, velocity and displacement) of the excitation system. The second order differential Equation 2-34 is converted to two first-order differential equations. These equations were then implemented in the MATLAB environment and solved by numerical integration with the built-in algorithm namely *ode.45m*. Within the three rectangles are the details of input variables, routine and output variables.

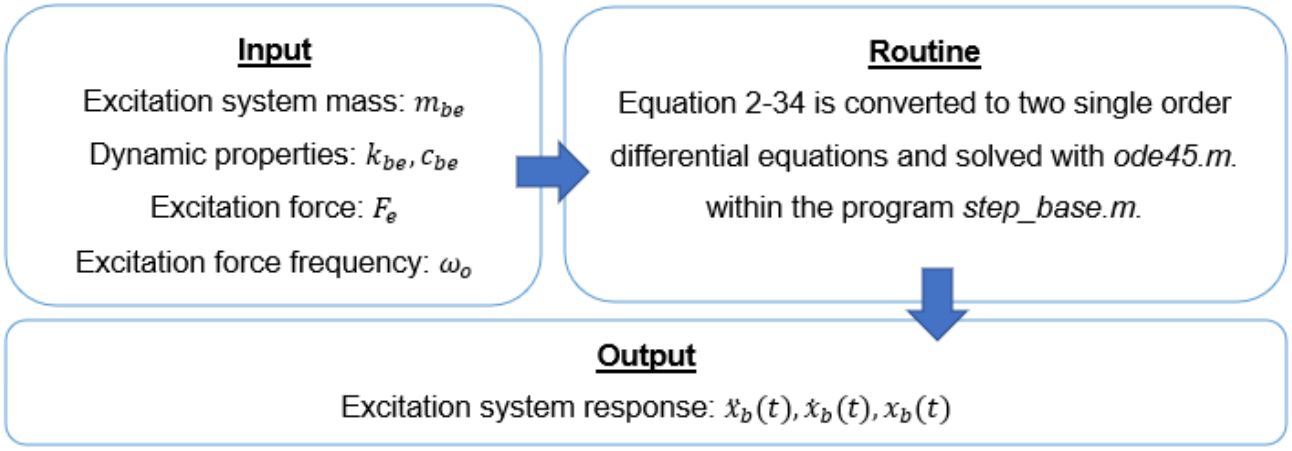

Figure 3-3 step_base.m flowchart - Excitation System

3.5 Characterization

3.5.1 Plane wave tube sweep

The stiffness coefficient k_{ge} is approximated through characterization utilising Equation 2-40. The equation is implemented into the MATLAB program *step_1.m* to successively calculate values and create graphed data. The equation within the MATLAB environment is not depicted within a flow chart due to its simplicity.

3.5.2 Plane wave tube with variable load

The damping ζ_{ele} associated with the variable load configurations are approximated through the model and procedure described in paragraph 2.5.4. The model is iterated to obtain the approximate damping values ζ_{ele} for each associated electrical load. The model is implemented into *step_2.m* MATLAB program for fast iterations. Furthermore, the program is illustrated in a flow chart in Figure 3-4.

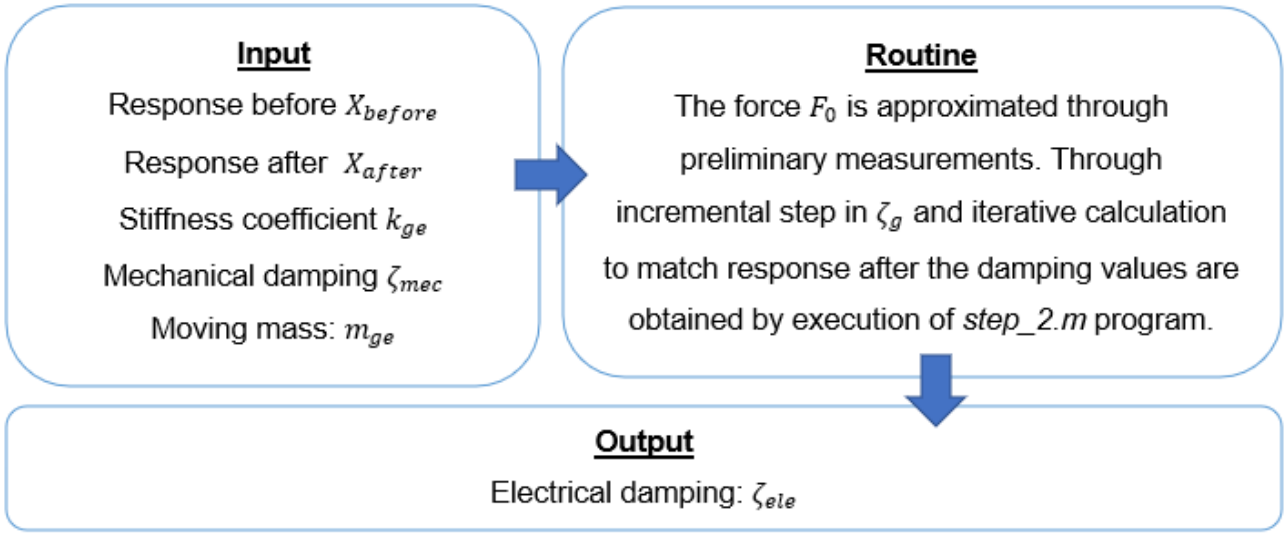

Figure 3-4 step_2.m flowchart

3.5.3 Free response decay analysis

The mathematical model described in paragraph 2.5.1 was implemented in a MATLAB environment to compute the equivalent stiffness and damping coefficients of the generator system. The mathematical logic is depicted within the flow chart in Figure 3-5, where the Equations 2-38 and 2-39 are solved simultaneously. The input data used is two consecutive acceleration amplitudes, periodic time, mass and number of cycles between these amplitudes.

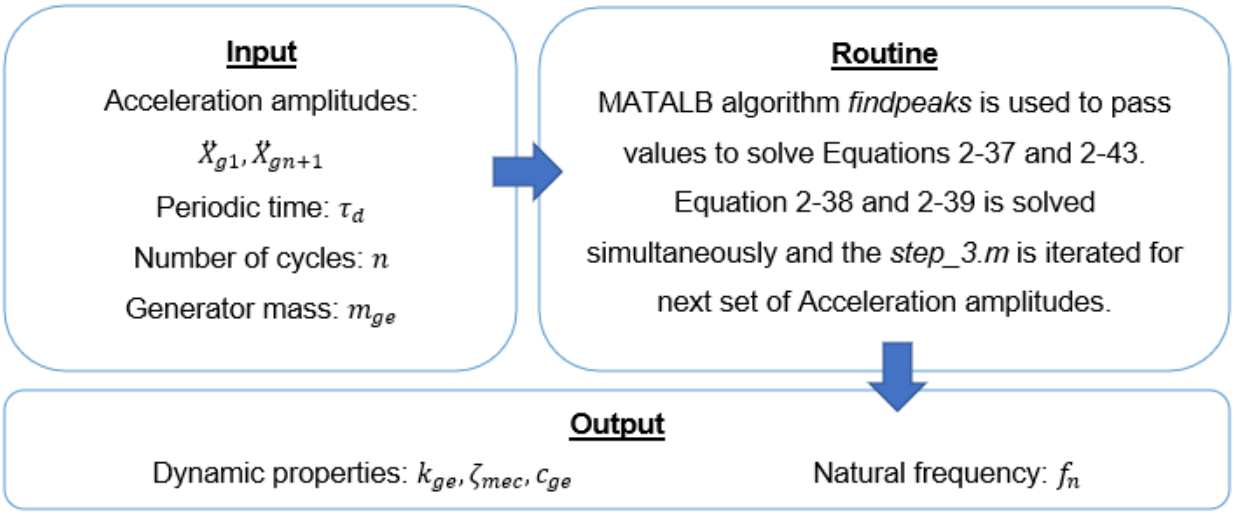

Figure 3-5 step_3.m flowchart

3.5.4 *In situ* characterization

The flow chart for the *in situ* characterization model to predict the dynamic properties of the generator system is depicted in Figure 3-6. The mathematical model described in paragraph 2.5.2 is converted to MATLAB code *step_5.m* to be executable on demand. The Equations 2-5 and 2-6 are solved simultaneously, for which the input data used is the generator system and excitation system acceleration response amplitudes, that are associated with the phase angle and excitation frequency.

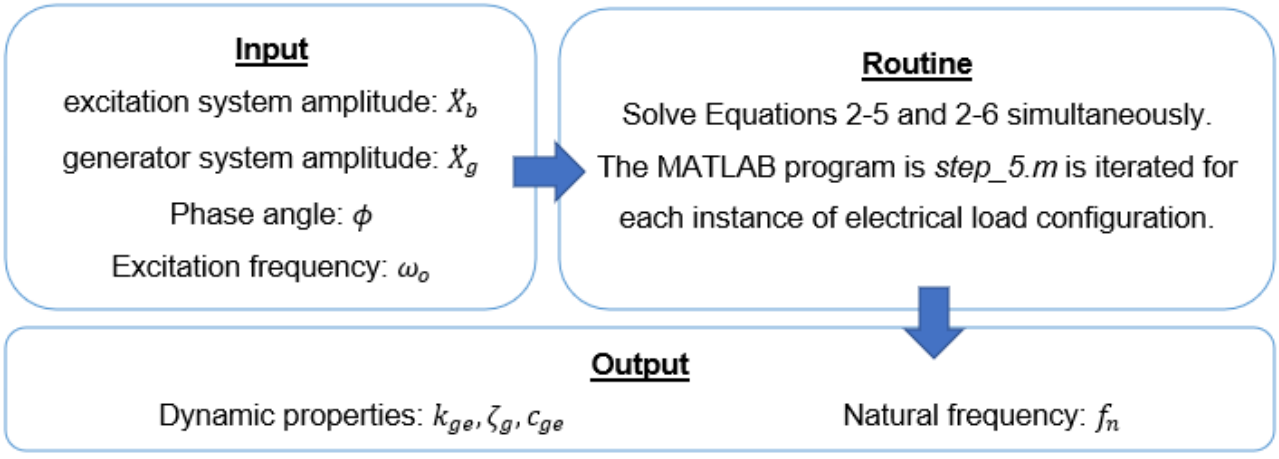

Figure 3-6 step_5.m flowchart

3.5.5 Coupling factor characterization

The Equation 2-26 as stipulated in paragraph 2.5.5 was implemented within a MATLAB environment. The input data used is the response of the generator system and the induced voltage. The program allows for quick successive calculation for different instances. The MATLAB program *step_BL.m* is not described a in flow chart due to its simplicity.

3.5.6 Finite element analysis

The computer implementation to determine the coupling factor using Finite Element Analysis (FEA) is achieved through the use of FEMM4.2, a free software package. The methodology of implementation is illustrated in the flow diagram in Figure 3-7. The input data used are the dimensions, properties of the magnetic circuit, the material properties and properties of the coil such as dimensions, material and number of turns in the coil.

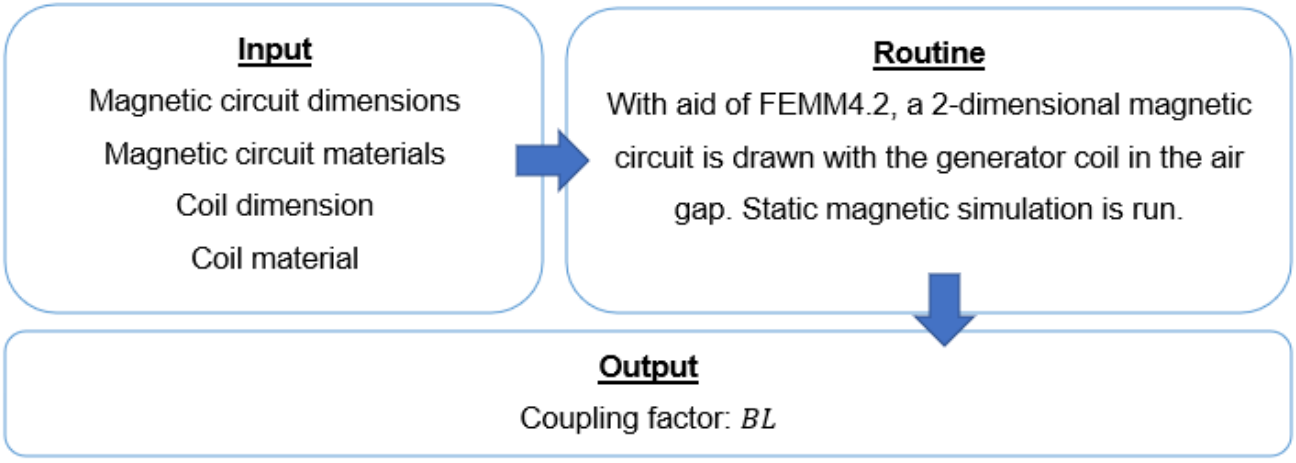

Figure 3-7 Finite element analysis

3.6 Conclusion

All mathematical models developed in Chapter 1 could be successfully implemented into MATLAB. The input and output parameters of each model are clearly illustrated in each flow chart. Furthermore, the use of specific parameters for FEA analysis is illustrated in a flow diagram to determine the coupling factor. The code pertaining to the model input and output parameters is attached in Appendix A. These codes are used in Chapter 4 and 5 for experimental characterization and experimental evaluation, respectively.

Chapter 4 Experimental characterization

4.1 Introduction

The properties of the vibration energy generator system at varying load conditions and the properties of the excitation system have to be characterised, since the characterised values are required as input parameters. The input parameters are used to successfully make predictions for usable power and ensure a safe experimental setup. The parameters to be characterised are specific to each model and clearly depicted in Chapter 3.

Firstly, the available instrumentation is presented in this chapter. Then, dynamic properties used in the generator mechanical models are systematically determined through consecutive experiments referred to as steps in MATLAB programs. This is followed by the characterization procedures for parameters used in the generator electrical models. Lastly, the characterised properties of the excitation system are set forth.

4.2 Measuring Instrumentation

4.2.1 Mechanical measurements

The successful measurement of the mechanical response of the excitation and generator system requires transducers, a real time FFT analyser and a data recorder. The two different transducers utilized were the Dytran sensor and PCB sensor. Signals from the transducers were analysed and recorded by the diagnostic instrument 2200 FFT analyser. All three of these instruments with respective connectors are captured in Figure 4-1 and Figure 4-2. The $100\ mV/G$ Dytran sensor was specifically used at the mechanical generator system to reduce the effect on dynamic properties due to the added mass. The sensor is but 2% of the equivalent mass of the generator, weighing only $4\ g$. The response of the excitation system was measured using a $100\ mV/G$ PCB accelerometer sensor. The instrument data sheets are included in the Appendix B.

Figure 4-1 DI 2200 and PCB sensor

Figure 4-2 Dytran sensor

4.2.2 Electrical measurements

The electrical response of the generator system and the relevant electrical properties are measured using either the multimeter illustrated in Figure 4-3 or the DI 2200 instrument with electrical probes. The multimeter displays only rms or peak amplitude values, however, it can also measure current, voltage and resistance.

Figure 4-3 Multimeter

4.2.3 Mass scaling

The instrument used to weigh the components of the dynamic systems was the PRW 30 digital scale. Included in Figure 4-4 is a picture of the mass scale with a moving mass component on the measuring platform. The magnetic components were measured using a simple hand-held scale to reduce the effects of magnetic fields on measured values.

Figure 4-4 PRW 30 digital scale

4.3 Generator mechanical system

4.3.1 Mass properties

Due to the nature of the chosen vibration energy generator, components were carefully removed from the dissected speaker and measured individually. The total mass of each component was extrapolated from the measured value by simply doubling the measured values. The extrapolated data was controlled by comparing the sum of the components to the total mass of a complete loudspeaker. There is only a 3% discrepancy when comparing the extrapolated total to the total of a complete speaker.

Table 4-1 lists the components that contribute to the equivalent mass of the generator. The equivalent mass of the generator m_{ge} is equated to $0.1779\,kg$. It compares well with the manufacturing specification reported in Appendix C. The manufacturing specification of Mms is $0.166\,g$ giving only a 6% difference in characterization of the mass.

Table 4-1 Loudspeaker component mass

Component	Measured mass [g]
Half speaker	2940
Structure	2843.9
Generator	88.3
Diaphragm	58.7
Coil and spider	30.6
Spider	2.8
Coil	27.3
Connection	30.9
Dytran sensor	4

White dotted lines on Figure 4-5 show the approximate separation by part for contribution of mass. Only a $1/3$ of a spring mass contributes to the moving mass in a coil spring (Rao, 2011; Ruby, 2000). This definition is applied to the spider even though it is not a coil spring. The spider can be seen as infinitely numerous coil springs attached all around the voice coil.

Table 4-2 Equivalent moving mass

Component	Equivalent mass m_{ge} [g]
Equivalent generator mass	177.9

Figure 4-5 Dissected loudspeaker

4.3.2 Dynamic properties

4.3.2.1 Plane wave tube sweep

A preliminary experiment to determine the dynamic properties of a loudspeaker was completed. The preliminary experiment is a frequency sweep that utilised the plane wave tube apparatus. The plane wave tube is the experimental apparatus shown in Figure 4-6. With the aid of *step_1.m* MATLAB program the preliminary values for natural frequency f_n of the generator and the stiffness coefficient k_{ge} of the generator system are determined and graphed.

Also depicted in Figure 4-6 is a laptop that produces the sinusoidal signal that is relayed to an amplifier. The amplifier is visible to the far right in Figure 4-6. The amplifier drives a loudspeaker mounted, facing inward to the tube, on the right. The driven loudspeaker excites the designated loudspeaker that is to be characterised. The designated loudspeaker is mounted on the left of the tube. The DI 2200 instrument is visible to the left of the plane wave tube apparatus. The white box below the DI 2200 instrument is the switch box with variable resistors.

Figure 4-6 Plane wave tube apparatus

The volume on the laptop allowed steady increments to gauge the extent of amplitude dependency on the designated speaker. With the volume setting fixed, the frequency sweep was completed over a range that is expected. Through the frequency sweep the maximum amplitude of the response was noted. The maximum response of the generator was recorded at incremental volume settings.

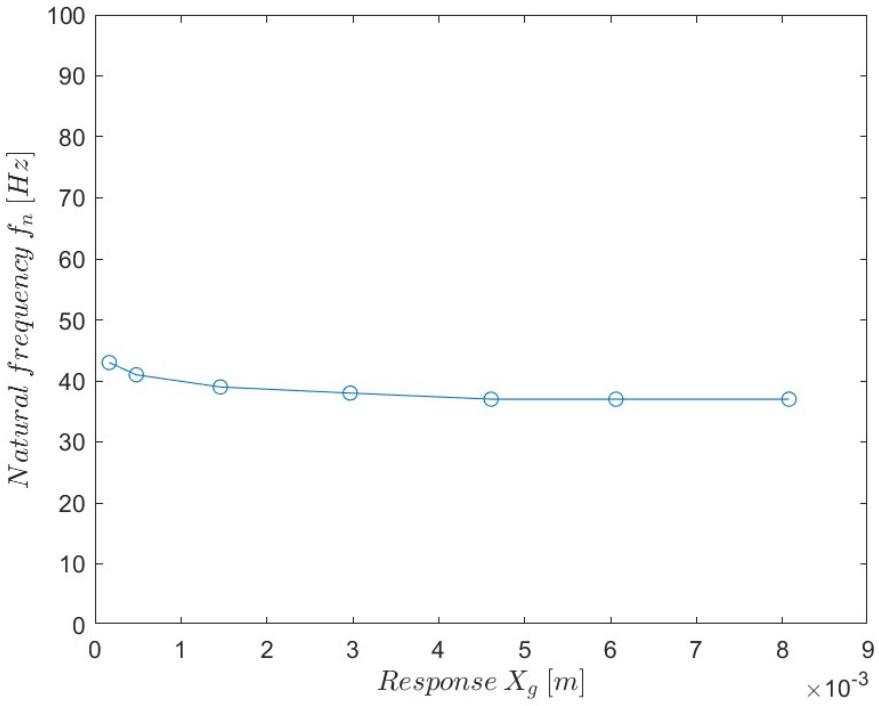

Figure 4-7 Step 1 generator natural frequency

As per example the maximum response $X_{ge} = 2.97\ mm$ was noted at a frequency $f_o = 38\ Hz$ While the moving mass $m_{ge} = 0.1779\ kg$ remained constant at all instances. The natural frequency $f_n = 38\ Hz$ and the equivalent stiffness coefficient $k_{ge} = 10141.5\ N/m$ is determined with Equation 2-40. The MATLAB program *step_1.m* was iteratively executed for all measured instances. The resultant stiffness coefficients and natural frequencies for each instance of a volume setting is graphed against the measured response in Figure 4-7 and Figure 4-8 respectively.

The X and Y-axis are placed in this specific manner in order to have a better view of the extent of the amplitude dependency (Nel & Van Wyngaardt, 2014). This graph orientation is used by Nel et al In the study of amplitude dependency. Depending on the scale of the Y-axis, the severity of amplitude dependency may differ. However, it is clear that some amplitude dependency is present in the generator system for mechanical properties at relatively small displacements as seen in Figure 4-7 and Figure 4-8. The use of these values for prediction is not viable as the air cushion within the plane wave tube is foreseen to have an effect on the accuracy of calculated values. It was could also be the reason for the visible amplitude dependency. Therefore, the free decay response analysis was completed and is reported later on.

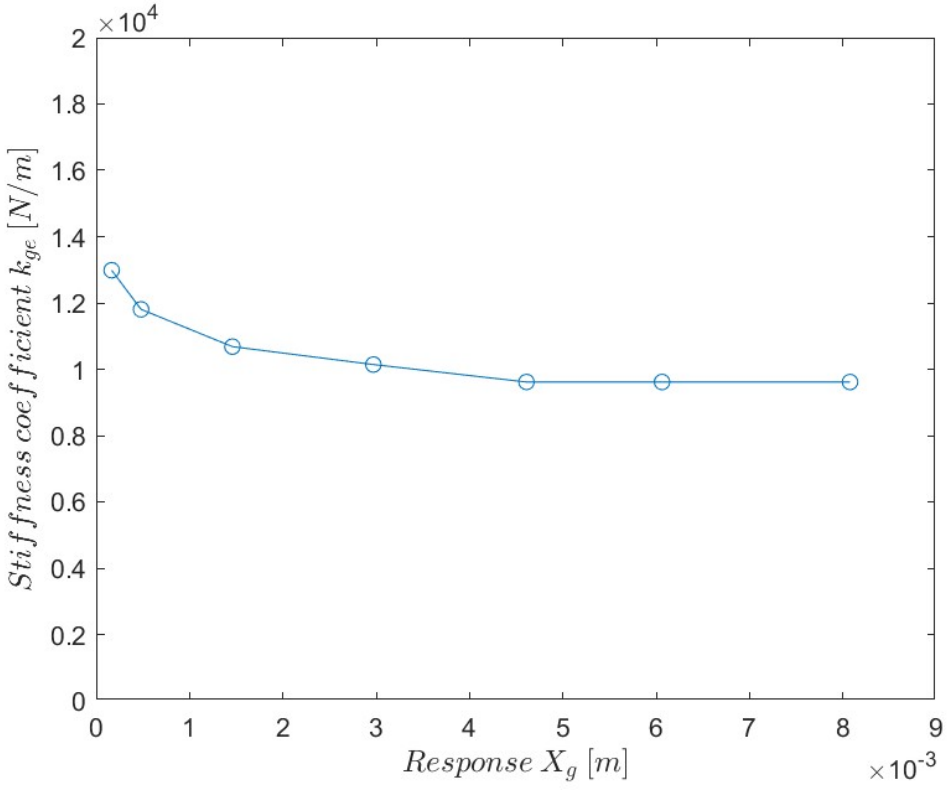

Figure 4-8 Generator stiffness coefficient step_1

4.3.2.2 Plane wave tube with variable load

The plane wave tube experimental apparatus was utilised to determine the effect of an electrical resistor on the mechanical system. Furthermore, it assisted in choosing suitable resistors for the variable load conditions for evaluation purposes.

For the characterization below, purely resistive values varied from $0.5\,\Omega$ to $46\,\Omega$ in this setup. The process of experimentation was started with a specific load resistor connected in series to the vibration generator. The coils were then connected in parallel. An electrical switch was present to toggle between a closed circuit (load condition) and an open circuit (unloaded condition). The frequency and volume setting as excitation for all load conditions was held constant. The response $X_{g\ before}$ of the moving mass in the unloaded condition is recorded with the open circuit. The switch is toggled and the response $X_{g\ after}$ of the moving mass is recorded in the loaded condition.

The dynamic properties of the mechanical system, stiffness coefficient k_{ge} and damping ζ_{mec} is assumed to remain constant. This assumption is contradictory to literature in paragraph 1.2.3. Literature shows that the natural frequency and consequently the stiffness coefficient of the system will change with addition of a resistive load. To determine the extent of error in the application of the assumption would require a frequency sweep for each electrical load resistance. The specific frequency sweep for each load resistor would show the change in natural frequency and stiffness coefficient. This is impractical as the resistors quickly overheat during such an experiment even though $5\,W$ resistors where used. Secondly, there is foreseen inaccuracy of characterised properties due to the air cushion within the plane wave tube apparatus. The experiment is still considered insightful in terms of the behaviour of a vibration energy generator.

As per example the set volume and operating frequency $f_o = 38\,Hz$ is kept constant. The dynamic properties of the mechanical system are assumed to be stiffness coefficient $k_{ge} = 13157.8\,N/m$, damping coefficient $c_{ge} = 3.39\,Ns/m$ and damping $\zeta_{mec} = 3.5\,\%$ according to the Thiele small parameters as presented in Appendix C. The response of the moving mass in unloaded condition is $X_{g\ before} = 4.0\,mm$ and the response of the moving mass in loaded condition is $X_{g\ after} = 3.1\,mm$. Running the MATLAB program *step_2.m* gives the perceived added damping of the electrical system as $\zeta_{ele} = 9.6\,\%$. The experiment was completed for all available load resistors and the perceived electrical damping ζ_{ele} is graphed in Figure4-9.

Figure 4-9 gives an indication of the effect of a resistor on the generator under steady state excitation. This load condition with maximum perceived damping is used at the evaluation experiment to ensure a safe commissioning of the generator and excitation system.

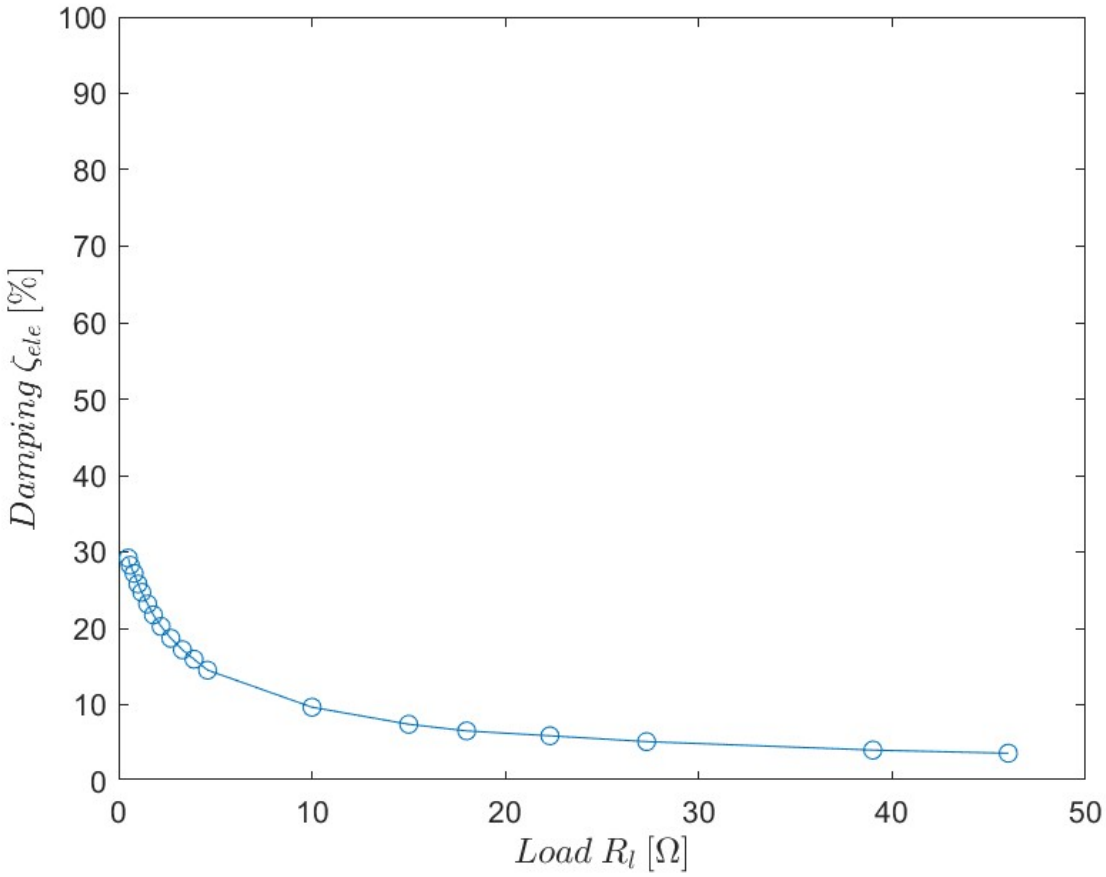

Figure 4-9 Variable electrical damping

4.3.2.3 Free response decay analysis

The loudspeaker was attached securely to a structure that is rigid in the experiment. The experimental setup is shown in Figure 4-10. The figure illustrates the sensor placement and instruments that were used. A frequency signal was generated on the laptop using Sinegen as a software tool. The signal was amplified by the amplifier, pictured in the middle of Figure 4-10. The amplified signal is then used to drive the loudspeaker that is to be characterised. The excitation was increased to ensure maximum displacement amplitude before allowing free decay response. By interrupting the circuit with a switch, the speaker was allowed to follow the typical exponential decay seen in Figure 4-11 without excitation from the amplifier. The response was recorded using the diagnostics instrument 2200 FFT Analyser. Several free response tests were conducted to ensure repeatability. An example of the measured vibration time domain signals is graphed in Figure 4-11.

Figure 4-10 Free decay response setup

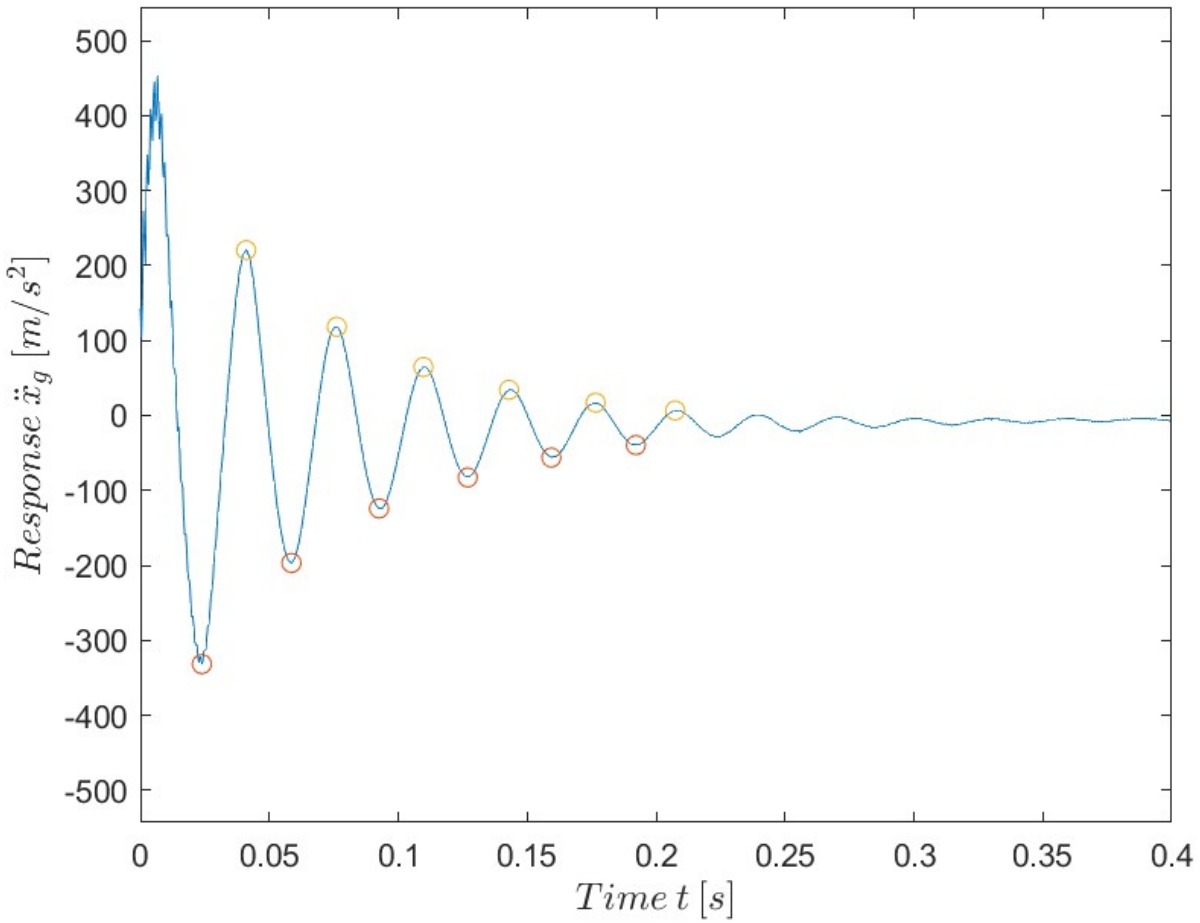

Figure 4-11 Typical free decay time response at step 3

Two consecutive peak values, $X_{g1} = -196.74\ m/s^2$ and $X_{g2} = -124.03\ m/s^2$ with corresponding time $t_1 = 58.59 \times 10^{-3}\ s$ and $t_2 = 92.57 \times 10^{-3}\ s$ substituted into the computer program, *step_3.m* characterises the values of the dynamic stiffness $k_{ge} = 6113.8\ N/m$, damping $\zeta_{ge} = 7.3\ \%$ and a natural frequency $f_n = 29.5\ Hz$. These values were obtained at an $X_{avg} = 4.7\ mm$. Repeating the above procedure for several data points and experiments, a compilation of data is created for different amplitudes correlating to X_{avg}.

Figure 4-12 shows the amplitude dependency in natural frequency graphically and is determined to be minimal. Similar amplitude dependency is viewed in the dynamic properties for stiffness and viscous damping.

The complete input dataset for the analysis of the signal in Figure 4-11 is tabulated in Table 4-3. The input dataset of Table 4-3 is used to determine the values graphed in the figures below and tabulated in Table 4-4.

Table 4-3 Input Dataset for a single free decay response at step 3

Response amplitude $X_{g1}[m/s^2]$	Response amplitude $X_{g2}[m/s^2]$	Time $t_1 \times 10^{-3}[s]$	Time $t_1 \times 10^{-3}\ [s]$
331.70	196.74	23.83	58.59
196.74	124.03	58.59	92.58
124.03	82.69	92.58	126.95
82.69	56.08	126.95	159.38
56.08	39.44	159.38	192.19
39.44	28.04	192.19	222.66

Table 4-4 Free decay analysis output dataset example at step 3

Average response $X_{avg} \times 10^{-3}[m]$	Natural frequency $f_n\ [Hz]$	Stiffness coefficient $k_{ge}\ [N/m]$	Damping $\zeta_{mec}[\%]$
8.03	28.863	5851.0	8.3
4.67	29.504	6113.8	7.3
3.08	29.151	5968.4	6.4
1.84	30.902	6706.8	6.2
1.30	30.524	6543.6	5.6
0.79	32.869	7587.6	5.4

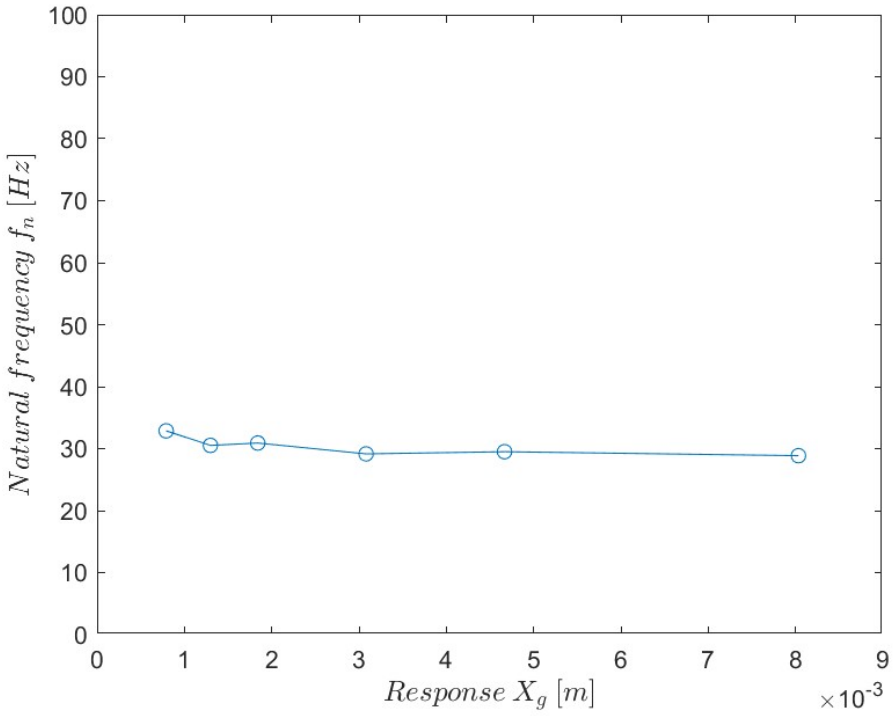

Figure 4-12 Natural frequency of generator at step 3

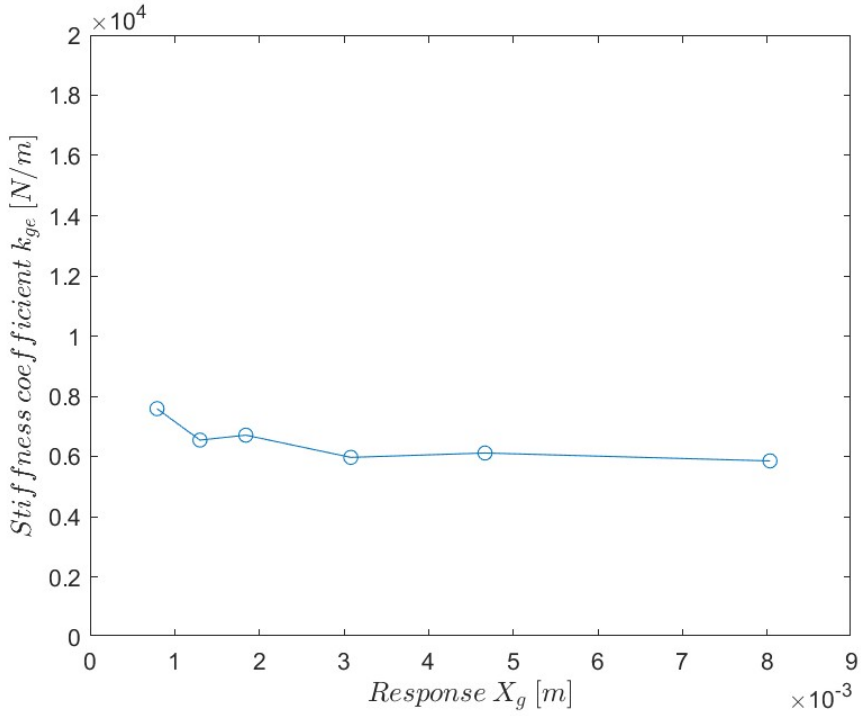

Figure 4-13 Stiffness coefficient of generator at step 3

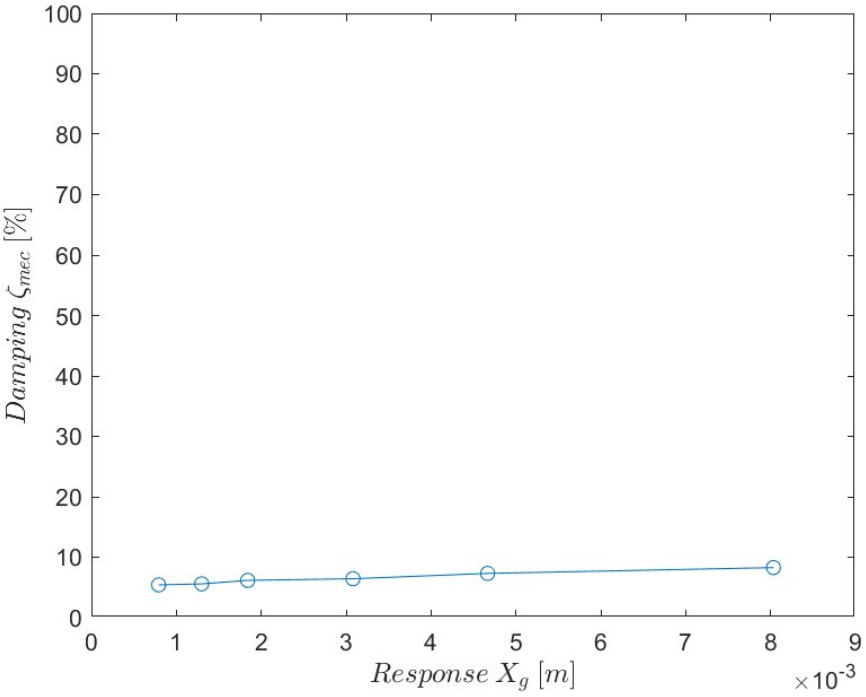

Figure 4-14 Mechanical damping of generator at step 3

4.3.2.4 *In situ* sweep

For confirmation, two *in situ* frequency sweeps were done and graphed in Figure 4-15. The loudspeaker was fixed upon the base that is excited by the shaker motors. The setup allows to induce base excitation of the loudspeaker. The *in situ* frequency sweep test setup is shown in Figure 4-16.

The correct method of measuring the maximum relative response would be through phase and absolute response measurements of the generator and excitation system, which was not followed. The process is too cumbersome for the relative reward and the instrumentation battery power cannot endure the experiment to ensure experimental control.

The 2200 FFT diagnostic instrument can be viewed in Figure 4-16. The response values shown on the diagnostics instrument is recorded manually on the laptop and actively plotted in Microsoft Excel to view the frequency response as shown in Figure 4-15. The frequency sweep data is tabulated in Table 4-5.

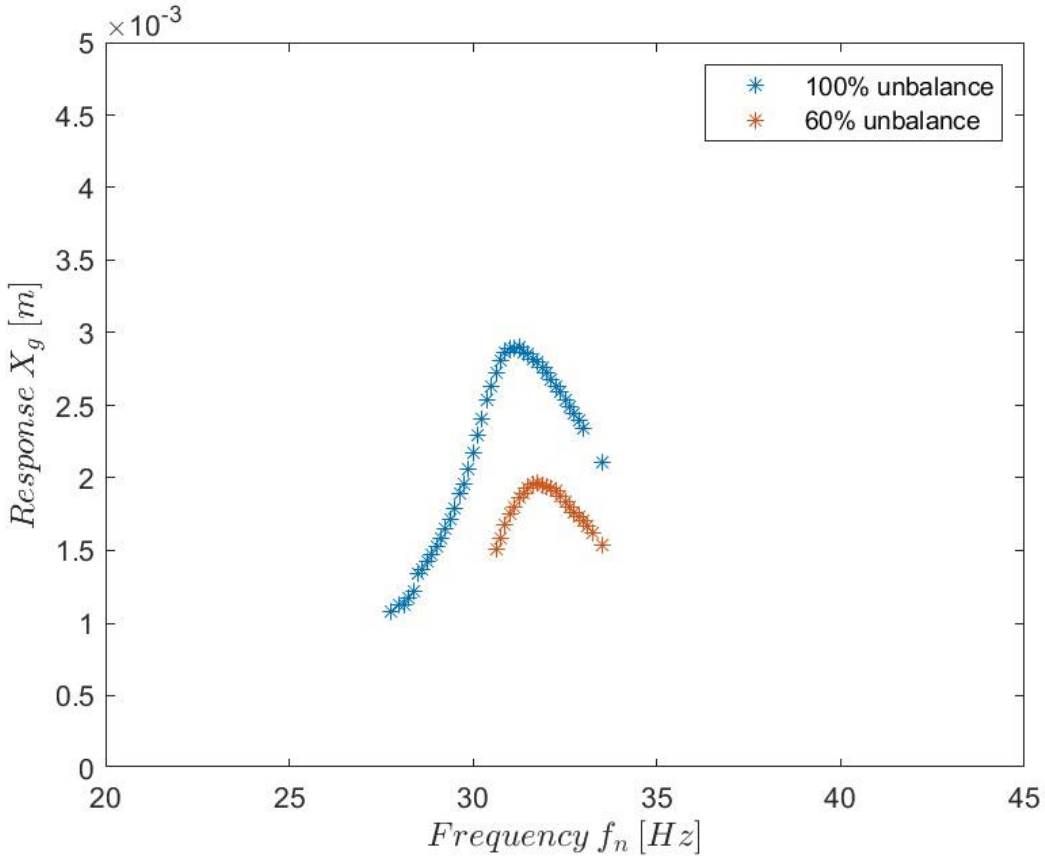

Figure 4-15 In situ frequency sweep

Figure 4-16 In situ experimental setup

Table 4-5 Natural frequency step 4

Test	Natural frequency $f_n\ [Hz]$	Response $X \times 10^{-3}\ [m]$
Frequency sweep	30.125	2.897

4.3.2.5 *In situ* characterization

It was shown that the mechanical properties do not have a vast amplitude dependency. However, incorporating the electrical circuitry changes the dynamic properties. The natural frequencies and dynamic properties for all seven configurations are obtained using the mathematical model as stipulated in paragraph 2.5.2 and implemented as described in Chapter 3.

An example of the characterization is shown for the no load condition, configuration 7, to show the correlation between the frequency sweep, free decay response analysis and *in situ* measuring technique. The 7 configurations specifically correlate to the load conditions listed in Table 4-8 as configuration one to seven. The *in situ* experimental setup is shown in Figure 4-16. The 2200 FFT diagnostic instrument is used to measure the response of the excitation and generator system simultaneously.

Figure 4-17 shows the time domain signal of the steady state response recorded, of the generator and excitation system, respectively. The diagnostics instrument is used to obtain the frequency domain response and the phase as well. The frequency domain response and phase response graphs are shown in Figure 4-19 and Figure 4-20. To determine the phase from measured data requires simple

arithmetic The phase is the difference in the measured values and by subtracting 180 degrees. This is consistently applied across all measurements. For example, the phase in Figure 4-19 is calculated as $ABS(70.1209 + 33.43348 - 180) = 76.44$. This can only be done due to the nature of the measurement instrument.

The response values $\ddot{X}_b = 15.1\, m/s^2$ and $\ddot{X}_g = 114.5\, m/s^2$ and the phase difference $\phi = 76.45°$ are taken as input parameters for the mathematical model *step_5.m* and implemented as described in Chapter 3 to computer software. Solving the equations simultaneously, the output characterised parameters required for prediction can be determined. The natural frequency is $f_n = 31.3\, Hz$, the stiffness coefficient $k_{ge} = 6934.0\, Nm$ and damping is $\zeta = 6.66\,\%$. The characterised values for each load configuration are summarised in Table 4-6. With this example it is shown that all three methods correlate well for characterization purposes with each step iteratively closer to accurate values. The input parameters for evaluation as described in Chapter 3 are used from method and characterization program *step_5.m* for consistency purposes.

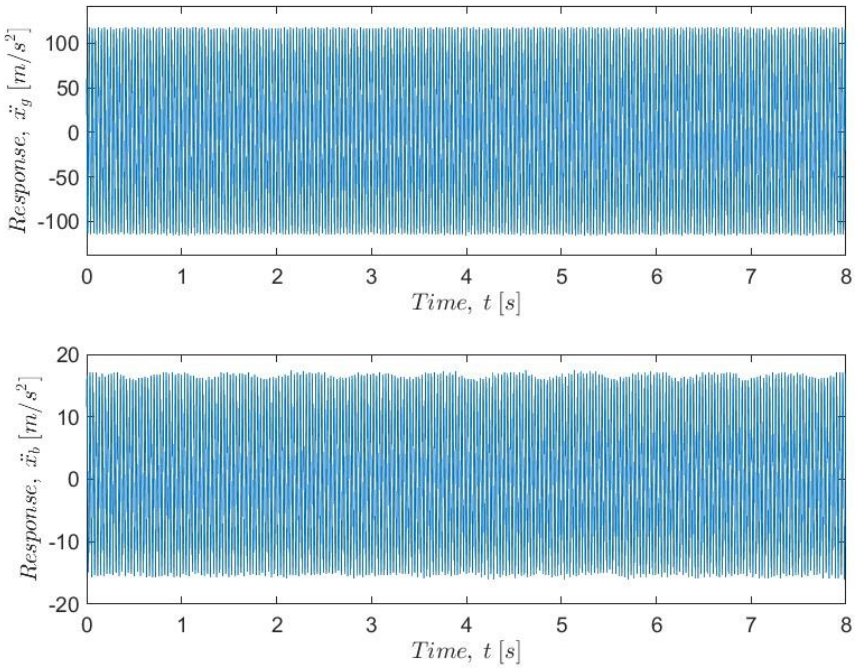

Figure 4-17 Time domain response of generator and base

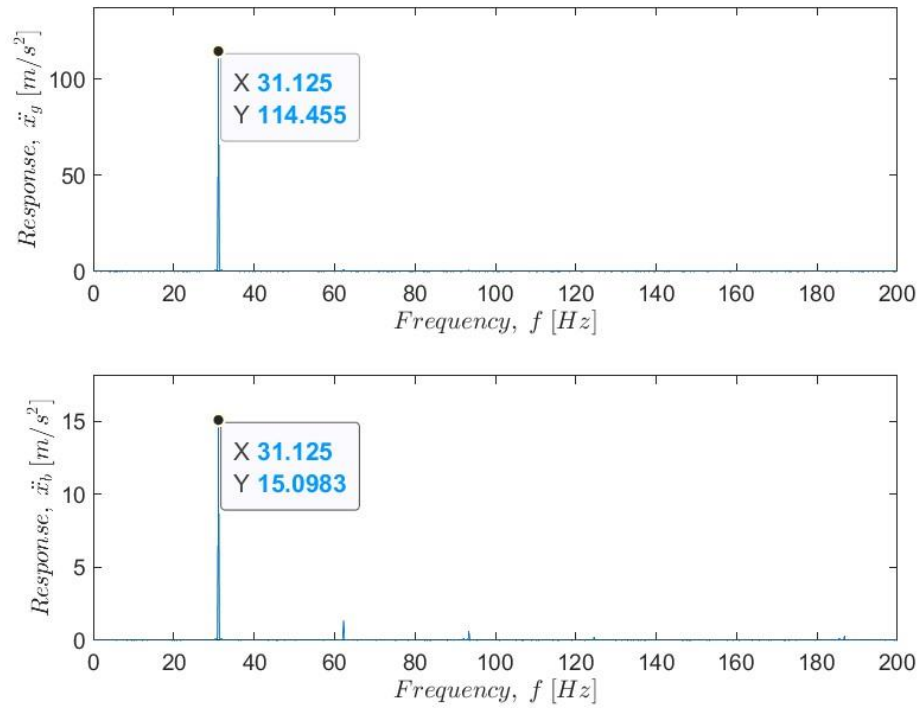

Figure 4-18 Frequency domain response of generator and base

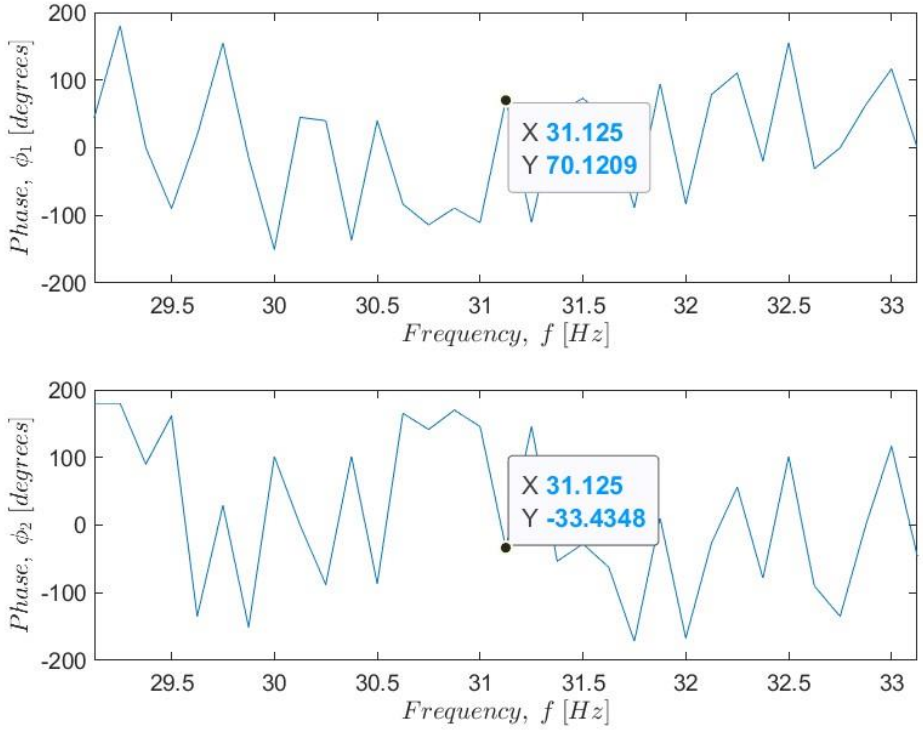

Figure 4-19 Phase measurements

Table 4-6 In situ characterization output data

Configuration	Natural frequency $f_n[Hz]$	Stiffness $k_{ge}[N/m]$	Damping $\zeta[\%]$
1	39.242	10870	38.592
2	34.672	8485.7	25.087
3	33.737	8034.4	18.41
4	32.452	7433.9	11.763
5	32.046	7294.0	10.346
6	31.63	7062.0	8.3827
7	31.342	6934.0	6.6613

For comparison the datasets from all steps are graphed together. The natural frequency in Figure 4-20 is shown for the plane wave tube, free decay analysis, *in situ* frequency sweep and *in situ* characterization. It is clear that the plane wave tube apparatus did contribute to inaccuracy of the characterised data. The values obtained from the plane wave apparatus is seen to be significantly higher for the parameters of stiffness and natural frequency. Results of the in-situ characterization and free response decay analysis closely relate and support these characterised values.

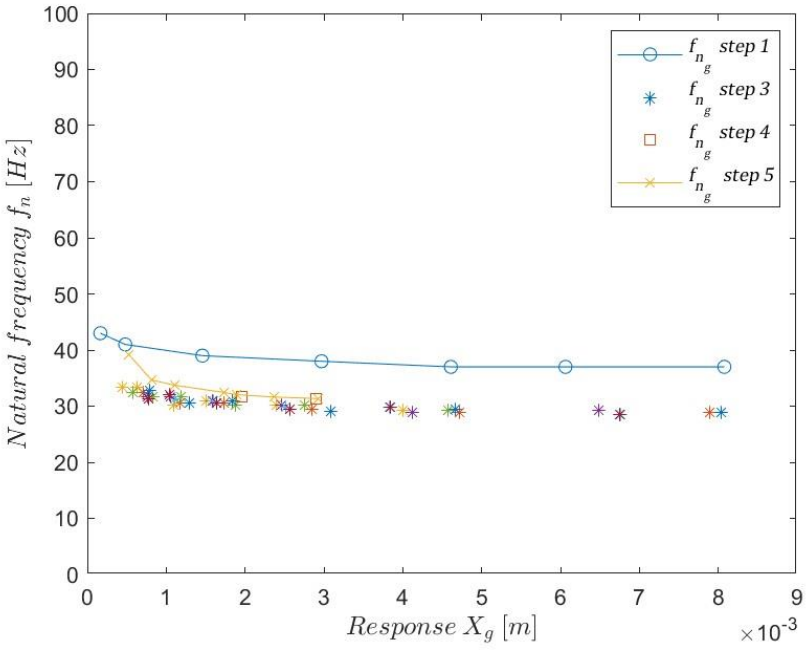

Figure 4-20 Generator natural frequency

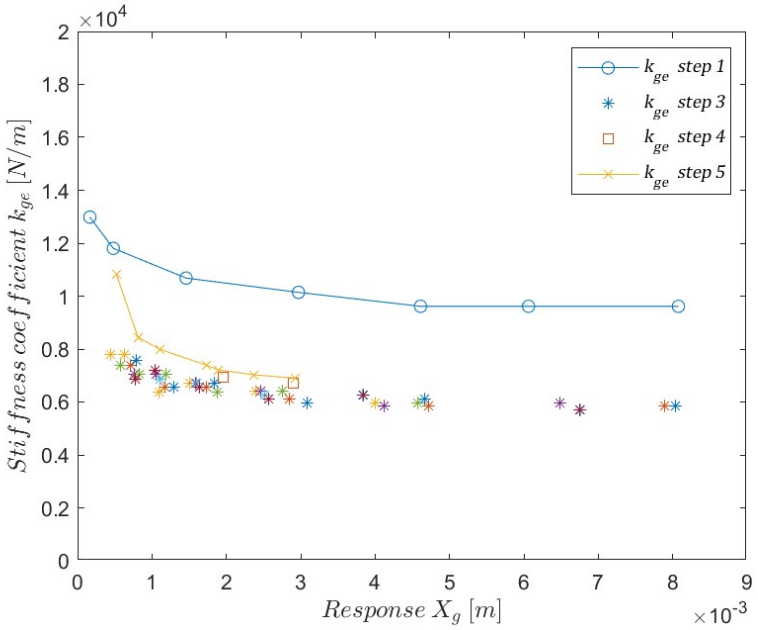

Figure 4-21 Generator system stiffness coefficient

In Figure 4-21 the stiffness characteristic of the generator at the different steps is graphed. The values from step 3, 4 and 5 show consistency with the same trend in amplitude dependency. An single outlier data point for step 5 *in situ* characterization is seen for configuration one. This is due to the extreme condition associated with configuration 1 (this electrical load configuration is discussed later in paragraph 4.4.1). Damping is graphed in Figure 4-22. The generator damping at step 5 *in situ* characterization strongly correlates with damping calculated at step 2, the plane wave tube experiment with variable loads.

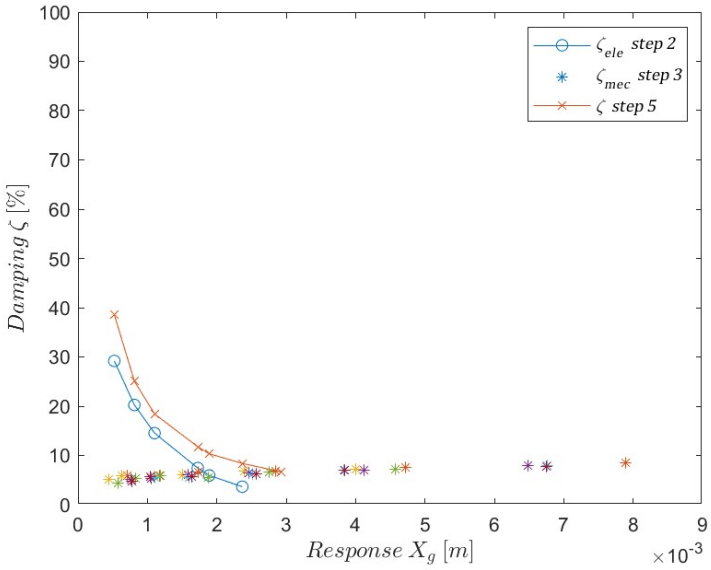

Figure 4-22 Generator system damping

4.4 Generator electrical system

4.4.1 Coil and load resistance

Selected load resistors are placed in an electrical box with switches and LED (light emitting diode) lights that indicate the current configuration of the circuit as depicted in Figure 4-23. Table 4-7 is a list of the switchable load resistors and the resistors for the separated DC circuit that control the interactive LEDs to ensure the state of the electrical circuit.

The instrument used to characterise the resistance of the circuit is the Fluke 17B+ (see Figure 4-3). The Fluke measures accurately to $0.2\ \Omega$. The values are measured with internal resistance such as soldering and wiring of the electrical box.

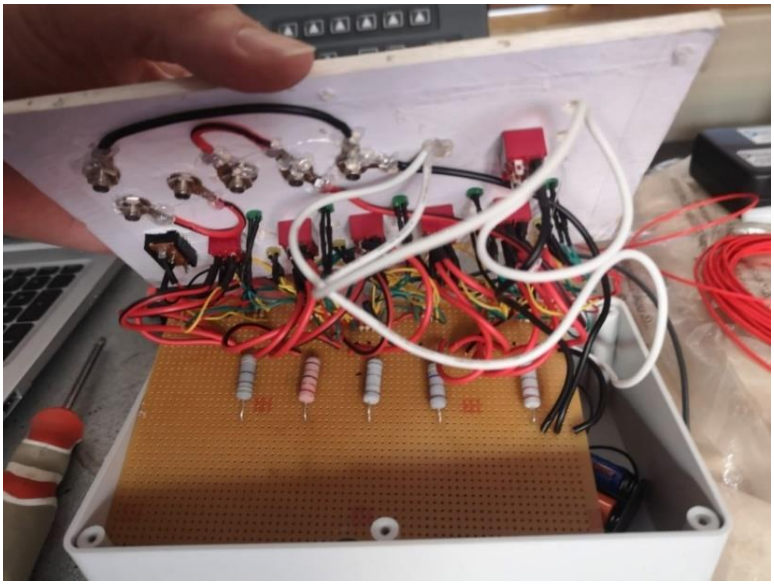

Figure 4-23 Switch box

Table 4-7 Resistors

Configuration	Resistor	Resistance [Ω]
-	R_1	220
-	R_2	330
1	R_{l1}	0.2
2	R_{l2}	2.3
3	R_{l3}	4.6
4	R_{l4}	15
5	R_{l5}	22.3
6	R_{l6}	46
7	R_{l7}	–
Parallel connection	R_c	1.9

The circuit diagram in Figure 4-24 shows the dual circuit design and the utilised load resistors associated with Table 4-7. The DC power supply is only to light the LEDs for ensuring the state of operation referring to different load configurations. The AC circuit is shown in blue in Figure 4-24. The volt and ammeter probes are indicated by the letters V and A. The open terminals of the blue circuit show the connection to the coils connected in parallel. The actual circuitry is seen in Figure 4-23 with the different 5 W load resistors visible on the board. The red blocks are the double throw switches that separate the DC and AC circuits and the black switch is simply to power the LEDs on and off.

In conducting the characterization of the electrical circuitry, the total impedance Z_t, load impedance Z_l and impedance ratio r were then measured and recorded in Table 4-8. The table shows seven different configurations. The load impedance values in Table 4-8 are measured at the respective points of direct connection to the terminals of the loudspeaker. The total impedance is the cumulative load of the load resistor and the coil. The load impedance is the effective load over which the power is calculated. Table 4-8 serves as a summary of the electrical parameters to be used in mathematical models in chapter 5.

Table 4-8 Electrical parameters

Configuration	Load Impedance Z_l [Ω]	Total impedance Z_t [Ω]	Ratio r [-]
1	0.1*	2	0.05
2	2.3	4.2	0.55
3	4.6	6.5	0.70
4	15	16.9	0.88
5	22.3	24.2	0.92
6	46	47.9	0.96
7	-	-	-

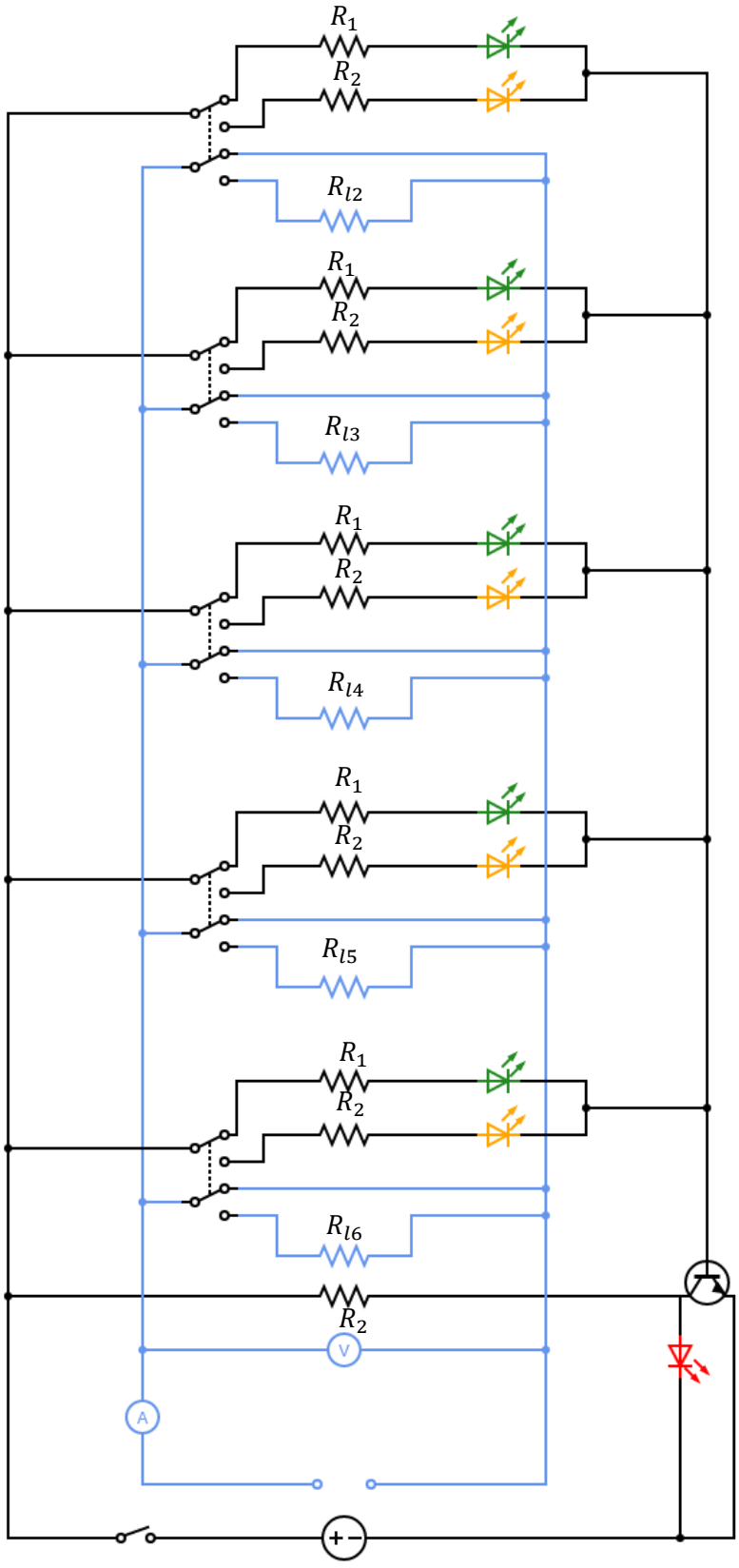

Figure 4-24 Switch box schematics

4.4.2 Coupling factor

The coupling factor is characterised here by two methods as it is a crucial parameter in the mathematical model. The FEMM model shows the magnetic circuit and a simulated value according to materials and geometry. The alternative method more closely examines the amplitude dependency of the parameter and the change due to voice coil connection.

4.4.2.1 Coupling factor measurements

The Plane wave tube is utilised again for measuring the coupling factor BL. During excitation, the response is measured in addition to the induced voltage over the terminals of a coil configuration. The volume setting is used on the amplifier to measure for different BL values in the range of $0\ mm$ to $8\ mm$. The experiment is repeated for different coil configuration, single, parallel and series. The MATLAB program *step_BL.m* calculates the BL value with use of Equation 2-26 and graphs the values in Figure 4-25. Stander deviation is obtained from the MATLAB plot and the coefficient of variations are calculated. The values are determined to be sufficiently low. This supports the assumption that the value remains constant over the travel of the coil. The plot axis could be changed to show the trend more prominently. However, this will be deceptive in comprehending the extend of influence the parameter may have.

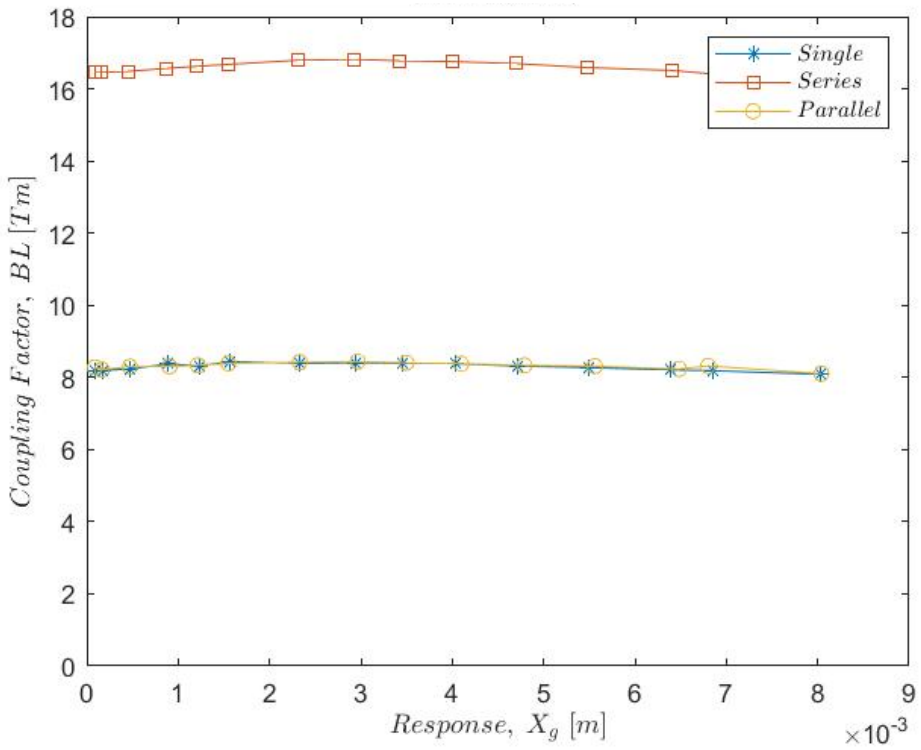

Figure 4-25 Coupling factor

4.4.2.2 Coupling factor simulation

The parameters required for the simulation of the coupling factor were recorded and the coil dimensions measured. Then the magnetic materials were listed and the dimensions were tabulated. The result of the FEMM analysis is shown with a value for the coupling factor. The coupling factor is then compared to the measured values from paragraph 4.4.2.1.

The micrometre is a general engineering measuring instrument used to measure the dimension of the coil. The coil height and diameter are obtained from the Thiele-small parameters. The wire dimension is measured on 10 different sections. The average diameter of the repeated measurements gives the approximate dimension for the wire, which corresponds to a commercially available 26-gauge wire. The values for the dimensions of the coil are tabulated in Table 4-9. The dissected coil and micrometre is shown in Figure 4-26.

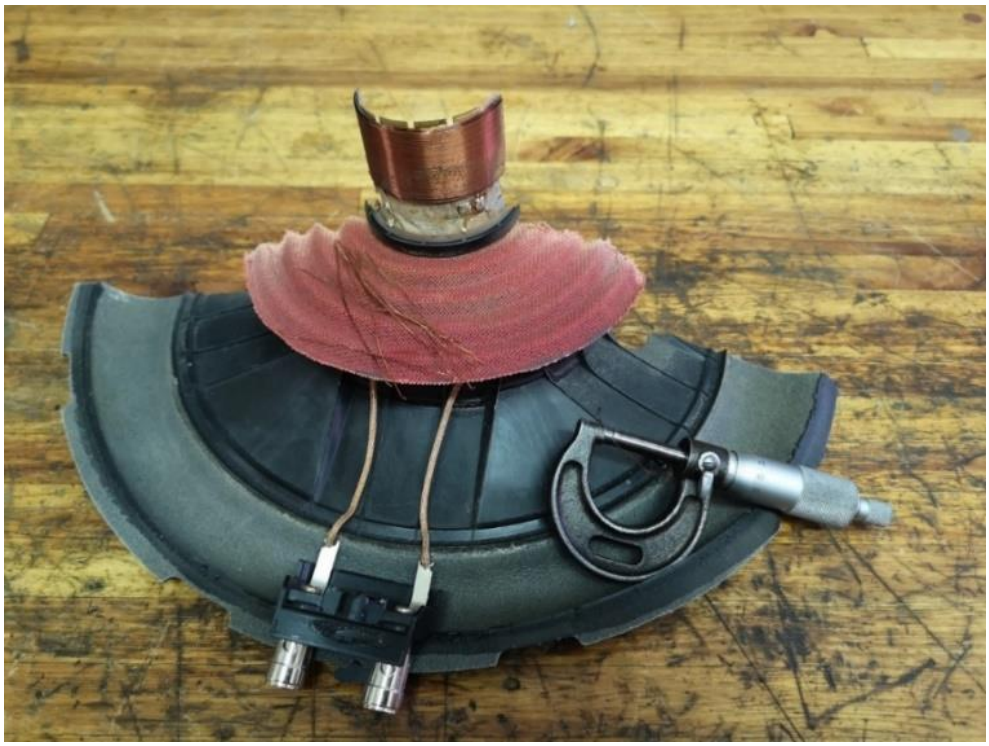

Figure 4-26 Coil dimensions

Table 4-9 Measured coil dimensions

Parameter	Value	Units
Coil height	31.6	mm
Wire	0.45	mm
Number of turns	140	$per\ coil$
Coil diameter	48	mm

The FEMM simulation requires accurate geometric representation around a symmetrical axis. Figure 4-27 shows a sketch of the dimensions used. Furthermore, FEMM requires material selection. Standard materials listed in the software package is sufficiently accurate. The materials are shown in Table 4-10. The simulation is configured as a single coil. A theoretical experiment is completed with use of the simulation software and the BL value is obtained. Colourful results of the simulation show the magnetic lines and field strength in Figure 4-28.

Table 4-10 Magnetic circuit properties

Symbol	Material
A	Powdered iron, sintered and annealed
B	Ceramic 5
C	Air
D	26 AWG

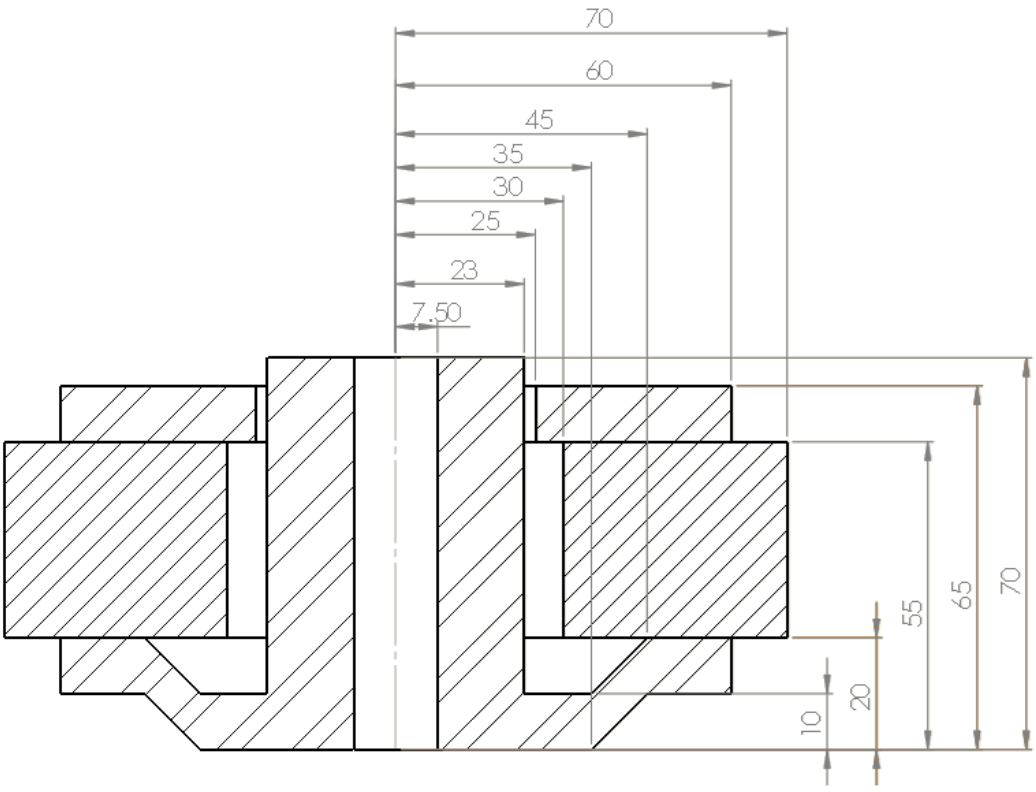

Figure 4-27 Magnetic circuit dimensions

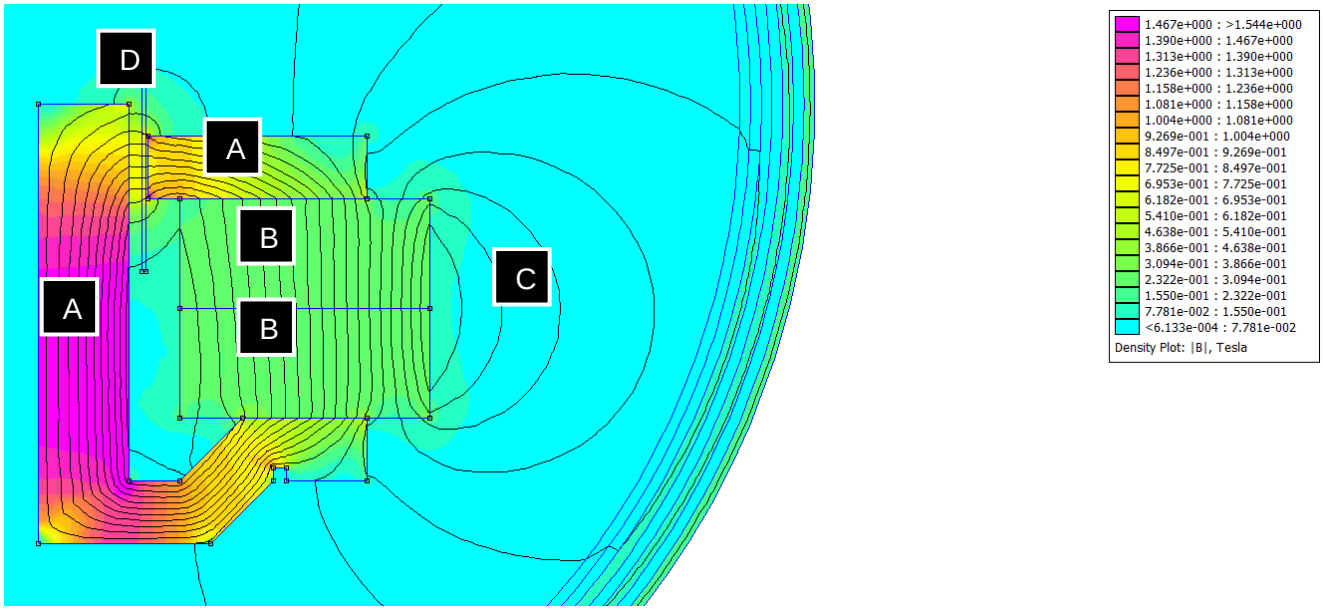

Figure 4-28 Simulation results and material allocation of magnetic circuit

Table 4-11 Coupling factor

	Simulation	Measured	Manufacturer
Coupling factor	8.1	8.29	8.2

4.4.3 Coil inductance

As was evident from the literature survey, several authors opt to neglect the inductance of the coil, due to the simple reason of either low operating frequencies and or low contribution to the total impedance of the coil. The manufacturing specification mentions a coil inductance of $L_c = 1.23\,mH$. Given that a single coil has the resistance of $3.9\,\Omega$ at a maximum operating frequency of $f = 39\,Hz$, in the worst-case scenario coil inductance only contributes to 3% total impedance of the coil. Equation 2-30 is used to determine this value. This justifies that the power factor can be assumed to be zero ($pf = 0$).

4.5 Excitation system

The properties for the excitation system are described below. The properties included are for the mathematical models depicted in paragraph 2-4. To model the base excitation system ensures a safe experimental setup and a predictable, steady state vibrational source for the generator. First the mass properties are determined with alternative methods such as measurements and simulation, whereafter approximate modal frequencies and dynamic properties are shown for consideration.

Due to financial considerations, available materials were used in the design of the excitation system. The metal structures are used to elevate the generator and prevent proximity to the vibration motors. This is to ensure the generator does not experience any of the fluctuating magnetic fields originating from the motors. Thus, the concept for the base excitation system is used as depicted in Figure 4- 29.

4.5.1 Mass properties

SolidWorks software was utilized to render the base structure in 3D. The available materials were set up in SolidWorks and the structures were virtually realized. The material properties are taken to be common commercial steel. Material properties and dimensions of each component were simulated. Through the use of SolidWorks, the mass was calculated, which excludes bolts and nuts. The complete structure as measured in reality as recorded in Table 4-11 with all other relevant values of mass. The equivalent mass of the excitation system was then determined and tabulated in Table 4-12 for use in mathematical models.

Table 4-12 Excitation system measured mass

Component	Measured mass m_{be} [g]
SolidWorks	94050
Measured	94050
Motors	6.3
Speaker alt mass	6.0

Table 4-13 Excitation system equivalent mass

Component	Measured mass m_{be} [g]
Excitation system	94050

4.5.2 Dynamic properties

With the excitation system virtually represented in SolidWorks a simple frequency analysis was done. The first eight modal frequencies are tabulated in Table 4-14. It is clear that the operating frequency range is between modes 6 and 7. It illustrates the success of the design attempt to reduce force transmissibility and eliminate resonance at structural frequencies. The bounce mode and 3D rendering of the structure is illustrated in Figure 4-29.

Table 4-14 First 8 modal frequencies

Natural frequency mode	frequency f_n $[Hz]$
1	0.93131
2	1.2262
3	2.716
4	3.5133
5	3.7945
6	3.7959
7	76.909
8	83.373

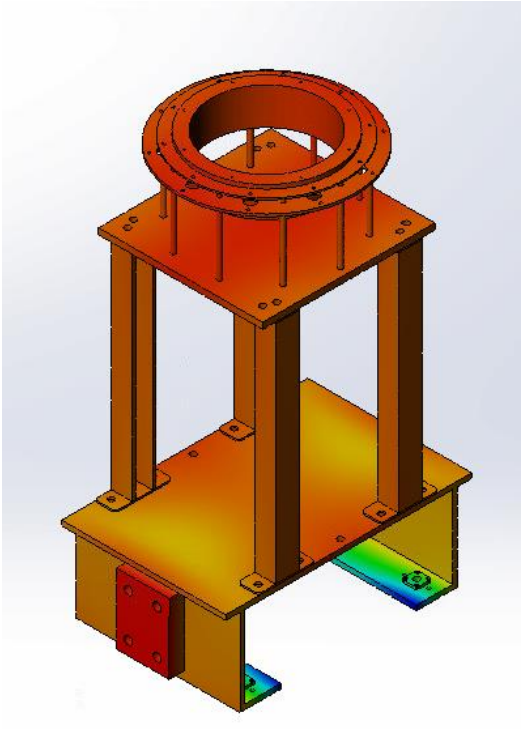

Figure 4-29 Bounce mode 3.51 Hz

At the end of manufacturing and the final assembly of the excitation system, measurements were taken to determine if simulation was acceptable. A free decay response was induced and measured. The recorded response is depicted in Figure 4-30. The response is analysed using the same methods as for the generator system in free decay analysis. The dynamic properties that were obtained from the analysis is graphed in Figure 4-31 to Figure 4-33. The Natural frequency is in the expected range as designed and simulated in SolidWorks. The stiffness coefficient and damping are graphed in Figure 4-32 and Figure 4-33 respectively. The results are jagged and only approximations. A more accurate results could be obtained with a greater resolution on the time domain response recording. The values used for the mathematical models are tabulated in Table 4-14.

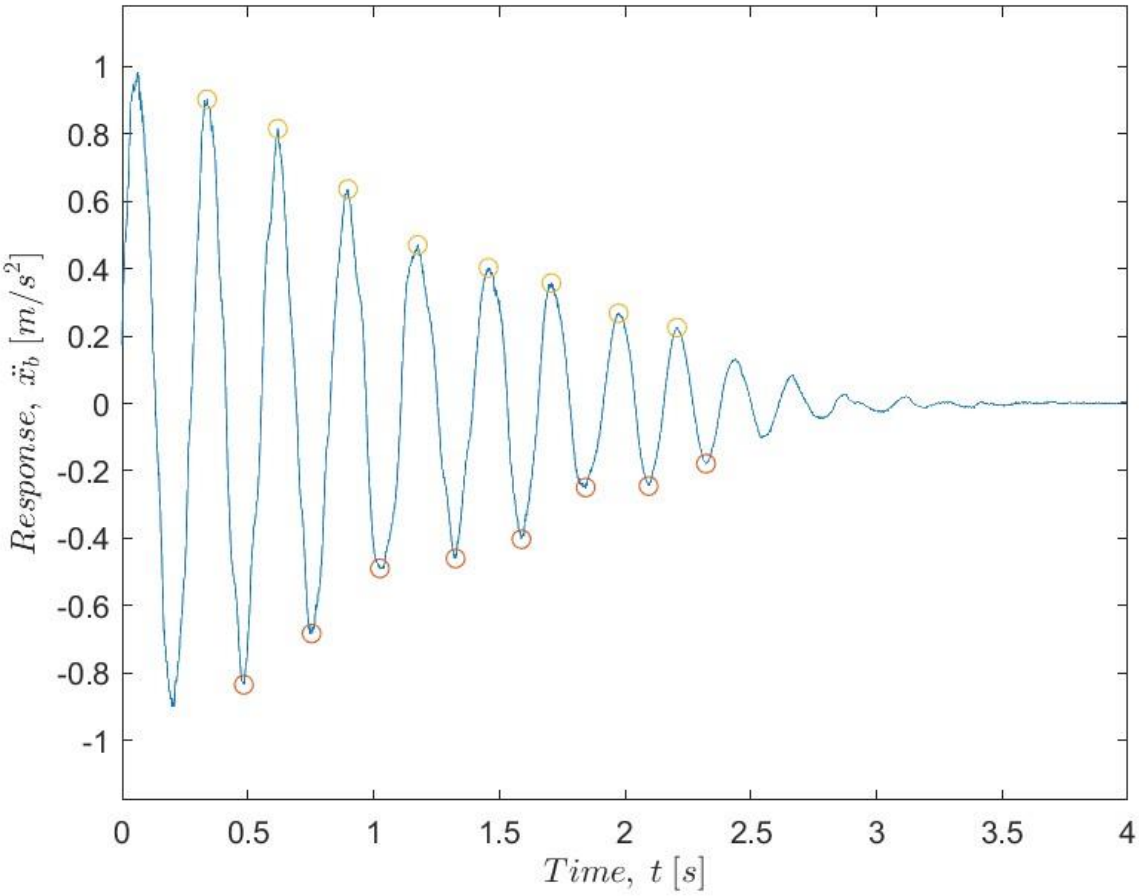

Figure 4-30 Excitation system free decay response

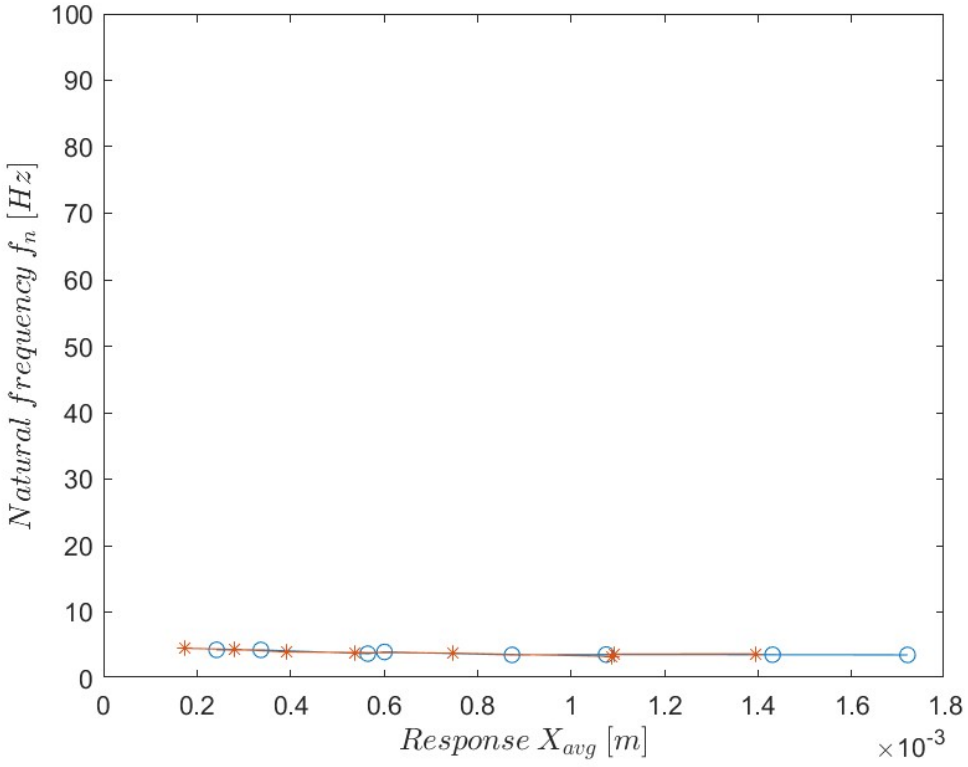

Figure 4-31 Excitation system natural frequency

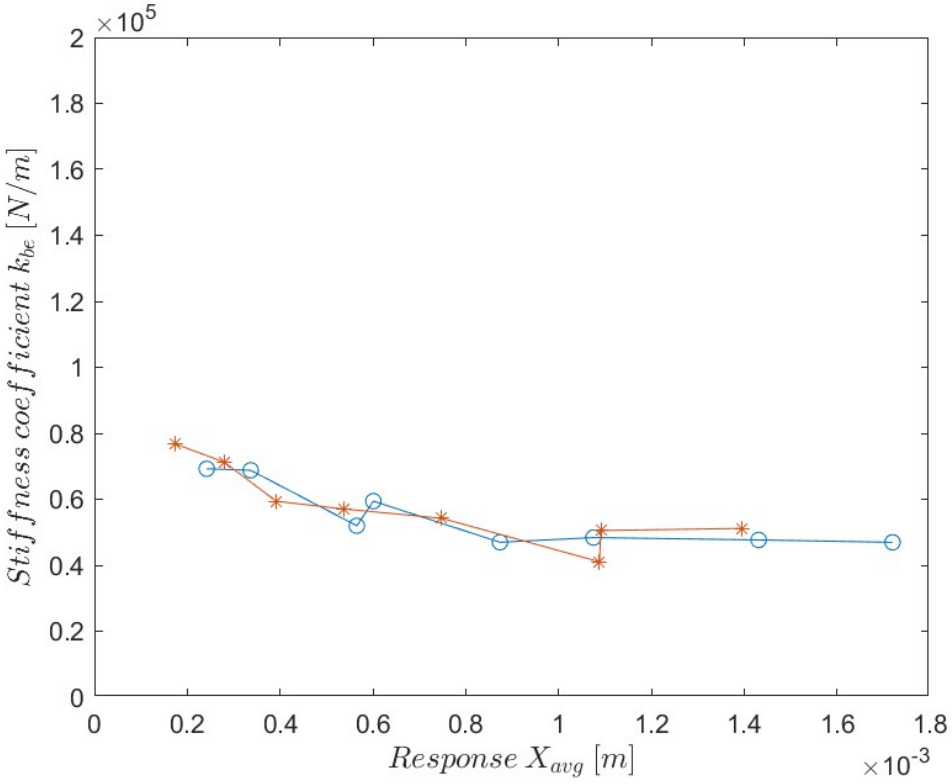

Figure 4-32 Excitation system stiffness coefficient

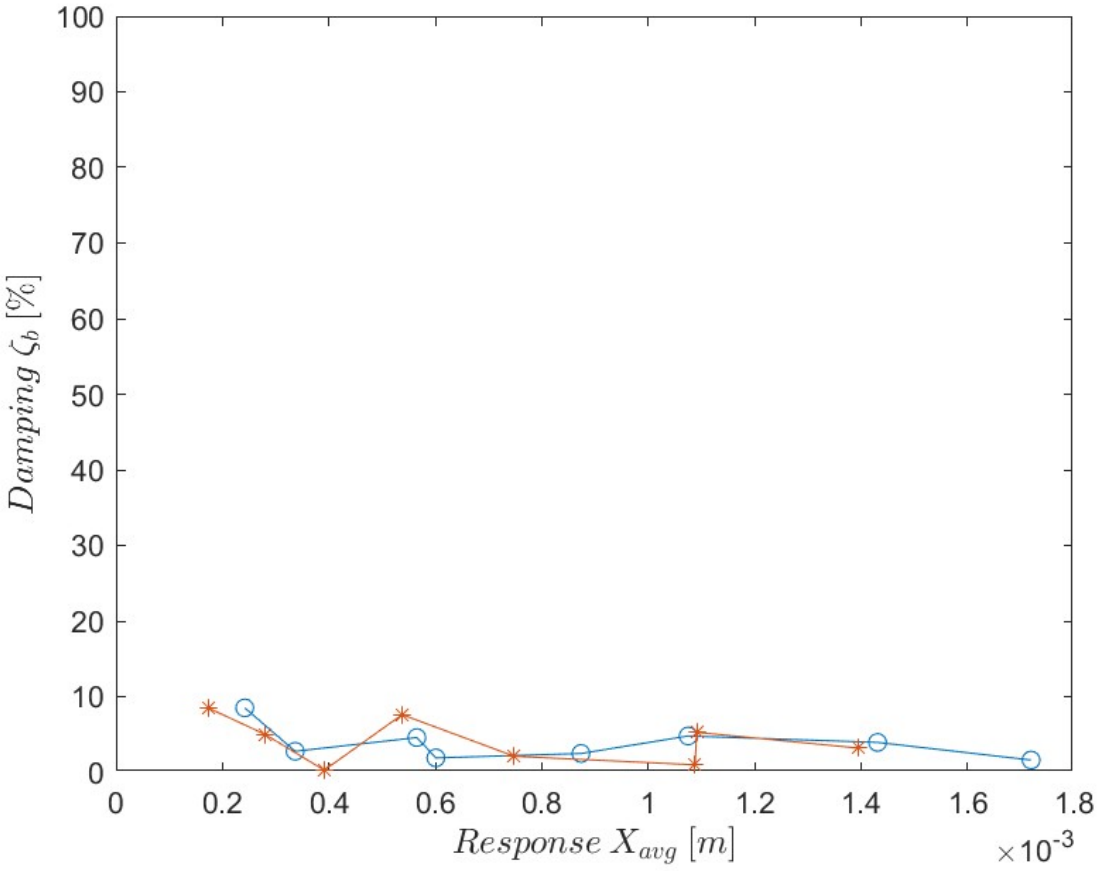

Figure 4-33 Excitation system damping

Table 4-15 Base excitation characteristics

Mass	Stiffness	Damping	Natural Frequency
m_{be} [g]	k_{be} [N/m]	ζ_b [%]	f_n[Hz]
94050	54923	4	3.88

4.6 Conclusion

The mechanical and electrical parameters required for predicting the response, mechanical and electrical power in each component was successfully characterised. The mechanical structure shows some amplitude dependency. The coupling factor was successfully simulated and measured *in situ*. The operating frequency for the different load configurations was identified. The mechanical and electrical characteristics compare well in order of magnitude to the values obtained from the supplier. Inductance L_c of the coil is shown to be neglectable. The next chapter entails evaluation of the models using the characterised values as input variables to the models described in Chapter 5.

Chapter 5 Experimental evaluation

5.1 Introduction

The experimental evaluation chapter summarizes the predicted values of the mathematical models of Chapter 2 in comparison with the measured values obtained from the vibration energy generator. Mechanical values pertain to relative response of the generator to the base excitation structure, associated dynamic forces and the power dissipated in the mechanical system. The electrical parameters that are summarized are the values of load voltage, induced current and power dissipated in the electrical system. The summaries of evaluation consider different conditions at the vibration energy generator. The different conditions refer to specific configurations (configurations 1 to 6) as described in Chapter 4.

Figure 5-1 Evaluation setup

The test setup used for evaluation is captured in Figure 5-1. The loudspeaker implemented as a generator is seen fixed to the yellow structure. Wires leading to the variable load box are the connections between the active load corresponding to a specific configuration and the coils inside the speaker, completing the circuit as in Figure 2-2. A green light is visible in the figure to illustrate configuration 1. The circuitry switches allow the active load to be varied to correspond with a specific configuration.

Two 2200 FFT Diagnostic instruments are used - one to capture the electrical measurements and the other to capture the mechanical response. The mechanical response is measured in positions shown in Figure 5-2 and Figure 5-3. The smaller Dytran sensor is preferable in measuring the response of the

generator and is used consistently throughout characterization and evaluation. The Dytran sensor is seen fixed in the centre of the diaphragm as seen in Figure 5-3. The excitation system response is measured by fixing the larger PCB sensor to the bottom of the horizontal fixed blue plate as pictured in Figure 5-2.

Figure 5-2 PCB sensor mounted

Figure 5-3 Dytran sensor mounted

The electrical parameters are measured using the circuitry as shown in Figure 5-4. The voltage V_l is measured simultaneously with the response of the base excitation system $x_b(t)$ using the 2200 FFT diagnostic instrument. The magnitude of the current is measured with the Fluke 17B+, read digitally and recorded manually. The voltage probes and current measure setup is shown in Figure 5-4. The switches for different load condition is also seen in Figure 5-4.

Figure 5-4 Multi meter and switch box

5.2 Excitation system

The excitation system evaluation is addressed first. The evaluation is only important to show that the design process and simulation was sufficient to construct an experimental setup. The response values during the evaluation experiment and the modelled response values are reported for comparison. The values are tabulated below in Table 5-1. The modelled values are obtained by using the parameters of Table 4-13 and Table 4-15 and the MATLAB program *step_base.*m. The characterised and operation frequencies of the final evaluation experiment is used for simulation and comparison reasons. The average error is 9%.

Table 5-1 Excitation system evaluation

Configuration	Frequency $f_o\ [Hz]$	Modelled $X_b \times 10^{-3}\ [m]$	Measured $X_b \times 10^{-3}\ [m]$
1	39.25	0.435	0.403
2	34.63	0.436	0.408
3	33.75	0.437	0.407
4	32.5	0.437	0.406
5	32.0	0.437	0.393
6	31.63	0.437	0.397
7	31.12	0.438	0.396

The results of the excitation system response evaluation show that acceptable assumptions and mathematical models are used to determine the steady state response of the excitation system. This is important as the modelled values are used to determine the possible response of the highly sensitive speaker before actual testing of the generator. A reasonably predictable excitation system allows a safe commissioning of the experimental setup.

5.3 Mechanical system

Table 5-2 summarises the relative response X_r that is predicted by the mechanical model and is evaluated against measured data. A typical signal that is measured, at configuration 4, is illustrated in Figure 5-5 to Figure 5-7. The time domain signal is recorded to illustrate the simultaneous observations of the excitation system and the generator moving mass in Figure 5-5. The frequency domain of the same signal is viewed in Figure 5-6, showing the predominant excitation frequency.

In Figure 5-6 the excitation frequency of $f = 32.5\ Hz$ and amplitudes of $X_b = 1.72\ G$ and $X_g = 7.57\ G$ can be viewed. At the exact frequency f, the phase is measured $\phi = 76.7\ °$. This is illustrated in Figure 5-7. Each configuration is measured and evaluated in the same way. The predictions are obtained with input parameters from Table 4-6 and using MATLAB model *Pred_mec.m*. The results for the relative

response and phase of the MATLAB program are tabulated in Table 5-2 and 5-3 in comparison with the measured data.

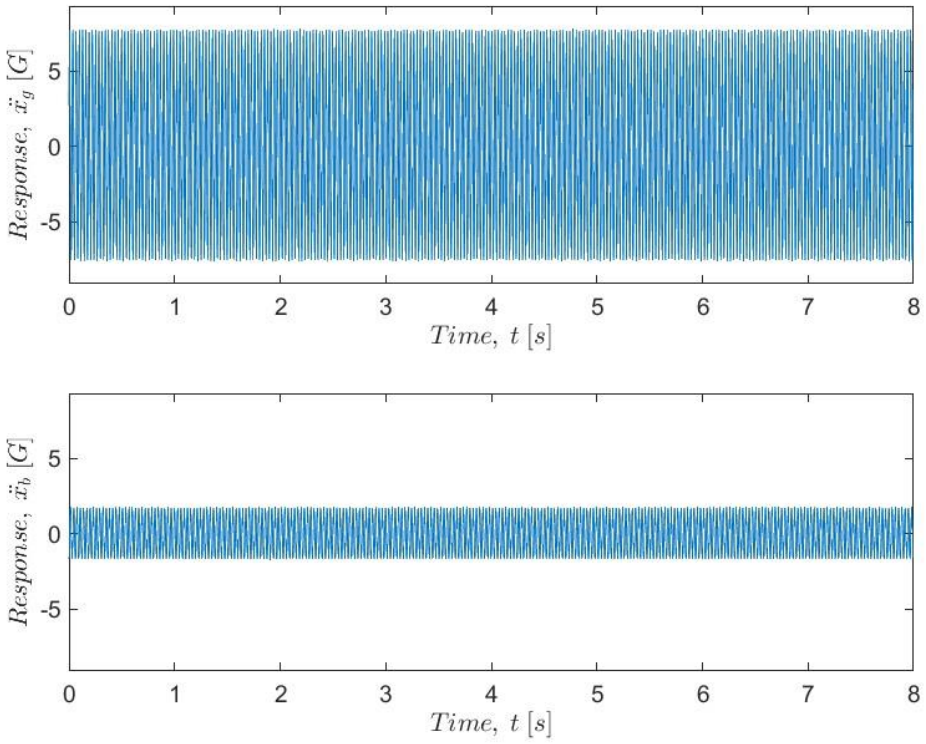

Figure 5-5 Time domain response of generator and base

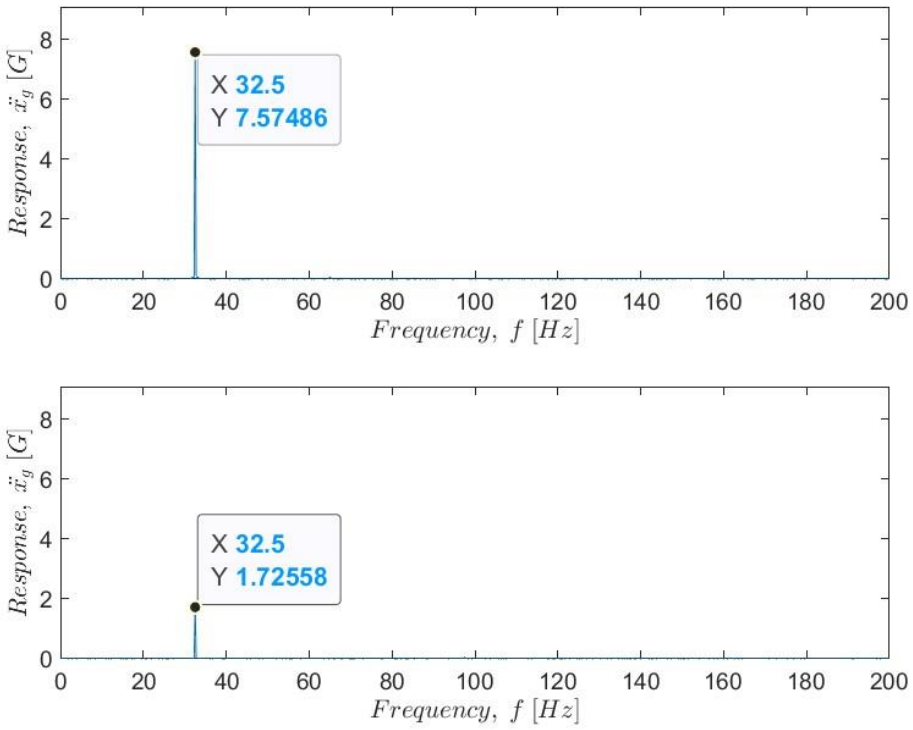

Figure 5-6 Frequency response of generator and base

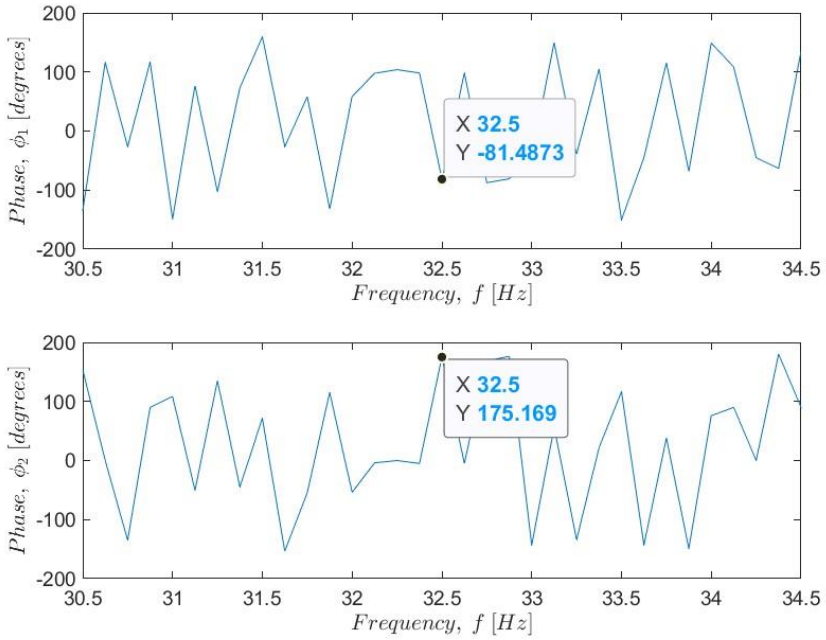

Figure 5-7 Phase measurement

Table 5-2 Relative response X_r

Configuration	Predicted $X_r \times 10^{-3}[m]$	Measured $X_r \times 10^{-3}[m]$	Error [%]
1	0.52	0.54	2.6
2	0.81	0.80	1.7
3	1.10	1.07	3.1
4	1.73	1.73	0.5
5	1.89	1.89	0.2
6	2.37	2.36	0.4
7	2.93	2.88	1.5

Table 5-3 Phase evaluation

Configuration	Predicted ϕ [degrees]	Measured ϕ [degrees]	Error [%]
1	52.4	52.4	0.1
2	63.1	63.6	0.8
3	69.9	69.6	0.3
4	77.3	76.7	0.9
5	77.2	82.3	6.2
6	80.4	78.8	2.0
7	76.4	71.6	6.7

Mechanical system response and phase value evaluation shows that valid characterization methods and accurate characterization values were used and determined in Chapter 4. Furthermore, that the successive calculated power values will be accurate, including the power at each component in the mechanical system. It is pertinent that the values reflect reality as the calculated usable power is compared to the electrical system usable power in a later section.

5.3.1.1 Power and power signal

Dynamic forces in the mechanical system are determined with use of the predicted data. Vector representation of the dynamic forces shows the equilibrium between the excitation force and the reaction forces transmitted to the generator. Vector representation for configuration 4 is seen in Figure 5-8. The excitation force is a constitution of the vector forces F_{kb} and F_{cb}. Dynamic forces associated are tabulated in Table 5-4. Furthermore, the power at each component is tabulated in Table 5-5 for the configuration 4. Instantaneous power is graphed in Figure 5-9. Usable power is tabulated in comparison with the usable power measured for evaluation of the mathematical model and characterised parameters in table 5-6.

Table 5-4 Dynamic forces

Configuration	$F_k\ [N]$	$F_c\ [N]$	$F_m\ [N]$	$F_{kb}\ [N]$	$F_{cb}\ [N]$
1	7.14	5.51	7.14	4.36	3.37
2	7.69	3.85	7.67	3.45	1.73
3	9.40	3.46	9.40	3.25	1.20
4	13.09	3.08	13.12	3.00	0.71
5	13.99	2.89	13.95	2.83	0.59
6	16.87	2.83	16.87	2.79	0.47
7	20.68	2.74	20.39	2.73	0.36

Table 5-5 Power at each component for configuration 4

$P_k\ [W]$	$P_c\ [W]$	$P_m\ [W]$
2.25	1.06	2.26

The sinusoidal power values graphed in Figure 5-9 illustrates the concept of power dissipation solely through the damper element as proposed by French (1971). The usable power is seen in the graph in phase with the power dissipated in the damper element. The unique traversal of power between the mechanical mass and the spring element is seen in the signals that are out phase with same magnitude.

Evaluation of the usable power values is supported by the validity of the power values and dynamic forces calculated above. Validity of the values are proven by the results being consistent with theory and that the dynamic force vector diagram below forms a closed diagram. The valid usable power calculated by the mechanical model can confidently be compared to the electrical model.

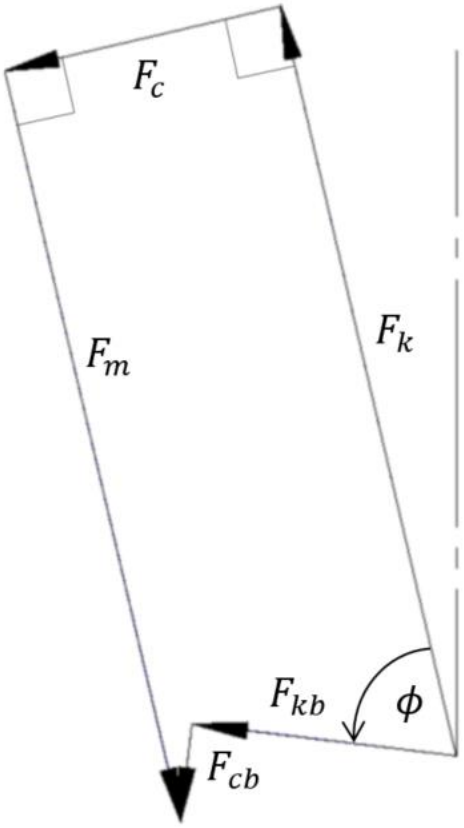

Figure 5-8 Vector diagram for configuration 4

Table 5-6 summarizes the usable power calculated and predicted. Values for configuration 1 and 7 are excluded. In configuration 1 the load resistance is simply too small to accurately determine the usable power, and in configuration 7 there is no electrical load to determine the usable power. The other values compare very well with the measured values. The average error is 1.5%.

Table 5-6 Usable power comparison

Configuration	Mechanical Predicted P_{um} [W]	Measured P_u [W]	Error [%]
1	–	–	–
2	0.13	0.13	0.39
3	0.18	0.19	1.95
4	0.22	0.23	2.00
5	0.19	0.20	3.24
6	0.14	0.14	0.30
7	–	–	–

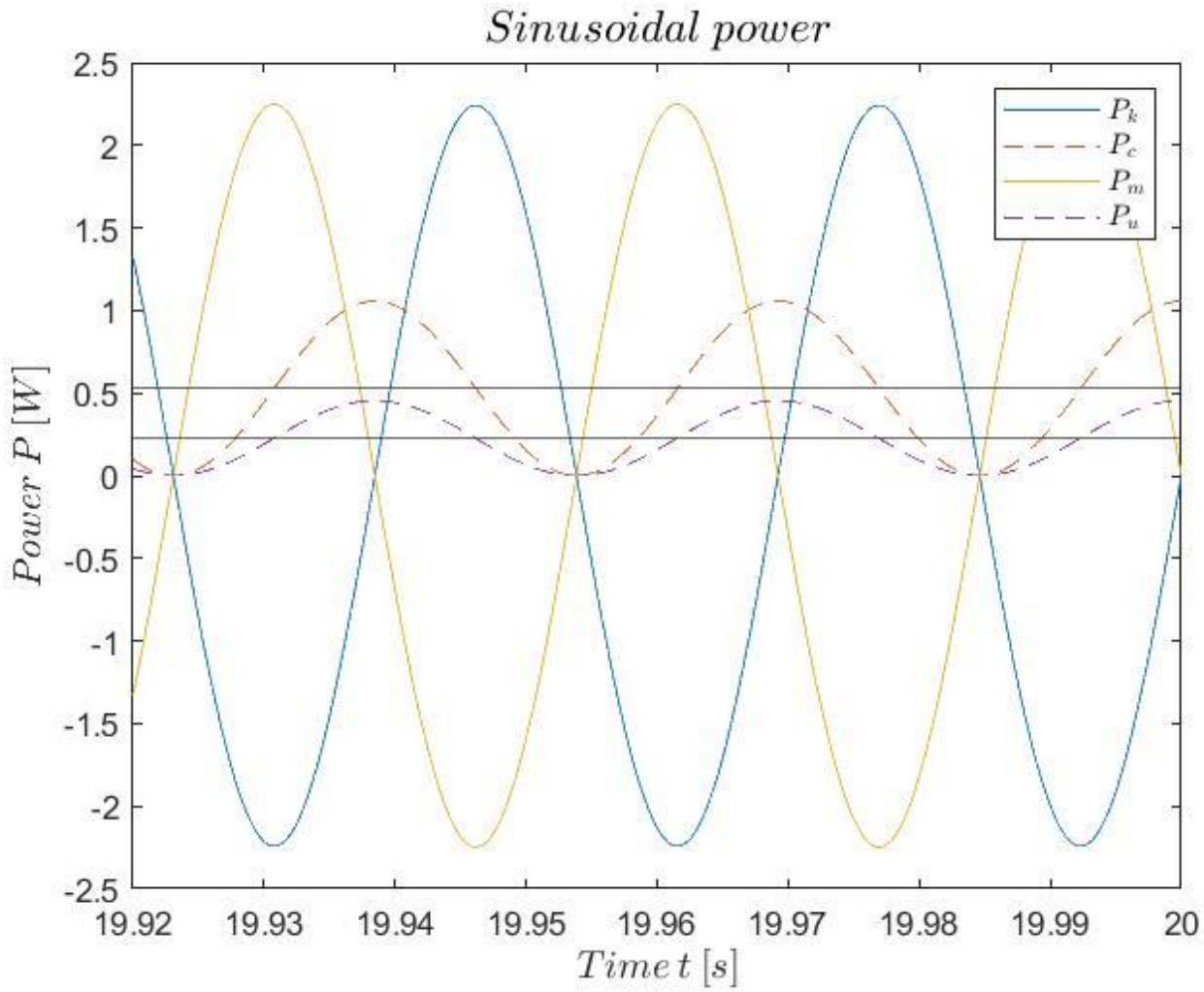

Figure 5-9 Power signals

5.4 Electrical system

The measured electrical parameters are summarised in Tables 5-7 to 5-9. For the load voltage and induced current parameters, the predicted values are compared to the measured values. The measured signals for configuration 4 is reported in the Figure 5-10 and Figure 5-11. The time domain signal is seen in Figure 5-10 where the base excitation and load voltage is measured simultaneously. Figure 5-11 is the frequency domain of the signal seen in Figure 5-10. The load voltage at rms value is $V_l = 0.906\, V_{rms}$ at the same operating frequency seen in the mechanical system $f = 33.75\, Hz$. The digital reading on the ammeter was recorded with rms value $I = 0.201\, A_{rms}$.

The predicted values are obtained using the evaluated relative response X_r in unison with the MATLAB program *Pred_ele.m*. As per example configuration 4, the evaluated response is $X_r = 0.54\, mm$, the predicted load voltage is $V_l = 0.75$, induced current $i_s = 0.33$ and usable power $P_{ue} = 0.23$.

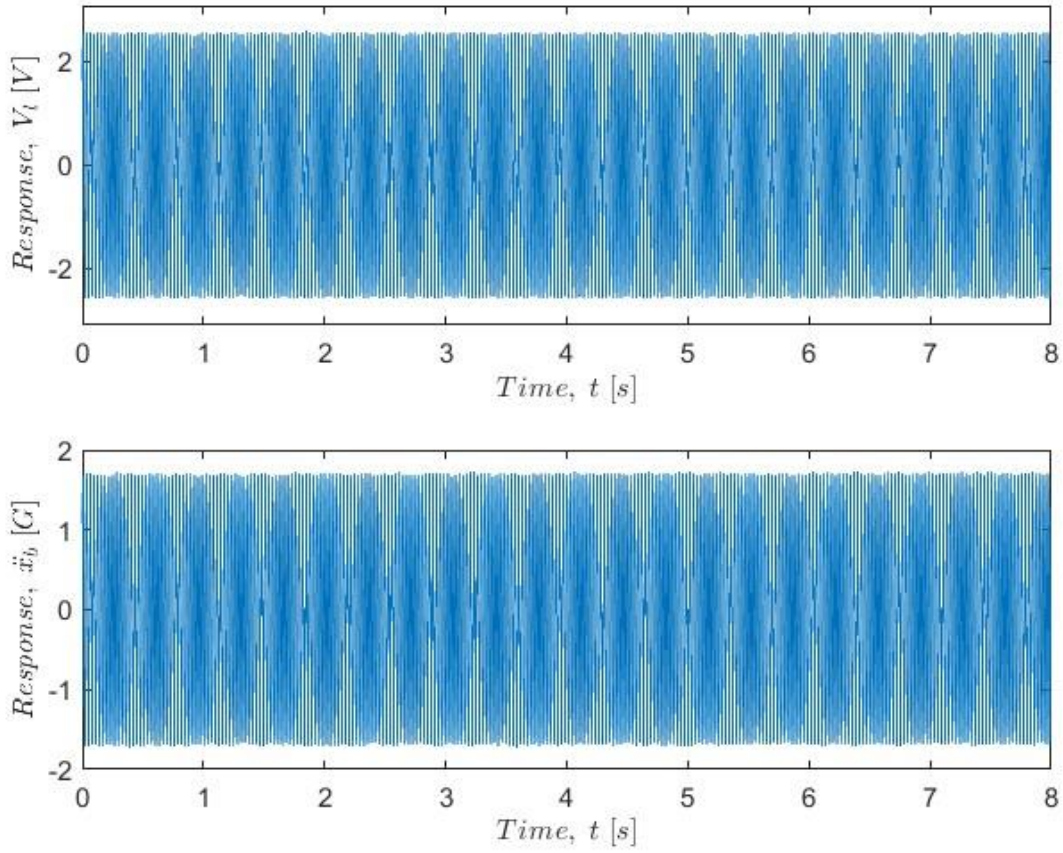

Figure 5-10 Generator and base time response (configuration 4)

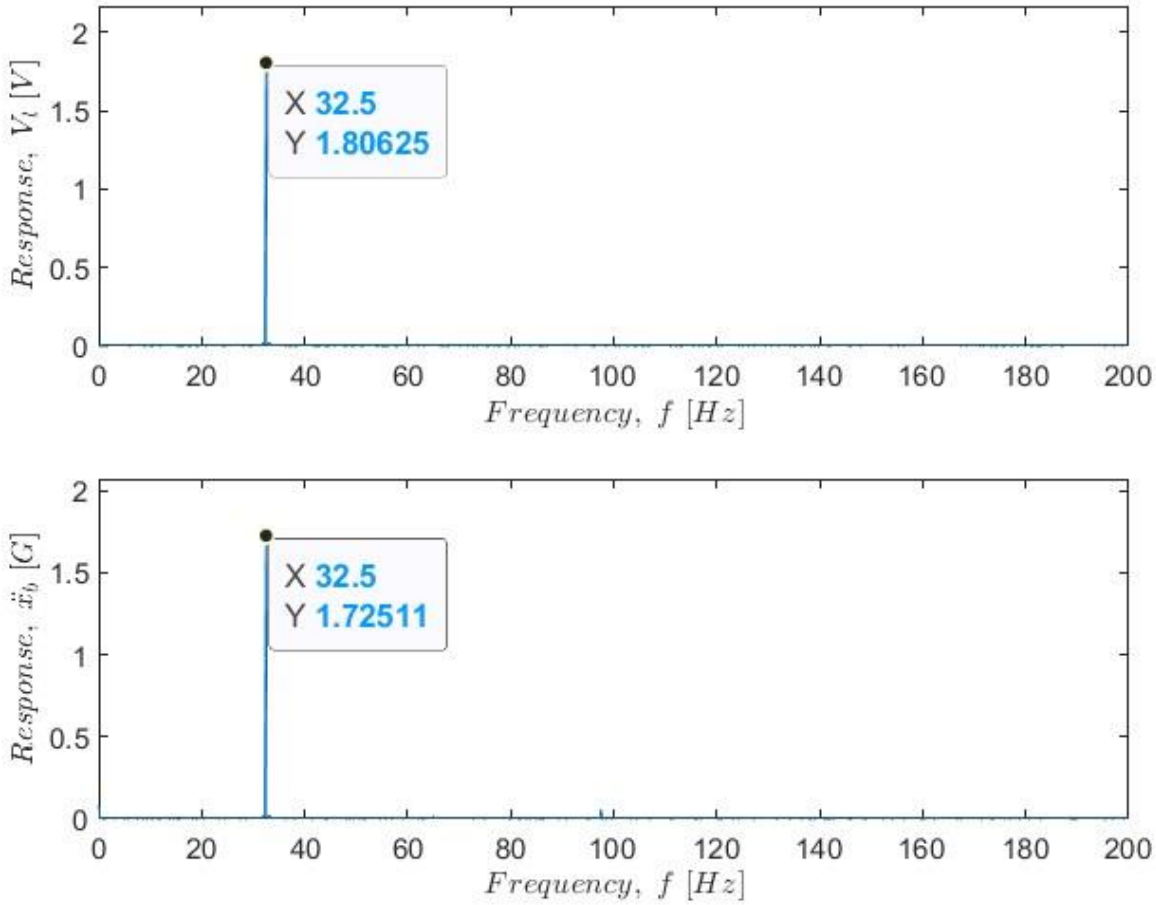

Figure 5-11 Generator and base frequency response (configuration 4)

Table 5-7 Induced current

Configuration	Predicted I_s [A]	Measured I_s [A]	Error [%]
1	–	–	–
2	0.34	0.33	2.87
3	0.29	0.28	2.00
4	0.17	0.17	0.03
5	0.13	0.13	2.74
6	0.08	0.08	2.52
7	–	–	–

Table 5-8 Load voltage

Configuration	Predicted V_l [V]	Measured V_l [V]	Error [%]
1	–	–	–
2	0.79	0.75	5.44
3	1.33	1.28	4.09
4	2.61	2.55	2.13
5	2.91	2.86	1.85
6	3.73	3.62	3.20
7	–	–	–

Since electrical power is determined by the product of the current and voltage values, it is paramount that they are predictable and accurate compared to measured values. The results above show exactly that. The error is sufficiently low. However, configuration 1 and 7 are discarded as the results showed clearly that they are at the extremes of the linear model and thus inaccurate.

5.4.1.1 Electrical power

The measured electrical power is calculated from the evaluated data parameters, load voltage and induced current as shown in Table 5-7 and 5-8. Table 5-9 shows the usable power given the electrical model with percentage error. The three sets of data for usable power are graphed in Figure 5-12 for an illustrative comparison. The mechanical model under-predicts; however, the electrical model shows relatively accurate values as is evident from the percentage error shown in Table 5-9.

Table 5-9 Usable electrical power

Configuration	Usable electrical power P_u [W]	Measured P_u [W]	Error [%]
1	–	–	–
2	0.14	0.13	5.83
3	0.19	0.19	4.04
4	0.23	0.23	0.06
5	0.19	0.20	5.40
6	0.15	0.14	5.11
7	–	–	–

Above are the measured and predicted usable power values of the electrical model. Comparative results lead to the conclusion that the model and characterization of the parameters were sufficient. The electrical usable power is consecutively taken for comparison against the mechanical usable power and the measured usable power.

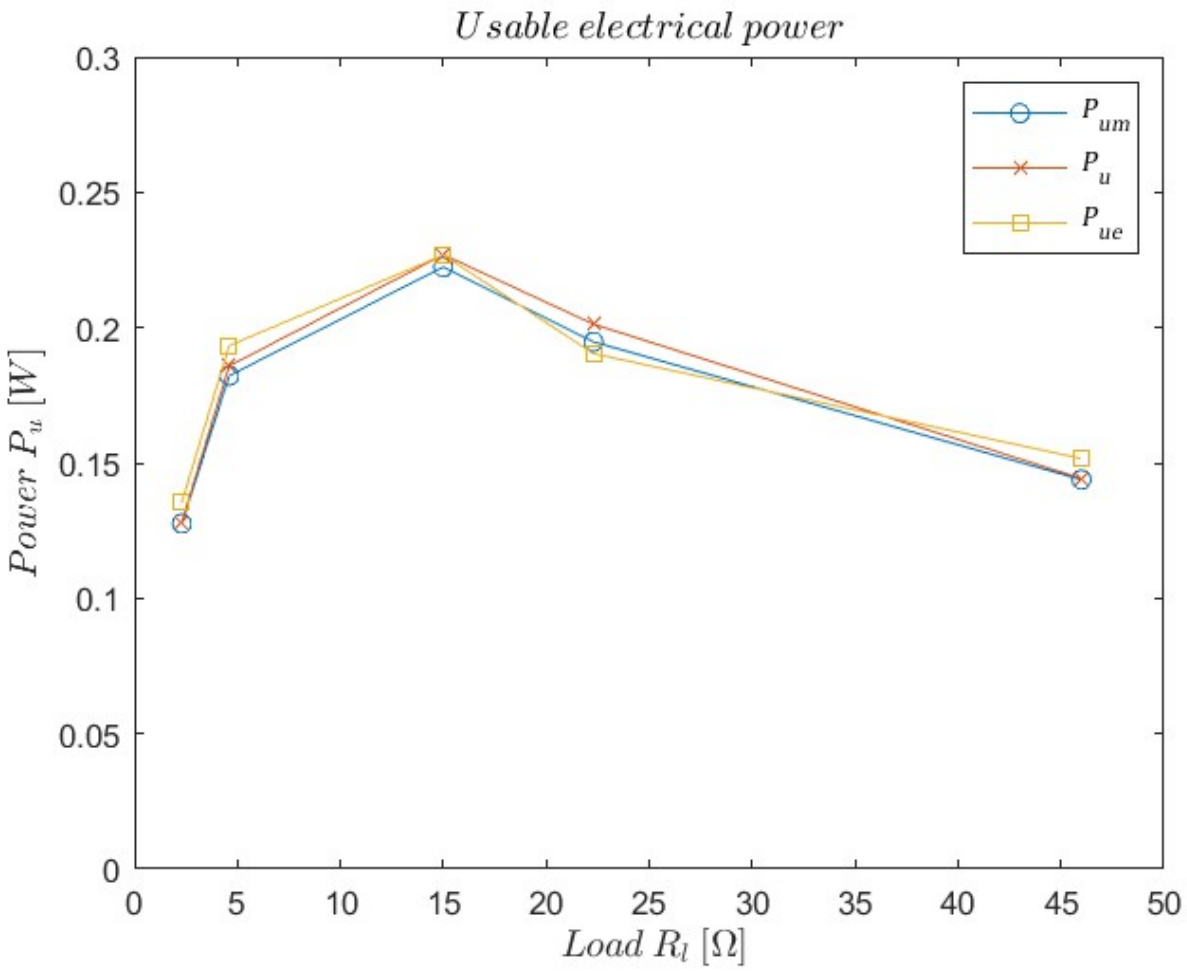

Figure 5-12 Usable power comparison

5.5 Conclusion

The mechanical and electrical models are evaluated to be accurate to within 10% error. The graph in Figure 5-12 is evidence of the validity of the models as the predicted values closely follow the measured values. The mechanical model is highly sensitive for errors in the value of damping. The assumption that induction is minimal is proven to be appropriate for this instance. The maximum usable power is seen at configuration 4, which was also used in this chapter for illustrative purposes. This does not correspond to impedance matching in the traditional sense of an electrical circuits, which would be $2\ \Omega$, but rather impendence matching in a model where the mechanical system is seen as an electrical equivalent. With the evaluation completed, the mechanical and electrical model both describe the behaviour of a vibration energy generator accurately and that valid prediction can be made with the model within limits of characterised input parameters.

Chapter 6 Conclusion

The investigation to understand the technical behaviour of a vibration energy generator, was successful and an adequate design for a vibration energy generator could be attained. The behaviour or performance of a vibration energy generator is ultimately seen in the usable power that is delivered. The parameters that affect this outcome have been identified and are presented in mathematical models that describe the behaviour of a vibration energy generator. The basic design requirement for a vibration energy generator is realised in a loudspeaker. Finally, it is determined that a loudspeaker can be utilised as a vibration energy generator with no further adjustments.

The process to determine whether a loudspeaker is adequate for use as a vibration energy generator was concurrently recorded in this dissertation to arrive at a design for a vibration energy generator. A literature study was completed, upon which mathematical models were developed for a mechanical and an electrical system that are constituents of a vibration energy generator system. Required parameters used in said mathematical models were characterised and used to predict the technical behaviour of a loudspeaker as a vibration energy generator. The predictions were evaluated experimentally to determine the validity of the mathematical models.

The mechanical and electrical systems that are modelled give insight to specific parameters. The parameters of concern were characterised. The parameters such as mechanical stiffness, damping and natural frequency were finally characterised *in situ*. The electrical parameters were obtained and determined through typical measurements. With these input parameters the predicted values were obtained and evaluated with experimental data.

Through experimental evaluation it was shown that the mathematical models are suited to predict the technical behaviour of a vibration energy generator. During experimentation the maximum usable power of $23\ mW$ was generated at configuration 4. This corresponds to an electrical load of $15\ \Omega$ and an operating frequency of $33\ Hz$.

To identify the specific operating configuration and frequency for the vibration energy generator requires excessive and delicate characterization of parameters unique to the loudspeaker. Therefore, the design of a vibration energy generator should rather be approached per application. Architecture and design concepts for an application can vary greatly. However, in general, the design will have the mechanical components of mass, stiffness and damping, while the electrical components present will be the transducer and electrical load, where upon the design for a vibration energy generator will be inclined to achieve maximum usable power.

To develop a design for maximum usable power, the excitation frequency and amplitude, mechanical dynamic properties, coupling factor and electrical load and the intricate relationships thereof need be

modelled and predicted. The maximum usable power configuration would then be obtained through operation at resonance and selecting an optimal load. This can be done after the design concept has been selected with regards to the transducer and mechanical architecture.

Achieving these goals in reality becomes more cumbersome for a few reasons. Firstly, a generator could be exposed to random or varying excitation. To operate at maximum power would require active or passive tuning for the change in frequencies or amplitude. This entails extensive study of the specific system characteristics under transient conditions.

Secondly, varying material or environmental properties affect dynamic characteristics. This has an influence on maximum power and should be addressed accordingly. The use of a mechanical architecture that is simple, with well-studied materials would allow these factors to be addressed more easily.

Thirdly, the exact electrical load and its varying characteristic is important as it influences the maximum power configuration as well. The electrical load should be optimised in accordance with the mechanical system to ensure operation at maximum usable power.

This ultimately leads to a system that is adjustable in all parameters concerned but yet with relatively predictable and consistent parameters. It is recommended that further research be conducted to utilise the basic design of a loudspeaker to develop an adjustable yet relatively predictable and consistent system. The use of a loudspeaker design is beneficial because the magnetic circuit and manufacturing processes have been optimised and are commercially utilised. The dynamic components should be replaced with more predictable and stable materials. A system that is easily adjustable and stable is viable as a generic solution for suitable applications. Further work will include study on the model's validity under random and transient excitation after proposed changes have been made to the system.

References

Anderson, B.E. & Leishman, T.W. 2003. An acoustical measurement method for the derivation of loudspeaker parameters. 115th Convention of the Audio Engineering Society: New York.

Arroyo, E. & Badel, A. 2011. Electromagnetic vibration energy harvesting device optimization by synchronous energy extraction. *Sensors and Actuators A: Physical*, 171(2):266-273. doi: 10.1016/j.sna.2011.06.024

Ashraf, K., Md Khir, M.H., Dennis, J.O. & Baharudin, Z. 2013. Improved energy harvesting from low frequency vibrations by resonance amplification at multiple frequencies. *Sensors and Actuators A: Physical*, 195:123-132. doi: 10.1016/j.sna.2013.03.026

Askeland, D.R. & Wright, W.J. 2016. *The science and engineering of materials.* 7th edition, SI. Cengage Learning.

ASTM-E1050 2019. Standard Test Method for Impedance and Absorption of Acoustical Materials Using a Tube, Two Microphones and a Digital Frequency Analysis System. https://www.document-center.com Date of access: 6 February

Audio Engineering Society, Inc. 1991. AES Information Document Plane-Wave Tubes: Design and Practice. *AES 1id-1991(r2003).*

Austrell, P.-E. & Olsson, A.K. 2012. Considering amplitude dependence during cyclic loading of elastomers using an equivalent viscoelastic approach. *Polymer Testing*, 31(7):909-915. doi: 10.1016/j.polymertesting.2012.05.005

Bandstra, J.P. 1981. Comparison of equivalent viscous damping and nonlinear damping in discrete and continuous vibrating systems. *Journal of Vibration and Acoustics,* 105(3):382-392. doi: 10.1115/1.3269117

Beeby, S., Torah, R., Tudor, M., Glynne-Jones, P., O'Donnell, T., Saha, C. & Roy, S. 2007. Micro electromagnetic generator for vibration energy harvesting. *Journal of Micromechanics and Microengineering* vol. 17. doi: 10.1088/0960-1317/17/7/007

Cammarano, A., Burrow, S.G., Barton, D.A.W., Carrella, A. & Clare, L.R. 2010. Tuning a resonant energy harvester using a generalized electrical load. *Smart Materials and Structures*, 19(5). doi: 10.1088/0964-1726/19/5/055003

Cao, X., Chiang, W., King, Y. & Lee, Y. 2007. Electromagnetic energy harvesting circuit with feedforward and feedback DC–DC PWM boost converter for vibration power generator system. *IEEE Transactions on Power Electronics*, 22(2):679-685. doi: 10.1109/TPEL.2006.890009

Cepnik, C., Lausecker, R. & Wallrabe, U. 2013. Review on electrodynamic energy harvesters—a classification approach. *Micromachines*, 4(2):168-196. 10.3390/mi4020168

Challa, V.R., Cheng, S. & Arnold, D.P. 2013. The role of coupling strength in the performance of electrodynamic vibrational energy harvesters. *Smart Materials and Structures*, 22(2). doi: 10.1088/0964-1726/22/2/025005

Dayal, R., Dwari, S. & Parsa, L. 2011. A new design for vibration-based electromagnetic energy harvesting systems using coil inductance of microgenerator. *IEEE Transactions on Industry Applications*, 47(2):820-830. doi: 10.1109/tia.2010.2101995

De Silva, C.W. 2000. *Vibration: fundamentals and practice*. CRC-Press.

Den Hartog, J.P. 1985. *Mechanical vibrations*. Dover Publications.

Dickason, V. 2007. *The loudspeaker design cookbook*. Audio Amateur Press.

Eargle, J.M. 2002. *Electroacoustical reference data.* Kluwer Academic Publishers.

Eclipsemagnetic. Ferrite (ceramic) magnets. https://www.eclipsemagnetics.com/products/magnetic-materials-and-assemblies/magnet-materials/ferrite-ceramic-magnet-material/ Date of access: 18 August.

Eclipsemagnetics. Alnico magnets. https://www.eclipsemagnetics.com/products/magnetic-materials-and-assemblies/magnet-materials/alnico-magnet-material/ Date of access: 18 August.

Eclipsemagnetics. Rare earth neodymium magnets (NdFeB). https://www.eclipsemagnetics.com/products/magnetic-materials-and-assemblies/magnet-materials/neodymium-magnet-material/ Date of access: 18 August.

Elvin, N.G. & Elvin, A.A. 2011. An experimentally validated electromagnetic energy harvester. *Journal of Sound and Vibration*, 330(10):2314-2324. doi: 10.1016/j.jsv.2010.11.024

First4magnets. Magnetic materials. https://www.first4magnets.com/magnetic-materials-i156 Date of access: 18 August.

French, A.P. 1971. *Vibrations and waves*. Taylor & Francis.

Hendijanizadeh, M., Sharkh, S.M., Elliott, S.J. & Moshrefi-Torbati, M. 2013. Output power and efficiency of electromagnetic energy harvesting systems with constrained range of motion. *Smart Materials and Structures*, 22(12). doi: 10.1088/0964-1726/22/12/125009

HSmagnets. Permanent magnets. https://www.hsmagnets.com/permanent-magnets/ Date of access: 18 August.

HSmagnets. Sintered neodymium magnets. https://www.hsmagnets.com/permanent-magnets/neodymium-magnets/ Date of access: 18 August.

HSmagnets. Ferrite magnets. https://www.hsmagnets.com/permanent-magnets/ferrite-magnets/ Date of access: 18 August.

HSmagnets. SmCo magnets. https://www.hsmagnets.com/permanent-magnets/samarium-cobalt-magnets/ Date of access: 18 August.

HSmagnets. Alnico magnets. https://www.hsmagnets.com/permanent-magnets/alnico-magnets/ Date of access: 18 August.

Inman, D.J. & Singh, R.C. 2014. *Engineering vibration*. Pearson.

IntegratedMagnetics. Magnet materials overview. https://www.intemag.com/magnet-materials Date of access: 18 August.

IRENA (International Renewable Energy Agency). 2019. Innovation landscape brief: utility-scale batteries. International Renewable Energy Agency, Abu Dhabi.

James, F. 1991. Time, tide and Michael Faraday. *History Today,* 41(9):28. (Accessed online via NWU Library Research Portal).

John, E. 2012. *Loudspeaker measurements and modeling*. 325 p. Boston, MA: Springer US.

Joyce, B.S., Farmer, J. & Inman, D.J. 2014. Electromagnetic energy harvester for monitoring wind turbine blades. *Wind Energy,* 17(6):869-876. doi: 10.1002/we.1602

Karwatka, D. 2011. Hans Christian Oersted discovers electromagnetis. *Tech Directions*, 71(4):12. (Accessed online via NWU Library Research Portal).

Kelly, S.G. 2012. *Mechanical vibrations: theory and applications*. Cengage Learning.

Ichikawa, K. & Hijikata, W. 2019. Development of intraoral electrostatic energy harvester driven by occlusal force. *The Proceedings of the Conference on Information, Intelligence and Precision Equipment (IIP)*:1. doi: 10.1109/EMBC.2019.8856933

Khan, F.U. & Izhar. 2016. Electromagnetic energy harvester for harvesting acoustic energy. *Sādhanā,* 41(4):397-405. doi: 10.1007/s12046-016-0476-9

Kinsler, L.E., Frey, A.R., Coppens, A.B. & Sanders, J.V. 1982. *Fundamentals of accoustics.* New York: John Wiley & Sons.

Klippel, W.J. 2018. Maximizing efficiency in active loudspeaker systems. *Journal of the Audio Engineering Society*, 2018.

Lin, T.R., Farag, N.H. & Pan, J. 2005. Evaluation of frequency dependent rubber mount stiffness and damping by impact test. *Applied Acoustics*, 66(7):829-844. doi: 10.1016/j.apacoust.2004.10.004

Liu, M., Tai, W.-C. & Zuo, L. 2021. Vibration energy-harvesting using inerter-based two-degrees-of-freedom system. *Mechanical Systems and Signal Processing*, 146. doi: 10.1016/j.ymssp.2020.107000

Magnetshop. Magnet materials. https://www.magnetshop.com/resources/magnet-materials.html Date of access: 18 August.

Marinescu, M., Marinescu, N. & Kuhn, S. 2016. Optimization of magnetic circuits for loudspeakers 1970 and now. 2016 International Symposium on Fundamentals of Electrical Engineering (ISFEE). pp. 1-10. doi: 10.1109/ISFEE.2016.7803149

Mitcheson, P.D., Green, T.C., Yeatman, E.M. & Holmes, A.S. 2004. Architectures for vibration-driven micropower generators. *Journal of Microelectromechanical Systems,* 13(3):429-440. doi: 10.1109/JMEMS.2004.830151

Mitcheson, P.D., Yeatman, E.M., Rao, G.K., Holmes, A.S. & Green, T.C. 2008. Energy harvesting from human and machine motion for wireless electronic devices. *Proceedings of the IEEE,* 96(9):1457-1486. doi: 10.1109/jproc.2008.927494

Mitolo, M. & Araneo, R. 2019. A brief history of electromagnetism. *IEEE Industry Applications Magazine*, 25(2):7-11. doi: 10.1109/mias.2018.2884753

Moreno, J.N. 1991. Measurement of loudspeaker parameters using a laser velocity transducer and two-channel FFT analysis. *Journal of the Audio Engineering Society*, 39(4):243-249. (Accessed online via NWU Library portal).

Naifar, S., Bradai, S., Viehweger, C. & Kanoun, O. 2017. Survey of electromagnetic and magnetoelectric vibration energy harvesters for low frequency excitation. *Measurement*, 106:251-263. doi: 10.1016/j.measurement.2016.07.074

Nel, C.B. & Wyngaardt, J. 2014. *Dynamic vibration absorber design for a motor and pump assembly.* 487 p. Cham: Springer International Publishing.

Nel, C.B. & van Wyngaardt, J. 2014. Amplitude dependency on dynamic properties of a rubber mount. *In*: Allen, M., Mayes, R. & Rixen, D., eds. *Dynamics of coupled structures*, Volume 1, Cham. Springer International Publishing. pp. 447-454.

Nilsson, J.W. & Riedel, S.A. 2020. *Electric circuits.* 11th ed. Pearson Education Limited.

Poulin, G., Sarraute, E. & Costa, F. 2004. Generation of electrical energy for portable devices. *Sensors and Actuators A: Physical*, 116(3):461-471. doi: 10.1016/j.sna.2004.05.013

Rahman, M.F.B.A. & Kok, S.L. 2011. Investigation of useful ambient vibration sources for the application of energy harvesting. *In:* 2011 IEEE Student Conference on Research and Development. pp. 391-396.

Rao, S.S. 2011. *Mechanical vibrations*. 5th ed. Prentice Hall.

Roundy, S. 2005. On the effectiveness of vibration-based energy harvesting. *Journal of Intelligent Material Systems and Structures*, 16:809-823. doi: 10.1177/1045389X05054042

Ruby, L. 2000 Equivalent Mass of a Coil Spring. *Physics Teacher*, 38(3):140-141.

Salim, M., Dayou, J., Aljibori, H.S., Salim, D. & Shebeeb, A. 2016. A low frequency hybrid harvester with ring magnets. *Sustainable Energy Technologies and Assessments*, 13:23-30. doi: 10.1016/j.seta.2015.11.006

Schmitz, T.L. & Smith, K.S. 2012. *Mechanical vibrations: modeling and measurement*. Springer.

Shahhaidar, E., Padasdao, B., Boric Lubecke, O., Romine, R. & Stickley, C. 2015. Electromagnetic respiratory effort harvester: Human testing and metabolic cost analysis. *IEEE Journal of Biomedical and Health Informatics,* 19(2):399-405-405. doi: 10.1109/JBHI.2014.2326597

Singh, K.B., Taheri, S., Bedekar, V. & Priya, S. 2012. Piezoelectric vibration energy harvesting system with an adaptive frequency tuning mechanism for intelligent tires. *Mechatronics*, 22(7):970-988-988. doi: 10.1016/j.mechatronics.2012.06.006

Smith, W.F., Hashemi, J. & Wang, S.-H. 2011. *Foundations of materials science and engineering.* 5th SI ed. McGraw-Hill.

Spreemann, D., Folkmer, B. & Manoli, Y. 2008. Comparative study of electromagnetic coupling architectures for vibration energy harvesting devices. *Proceedings of PowerMems 2008 and MicroEMS*, pp. 257-260.

Standordmagnets. Ferrite/Ceramic Magnets. https://www.stanfordmagnets.com/ceramic-ferrite-magnets.html Date of access: 18 August.

Stanfordmagnets. ALNICO magnets. https://www.stanfordmagnets.com/alnico-magnets.html Date of access: 18 August.

Stanfordmagnets. Neodymium magnets. https://www.stanfordmagnets.com/neodymium-magnets.html Date of access: 18 August.

Stephen, N.G. 2006. On energy harvesting from ambient vibration. *Journal of Sound and Vibration,* 293(1):409-425. https://www.sciencedirect.com/science/article/pii/S0022460X05006784 doi: 10.1016/j.jsv.2005.10.003

Tang, X. & Zuo, L. 2011. Enhanced vibration energy harvesting using dual-mass systems. *Journal of Sound and Vibration*, 330(21):5199-5209. doi: 10.1016/j.jsv.2011.05.019

Tsai, Y.T., Wang, C.C. & Huang, J.H. 2013. An inverse method for estimating the electromechanical parameters of moving-coil loudspeakers. *Journal of the Acoustical Society of America*, 134(5):3594-3604. https://www.ncbi.nlm.nih.gov/pubmed/24180770 doi: 10.1121/1.4824158

Van Niekerk, J.L., Heyns, P.S. & Heyns, M. 2000. Human vibration levels in the South African mining industry. *The Journal of The South African Institute of Mining and Metallurgy*,100:235-242. http://saimm.org.za/Journal/v100n04p235.pdf

Verma, S.P. & Li, W. 2003. Measurement of vibrations and radiated acoustic noise of electrical machines. 2:861. Sixth International Conference on Electrical Machines and Systems, 2003. ICEMS 2003. Beijing, China.

Von Büren, T. & Tröster, G. 2007. Design and optimization of a linear vibration-driven electromagnetic micro-power generator. *Sensors and Actuators A: Physical*, 135(2):765-775. doi: 10.1016/j.sna.2006.08.009

Walker, J., Resnick, R. & Halliday, D. 2014. *Halliday & Resnick fundamentals of physics.* 10th ed. Wiley.

Wang, X., Liang, X., Shu, G. & Watkins, S. 2016. Coupling analysis of linear vibration energy harvesting systems. *Mechanical Systems and Signal Processing*, 70-71:428-444. doi: 10.1016/j.ymssp.2015.09.006

Wang, X., John, S., Watkins, S., Yu, X., Xiao, H., Liang, X. & Wei, H. 2015. Similarity and duality of electromagnetic and piezoelectric vibration energy harvesters. *Mechanical Systems and Signal Processing*, 52-53:672-684. doi: 10.1016/j.ymssp.2014.07.007

Wei, C. & Jing, X. 2017. A comprehensive review on vibration energy harvesting: modelling and realization. *Renewable and Sustainable Energy Reviews,* 74:1-18. doi: 10.1016/j.rser.2017.01.073

Xuezheng, J., Yancheng, L. & Jianchun, L. 2013. Design of a novel linear permanent magnet vibration energy harvester. Paper presented at the 2013 IEEE/ASME International Conference on Advanced Intelligent Mechatronics.

Yildirim, T., Ghayesh, M.H., Li, W. & Alici, G. 2017. A review on performance enhancement techniques for ambient vibration energy harvesters. *Renewable and Sustainable Energy Reviews,* 71:435-449. doi: 10.1016/j.rser.2016.12.073

Yu, Z., Saechan, P. & Jaworski, A.J. 2011. A method of characterising performance of audio loudspeakers for linear alternator applications in low-cost thermoacoustic electricity generators. *Applied Acoustics*, 72(5):260-267. doi: 10.1016/j.apacoust.2010.11.011

Zhang, Q. & Kim, E.S. 2014. Vibration energy harvesting based on magnet and coil arrays for watt-level handheld power source. *Proceedings of the IEEE*, 102(11):1747-1761. doi: 10.1109/jproc.2014.2358995

Zhang, Q., Wang, Y. & Kim, E.S. 2015. Electromagnetic energy harvester with flexible coils and magnetic spring for 1–10 Hz resonance. *Journal of Microelectromechanical Systems*, 24(4):1193-1206. doi: 10.1109/jmems.2015.2393911

Appendix A MATLAB code

Mechanical model

```
load('step_5\step_5_data.mat')
load('Meas_eval/meas_eval_table',"meas_eval_t")

f_o=[39.25 ;34.625 ;33.75; 32.5 ;32 ;31.63; 31.125];
R_l= [0.1 ;2.3 ;4.6 ;15 ;22.3 ;46 ;100];
comp_table=table();
comp_table2=table();
%1DOf model base excitation
%--------Import Input variables--------
global k_g m_g omega c_g X_b_in

for i=1:7
Config=i;
str=['Config',num2str(Config)];
var=CharPar.(str);

m_g=var(1,1);
k_g=var(2,1);
Zeta=var(3,1);
f_n=var(4,1);
omega_n=f_n*2*pi;
c_c=2*m_g*omega_n;
c_g=Zeta*c_c/100;
X_b_in=meas_eval_t.X_b(i);

f=f_o(Config,1);
omega=2*pi*f;

%--------Run ode45.m-----------
stp=0.0001;
tspan = 0:stp:20;

u0 = [0 0];
[t,u] = ode45(@(t,u) my1dof(t,u), tspan, u0);

x_ge=u(:,1);
xd_ge=u(:,2);
xdd_ge=(-k_g*u(1)-c_g*u(2)+X_b_in*k_g*sin(omega*t)+...
    X_b_in*c_g*omega*cos(omega*t))/m_g;
[pksxg,pklocg]=findpeaks(x_ge);
X_ge=pksxg(end);

x_b=X_b_in*sin(omega*t);
xd_b=X_b_in*omega*cos(omega*t);
[pksxb,pklocb]=findpeaks(x_b);
X_b=pksxb(end);

Phase_mec=abs(mean(360*f*(-pklocb(end-50-1:end-1)...
    .*stp+pklocg(end-50-1:end-1).*stp)-180));
Phase_mec2=abs(Phase_mec-180);

myarad=(Phase_mec2/360)*(2*pi);
X_rel=max(X_ge*sin(omega*t)-X_b_in*sin(omega*t+myarad));
```

```
Zeta_m=399.7*X_rel+5.525;
xrel=(x_ge-x_b);


F_k= k_g*X_ge;
F_c=c_g*X_ge*omega;
F_m=m_g*X_ge*omega^2;
F_kb=k_g*X_b_in;
F_cb=c_g*X_b_in*omega;
F_t=sqrt(F_kb^2+F_cb^2);

%power in each component
pk=(k_g*X_rel*omega*X_rel*sin(omega*t))/2;
pc=(c_g*omega*X_rel*omega*X_rel*cos(omega*t)+c_g*omega*X_rel*omega*X_rel)/2;
pm=(m_g*X_rel*omega^2*omega*X_rel*sin(omega*t-pi))/2;

amppk=max(pk);
amppc=max(pc);
amppm=max(pm);
pkb=F_kb*X_rel*omega;
pcb=F_cb*X_rel*omega;
ppt=F_t*omega*X_rel;
alpha=((atand(pcb/pkb)+Phase_mec2)/360)*(2*pi);

pin=(m_g*omega^2*X_b_in*omega*X_rel*sin(omega*t+alpha)...
    +m_g*omega^2*X_b_in*omega*X_rel)/2;
p_avg2=c_g*omega^2*X_rel^2/2;
p_avg=(c_g*m_g^2*omega^6*X_b_in^2)/(2*((k_g-omega^2*m_g)^2+(c_g*omega)^2));
p_e_um=p_avg*((Zeta-Zeta_m)/Zeta)*(R_l(i)/(R_l(i)+1.9));

var_n=[X_ge X_b Phase_mec2 X_rel F_m F_k F_c F_kb F_cb amppm amppk amppc p_avg p_e_um];
str=['Config',num2str(Config)];
predmdata.(str)=var_n;
save('Pred/Pred_m_data.mat','predmdata')


mytable=table(Config,
X_ge,Phase_mec2 ,X_rel ,F_m ,F_k ,F_c ,F_kb ,F_cb ,amppm ,amppk ,amppc ,p_avg,
p_avg2 ,p_e_um);
comp_table =[comp_table;mytable];

mytable2=table(m_g,k_g,Zeta,f_n,f,X_b)
comp_table2=[comp_table2;mytable2;]
end

save('Pred/Pred_t',"comp_table")
writetable(comp_table,'data.xls','Sheet','Pred_m','Range','B2')
writetable(comp_table2,'data.xls','Sheet','Pred_m','Range','B12')

function dudt= my1dof(t,u)
global k_g m_g omega c_g X_b_in

dudt = zeros(2,1);
dudt(1)= u(2);
dudt(2) = (-k_g*u(1)-c_g*u(2)+X_b_in*k_g*sin(omega*t)...
    + X_b_in*c_g*omega*cos(omega*t))/m_g;
end
```

Electrical model

```
%input parameters
BL= 8.3;

%load relative response
load Meas_eval\meas_data.mat
comp=table()
for i=1:7
Config=i;
str=['Config',num2str(Config)];
var=measdata.(str);
arad=((var(1,3)/360)*(2*pi));
omega= var(1,5)*2*pi;
stp=0.0001;
t = 0:stp:20;
Xd_rel=max(var(1,1)*sin(omega*t)-var(1,2)*sin(omega*t+arad))*omega;


Z_tot= var(1,6)+1.9;
VV=8.3*Xd_rel;
II=VV/Z_tot;
V_l=II*var(1,6);

p_elec_e=VV*II/2;
p_u = V_l*II/2;
var_n=[Xd_rel V_l II p_elec_e p_u]
str=['Config',num2str(Config)]
prededata.(str)=var_n
save('Pred/Pred_e_data.mat','prededata')

mytable=table(Xd_rel,Z_tot,BL,VV,II,V_l,p_u)
comp=[comp;mytable]


end
writetable(comp,'data.xls','Sheet','Pred_e','Range','B2')
```

Mechanical characterization *in situ*

```
%step_5
clc
clear all
load step_5\meas_data.mat
load step_5\step_5_data.mat

comp_table=table();
for i=1:7
config=i
str=['Config',num2str(config)]
var=measdata.(str)
f=var(1,1)
G_X=var(2,1)
G_y=var(3,1)
p=abs(var(4,1)-var(5,1)-180)
omega = f*2*pi;%2*pi*fre;
X = G_X*9.81/(omega^2);%AmplRo1;
Y = G_y*9.81/(omega^2);%AmplRt1;
m=0.1779;
phi = (p/360)*(2*pi);%phasedifrad1;

syms k c;
%Solve equations simulataneously
eq1 = (X./Y)==sqrt((k.^2+(c*omega).^2)/((k-m.*omega.^2).^2+(c.*omega).^2));
eq2 = tan(phi)==(m.*c.*omega.^3.)/((k.*(k-m.*omega.^2)+(omega.*c).^2));
[c,k] = solve(eq1,eq2);
k_g = max(double(k));
c_g = max(double(c));

Cc = 2*sqrt(k_g*m);
psi = (c_g/Cc)*100
XY = X/Y;
f_n=(sqrt(k_g/m))/(2*pi)
grade = phi*((180)/pi*2)

X_rel=(m*Y*omega^2)/sqrt((k_g-m.*omega.^2).^2+(c_g.*omega).^2)
var_n=[m;k_g;psi;f_n;X;Y;p;X_rel]
CharPar.(str)=var_n
save('step_5\step_5_data.mat', 'CharPar')


mytable=table(config,f,X,Y,p,m,k_g,psi,f_n,X_rel)
comp_table=[comp_table;mytable]

end
save('step_5/step_5_t',"comp_table")
writetable(comp_table,'data.xls','Sheet','step_5','Range','B2')
```

Bump test

```
%analysing bump test data for the speaker
clc
clear all

comp_out=table();
%import data and plot only data
for n=7
    if n<10
         lstring=['0',num2str(n)];

    else
      lstring=[num2str(n)];


    end

load(['step_3\',lstring, '.mat'])

g=3;
u=g+5;
j=25 ;

    if n<10
         string={['0',num2str(n),'.tra']};
         string1={['0',num2str(n),'.trb']};
    else
      string={[num2str(n),'.tra']};
      string1={[num2str(n),'.trb']};

    end
str=char(string);
str1=char(string1);
[e01,e00] = importDIdata(str,[1,inf]);
[e02,e03]= importDIdata(str1,[1,inf]);

%clearing noise in frequency domain

deltaf=e03(2)-e03(1);

    if deltaf == 2.5
        e02(1:5)=0;

    elseif deltaf == 2
        e02(1:1)=0;

    elseif deltaf == 1.25
        e02(1:5)=0;

    elseif deltaf == 1
        e02(1:4)=0;

    elseif deltaf == 0.5
            e02(1:5)=0;

    elseif deltaf == 0.25
            e02(1:8)=0;
```

```
    elseif deltaf == 0.125
            e02(1:15)=0;
    end

%Correcting for G's
e11=9.81.*e01;

%Find and plot peaks
[pks,loc] = findpeaks(e11,'MinPeakDistance',j);
[pksBG,locBG] = findpeaks(-e11,'MinPeakDistance',j);

figure(1);
subplot(2,1,1);
p1=plot(e00,e11,e00(locBG(g:u)),e11(locBG(g:u)),'o',e00(loc(g:u)),e11(loc(g:u)),'o');
hold on
ylim([-max(e11)*1.2 max(e11)*1.2])
xlabel('$$Time \:t\:[s]$$','fontsize',12,'interpreter','latex');
ylabel('$$Response\:ddot{x}_g\:[m/s^2]$$','fontsize',12,'interpreter','latex');
% title(['Response to impact, SN',num2str(n)]);
set(gcf,'color','w')
hold off;

subplot(2,1,2);
p1=plot(e03,e02);
hold on
ylim([0 max(e02)*1.1]);
xlabel('frequency \itt\rm [Hz]');
ylabel('Response\fontname{Cambria Math}\it ddot{x}_g \rm [m/s^2]');
title(['Response to impact load, SN',num2str(n)]);
hold off

saveas(figure(1),['step_3/Resp SN',num2str(n),'.jpg'])


for q=g:u
%running analysis
x_ddot_1(q) =pks(q);
x_ddot_2(q) =pks(q+1);

t1(q)=e00(loc(q));
t2(q)=e00(loc(q+1));

m(q)=0.1779;

syms Zeta omega_n

tau_d=t2(q)-t1(q);
omega_d=(1/tau_d*2*pi);

eqn1=(x_ddot_1(q)/x_ddot_2(q))==exp(Zeta*omega_n*tau_d);
eqn2= omega_n== (omega_d)/sqrt(1-Zeta^2);

eqns = [eqn1 eqn2];
S = solve(eqns,[Zeta omega_n]);

myZeta(q) = double(S.Zeta).*100;
```

```
myOmega_n(q)= double(S.omega_n);
mynatfreq(q)= myOmega_n(q)/(2*pi);
X_avg(q)=(x_ddot_1(q)+x_ddot_2(q))/(2*(myOmega_n(q)^2));
myke(q)=((myOmega_n(q))^2)*m(q);
end


for h=g:u
%running analysis
x_ddot_1_BG(h) =pksBG(h);
x_ddot_2_BG(h) =pksBG(h+1);

t1_BG(h)=e00(locBG(h));
t2_BG(h)=e00(locBG(h+1));

m_BG(h)=0.1779;

syms Zeta omega_n

tau_d=t2_BG(h)-t1_BG(h);
omega_d=(1/tau_d*2*pi);

eqn1=(x_ddot_1_BG(h)/x_ddot_2_BG(h))==exp(Zeta*omega_n*tau_d);
eqn2= omega_n== (omega_d)/sqrt(1-Zeta^2);

eqns = [eqn1 eqn2];
S = solve(eqns,[Zeta omega_n]);


myZetaBG(h) = double(S.Zeta).*100;
myOmega_nBG(h)= double(S.omega_n);
mynatfreqBG(h)= myOmega_nBG(h)/(2*pi);
X_avgBG(h)=(x_ddot_1_BG(h)+x_ddot_2_BG(h))/(2*(myOmega_nBG(h)^2));
mykeBG(h)=((myOmega_nBG(h))^2)*m_BG(h);
end
```

Base Response

```
%step_base
%Base response calculated 1DOF

%typical operating frequency
f_r=[39.25;  34.625;      33.75; 32.5;  32     ;31.63;      31.125];
comp_out=table();
for h=1:7
f(h)=f_r(h);

global F_0 k_b m_b omega c_b
%Input variables
UB =100;
F_0=0.2026423673*((f(h)*2*pi)^2)*2*0.1*UB/100;
m_b=94.05;
omega=f(h)*2*pi;
k_b =54923;
f_n=(sqrt(k_b/m_b))/(2*pi);
omega_n_b=sqrt(k_b/m_b);
zeta_b=4/100;
c_b =zeta_b*2*sqrt(m_b*k_b);

%------------------------1 DOF RUngaKutta for Base-----------------------
stp=0.0001;
tspan = 0:stp:20;

u0 = [0 0];
[t,u] = ode45(@(t,u) mydof(t,u), tspan, u0);

%retrieving solution
x_b=u(:,1);
xd_b=u(:,2);
[pksx,pkloc]=findpeaks(x_b);
X_b(h)=pksx(end)
[pksbs,pklocsbd]=findpeaks(xd_b);
Xd_b(h)=pksbs(end)

myt=table(f(h),X_b(h),'VariableNames',{'f','X_b'})
comp_out=[comp_out;myt]
end

writetable(comp_out,'data.xls','Sheet','Pred_base','Range','B2')
save('step_base/comp_out.mat')

function dudt= mydof(t,u)
global F_0 k_b m_b omega c_b

dudt = zeros(2,1);
dudt(1)= u(2);
dudt(2) = (-k_b*u(1)-c_b*u(2)+F_0*sin(omega*t))/m_b;
end
```

Appendix B Vibration transducers

Model Number	ICP® ACCELEROMETER	Revision: H
352C33		ECN #: 28610

Performance	ENGLISH	SI	
Sensitivity(± 10 %)	100 mV/g	10.2 mV/(m/s²)	
Measurement Range	± 50 g pk	± 490 m/s² pk	
Frequency Range(± 5 %)	0.5 to 10,000 Hz	0.5 to 10,000 Hz	
Frequency Range(± 10 %)	0.3 to 15,000 Hz	0.3 to 15,000 Hz	
Resonant Frequency	≥ 50 kHz	≥ 50 kHz	
Broadband Resolution(1 to 10,000 Hz)	0.00015 g rms	0.0015 m/s² rms	[1]
Non-Linearity	≤ 1 %	≤ 1 %	[4]
Transverse Sensitivity	≤ 5 %	≤ 5 %	[5]
Environmental			
Overload Limit(Shock)	± 5000 g pk	± 49,000 m/s² pk	
Temperature Range(Operating)	-65 to +200 °F	-54 to +93 °C	[3]
Temperature Response	See Graph	See Graph	[3][1]
Base Strain Sensitivity	0.003 g/με	0.029 (m/s²)/με	[1]
Electrical			
Excitation Voltage	18 to 30 VDC	18 to 30 VDC	
Constant Current Excitation	2 to 20 mA	2 to 20 mA	
Output Impedance	≤ 200 ohm	≤ 200 ohm	
Output Bias Voltage	7 to 12 VDC	7 to 12 VDC	
Discharge Time Constant	1.0 to 2.5 sec	1.0 to 2.5 sec	
Settling Time(within 10% of bias)	<10 sec	<10 sec	
Spectral Noise(1 Hz)	39 μg/√Hz	380 (μm/s²)/√Hz	[1]
Spectral Noise(10 Hz)	11 μg/√Hz	110 (μm/s²)/√Hz	[1]
Spectral Noise(100 Hz)	3.4 μg/√Hz	33 (μm/s²)/√Hz	[1]
Spectral Noise(1 kHz)	1.4 μg/√Hz	14 (μm/s²)/√Hz	[1]
Physical			
Sensing Element	Ceramic	Ceramic	
Sensing Geometry	Shear	Shear	
Housing Material	Titanium	Titanium	
Sealing	Hermetic	Hermetic	
Size (Hex x Height)	0.44 in x 0.62 in	11.2 mm x 15.7 mm	
Weight	0.20 oz	5.8 gm	[1]
Electrical Connector	10-32 Coaxial Jack	10-32 Coaxial Jack	
Electrical Connection Position	Side	Side	
Mounting Thread	10-32 Female	10-32 Female	
Mounting Torque	10 to 20 in-lb	113 to 226 N-cm	

CE [6]

Typical Sensitivity Deviation vs Temperature

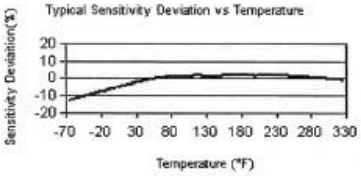

All specifications are at room temperature unless otherwise specified.
In the interest of constant product improvement, we reserve the right to change specifications without notice.

ICP® is a registered trademark of PCB Group, Inc.

OPTIONAL VERSIONS

Optional versions have identical specifications and accessories as listed for the standard model except where noted below. More than one option may be used.

HT - High temperature, extends normal operation temperatures			[3]
Frequency Range(5 %)	6 to 10,000 Hz	6 to 10,000 Hz	
Frequency Range(10 %)	4.5 to 15,000 Hz	4.5 to 15,000 Hz	
Broadband Resolution(1 to 10,000 Hz)	0.0009 g rms	0.009 m/s² rms	
Temperature Range(Operating)	-65 to +325 °F	-54 to +163 °C	
Excitation Voltage	22 to 30 VDC	22 to 30 VDC	
Discharge Time Constant	0.07 to 0.15 sec	0.07 to 0.15 sec	
Spectral Noise(1 Hz)	107 μg/√Hz	1050 (μm/s²)/√Hz	
Spectral Noise(10 Hz)	58 μg/√Hz	570 (μm/s²)/√Hz	
Spectral Noise(100 Hz)	41 μg/√Hz	400 (μm/s²)/√Hz	
Spectral Noise(1 kHz)	9.8 μg/√Hz	96 (μm/s²)/√Hz	
Output Bias Voltage	10 to 15 VDC	10 to 15 VDC	[2]

Supplied Accessory : Model ACS-68 Single Axis Amplitude Response Calibration from 5 Hz to upper 5% plotted on dB scale replaces Model ACS-1

J - Ground Isolated		
Frequency Range(5 %)	9 kHz	9 kHz
Frequency Range(10 %)	14 kHz	14 kHz
Resonant Frequency	≥ 40 kHz	≥ 40 kHz
Electrical Isolation(Base)	$>10^8$ ohm	$>10^8$ ohm
Size - Hex x Height	0.44 in x 0.67 in	11.2 mm x 17.0 mm
Weight	0.21 oz	6.0 gm

T - TEDS Capable of Digital Memory and Communication Compliant with IEEE P1451.4
TLA - TEDS LMS International - Free Format
TLB - TEDS LMS International - Automotive Format
TLC - TEDS LMS International - Aeronautical Format
TLD - TEDS Capable of Digital Memory and Communication Compliant with IEEE 1451.4

Temperature Range(Memory Access)	-10 to +200 °F	-23 to +93 °C
Excitation Voltage	20 to 30 VDC	20 to 30 VDC
Output Bias Voltage	7.5 to 13 VDC	7.5 to 13 VDC

W - Water Resistant Cable		
Electrical Connector	Sealed Integral Cable	Sealed Integral Cable
Electrical Connection Position	Side	Side

NOTES:
[1] Typical.
[2] TEDS option adds 1.0 VDC to bias voltage.
[3] 200°F to 325°F data valid with HT option only.
[4] Zero-based, least-squares, straight line method.
[5] Transverse sensitivity is typically ≤ 3%.
[6] See PCB Declaration of Conformance PS023 for details.

SUPPLIED ACCESSORIES:
Model 080A Adhesive Mounting Base (1)
Model 080A109 Petro Wax (1)
Model 081B05 Mounting Stud (10-32 to 10-32) (1)
Model ACS-1 NIST traceable frequency response (10 Hz to upper 5% point). (1)
Model M081B05 Mounting Stud 10-32 to M6 X 0.75 (1)

Entered: PCS	Engineer: BM	Sales: WDC	Approved: EIC	Spec Number:
Date: 4.15.08	Date: 4.15.08	Date: 4.15.08	Date: 4.15.08	13118

PCB PIEZOTRONICS
VIBRATION DIVISION
3425 Walden Avenue, Depew, NY 14043
Phone: 716-684-0001
Fax: 716-685-3886
E-Mail: vibration@pcb.com

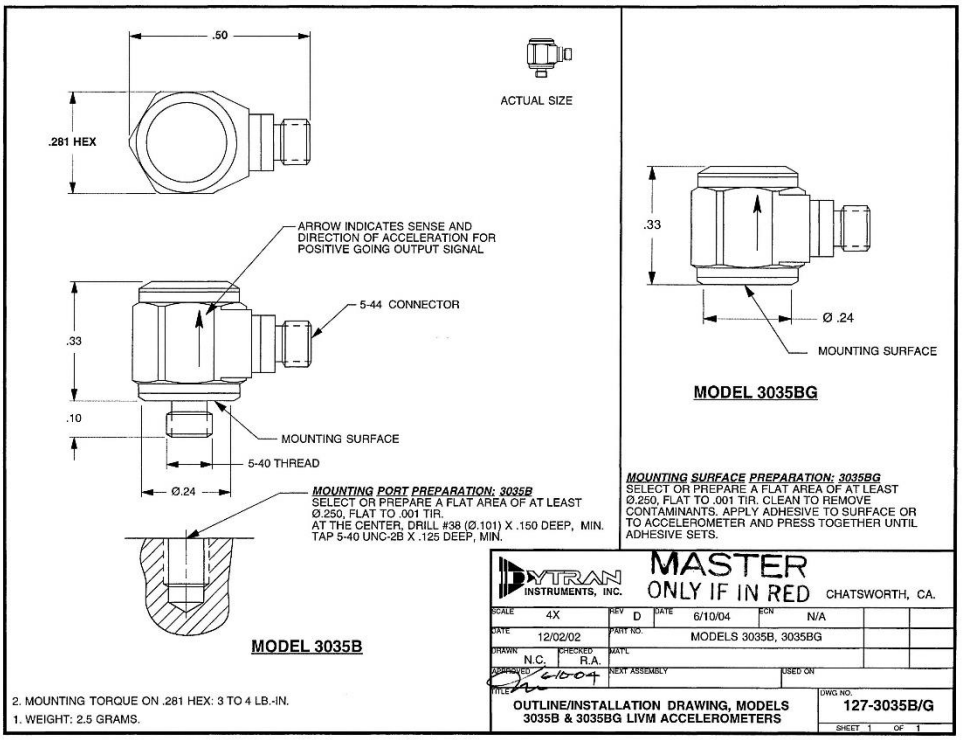

Model Number 3035B	PERFORMANCE SPECIFICATIONS	DOC NO PS3035B
	IEPE ACCELEROMETER	REV D, ECN 16235, 06/22/21

- MINATURE SIZE
- HERMETICALLY SEALED
- STUD MOUNT

	ENGLISH		SI	
PHYSICAL				
Weight, Max.	0.09	oz	2.5	grams
Connector	5-44 Coaxial		5-44 Coaxial	
Mounting Provision	5-40 Integral Stud		5-40 Integral Stud	
Material, Housing/Connector	300 Series Stainless Steel		300 Series Stainless Steel	
Sensing Element	Ceramic		Ceramic	
Element Style	Shear		Shear	
PERFORMANCE				
Sensitivity, ±10% [2]	100	mV/g	10.2	mV/m/s²
Range for ± 5 Volts Output	±50	g pk	±490.5	m/s² pk
Frequency Response, ±10%	0.34 to 10000	Hz	0.34 to 10000	Hz
Resonant Frequency	> 45	kHz	> 45	kHz
Broad Band Resolution	0.0004	g RMS	0.004	m/s² RMS
Linearity [3]	±1	% F.S.	±1	% F.S.
Maximum Transverse sensitivity	5	%	5	%
Strain Sensitivity @ 250με	0.002	g/με	0.02	m/s²/με
ENVIRONMENTAL				
Maximum Shock	10000	g pk	98067	m/s² pk
Temperature Range	-60 to +250	°F	-51 to +121	°C
Seal	Hermetic		Hermetic	
ELECTRICAL				
Supply Current Range [4]	2 to 20	mA	2 to 20	mA
Compliance Voltage Range	18 to 30	Volts	18 to 30	Volts
Output Impedance,Typ	100	Ω	100	Ω
Bias Voltage	11 to 13	VDC	11 to 13	VDC
Discharge Time Constant	0.8 to 2	Sec	0.8 to 2	Sec
Electrical Isolation	Case Grounded	GΩ,min	Case Grounded	GΩ,min

This family also includes:

Model	Range F.S. (g pk)	Sensitivity (mV/g)	Time Constant (Sec)
3035B1	± 500	10	0.8 to 2
3035B2	± 100	50	0.8 to 2
3035B3	± 1000	5	0.8 to 2

Refer to the performance specifications of the products in this family for detailed description

Supplied Accessories:

1) Accredited calibration certificate (ISO 17025)

Notes:

[1] All specifications are at room temperature unless otherwise specified.

[2] Measured at 100Hz, 1 g RMS per ISA RP 37.2.

[3] Measure using zero-based straight line method, % of F.S. or any lesser range

[4] Do not apply power to this system without current limiting. 20 mA MAX. To do so will destroy the IC charge amplifier.

[5] In the interest of constant product improvement, we reserve the right to change specifications without notice. It is the customer's responsibility to validate that a particular product with the properties described in the product specification is suitable for use in a particular application. Parameters provided in datasheets and / or specifications may vary in different applications and performance may vary over time. All operating parameters, including typical parameters, must be validated for each customer application by the customer's technical experts.

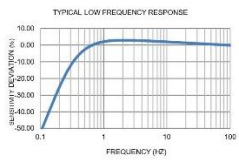

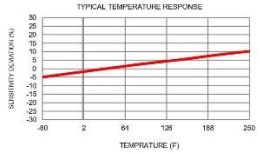

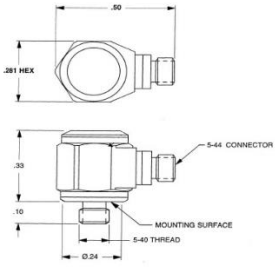

Units on the line drawing are in inches, units in brackets are in millimeters. Refer to 127-3035B/G for more information.

21592 Marilla Street, Chatsworth, California 91311 Phone: 818.700.7818 Fax:818.698.0362 www.dytran.com

Appendix C TS W311 4D Pioneer

Model Modell Modèle Modello Modelo Modelo Модель 機種 الموديل	Size Größe Taille Dimensioni Tamaño Tamanho Размер 尺寸 المقاس	Nominal power Nennleistung Puissance nominale Potenza norminal Potencia nominal Potência nominal Номинальное питание 額定功率 القدرة الإسمية	Max.music power Max.Musikleistung Puissance musicale maximum Potenza musicate massima Máxima potencia de musica Potência máxima da música Макс. музыкальная мощность 最大音樂功率 أقصى قدرة للموسيقى	Nominal impedance Nennimpedanz Impédance nominale Impedenza norminale Impedancia nominal Impedância nominal Номинальный импеданс 標稱阻抗 المقاومة الإسمية	Sensitivity Empfindlichkeit Sensibilité Sensibilità Sensibildad Sensibilidade Чувствительность 靈敏度 الحساسية	Frequency response Frequenzgang Bande passante Risposta alla frequenza Respuesta de frecuencia Resposta de freqüência Частотная характеристика 頻率响應 إستجابة الذبذبات	Magnet weight Magnetgewicht Poids aimant Peso del magnete Peso del imán Peso do magneto Вес магнита 磁鉄重量 وزن المغنطيس	Displacement Wegamplitude Déplacement Spostamento Desplazamiento Deslocamento Смещение 體積 الإزاحة
TS-W311S4	30 cm	400 W	1 400 W	4 Ω	95 dB ±1.5 dB (in car, input : 1 W)	20 Hz To 125 Hz (−20 dB in car, input : 1 W)	2 100 g	1.67 liters
TS-W311D4	30 cm	400 W	1 400 W	dual 4 Ω	95 dB ±1.5 dB (in car, input : 1 W)	20 Hz To 125 Hz (−20 dB in car, input : 1 W)	2 100 g	1.67 liters
TS-W261S4	25 cm	350 W	1 200 W	4 Ω	93 dB ±1.5 dB (in car, input : 1 W)	20 Hz To 125 Hz (−20 dB in car, input : 1 W)	1 700 g	1.22 liters
TS-W261D4	25 cm	350 W	1 200 W	dual 4 Ω	93 dB ±1.5 dB (in car, input : 1 W)	20 Hz To 125 Hz (−20 dB in car, input : 1 W)	1 700 g	1.22 liters

Revc (Ω)	Levc (mH)	Fs (Hz)	Qms	Qes	Qts	Vas (liters)	Rms (N.S/m)	Mms (g)	Cms (m/N)	Diam (mm)	BL (T.m)	Xmax (mm)
3.0	2.87	42	14.96	0.84	0.79	37.5	2.88	164	8.7×10^{-5}	257	13.0	8.0
dual 2.9	4.85 (8 Ω) 1.23 (2 Ω)	43	13.79	1.02	1.05	32.7	3.39	166	7.6×10^{-5}	257	16.2 (8 Ω) 8.2 (2 Ω)	10.8
3.2	2.92	45	14.59	0.90	0.85	18.6	2.42	124	9.9×10^{-5}	211	11.5	9.3
dual 3.3	4.91 (8 Ω) 1.26 (2 Ω)	46	15.49	1.12	1.04	17.7	2.33	123	9.5×10^{-5}	211	15.3 (8 Ω) 7.7 (2 Ω)	10.1

Appendix D Shaker motors

2 poles Three-phase electric vibrators - 3000/3600 rpm

DESCRIPTION			MECHANICAL SPECIFICATIONS						ELECTRICAL SPEC.				DIMENSIONAL SPECIFICATIONS																	
			STATIC MOMENT		CENTRIFUGAL FORCE				MAX. INPUT POWER (W)		MAX. INPUT CURRENT (A)		Weight (kg.)			Fixing distances				Fixing holes									
			kgmm		kg.f		kN				400V	460V																	
Code	Type	Size	50Hz	60Hz	50Hz	60Hz	50Hz	60Hz	50Hz	60Hz	50Hz	60Hz	50Hz	60Hz	Ref	A	B	C	D	E	ØF	N°	G	H	I	L	M	N	O	Cable gland
V2001	VV03N/2	BA	12	7,5	120	110	1,18	1,08	170	170	0,33	0,29	5,8	5,6	2	62-74	106	216	125	30,5	9	4	24	23	93	154	129	64	50	PG13,5
V2002	VV05N/2	BA	20	13	205	190	2,01	1,86	170	170	0,33	0,29	6,3	5,9	2	62-74	106	216	125	30,5	9	4	24	23	93	154	129	64	50	PG13,5
V2003	VV10N/2	CA	32	21	320	310	3,14	3,04	250	260	0,57	0,48	9,7	9,2	2	90	125	243	152	28,5	13	4	28	30	93	178	144	73	54	PG13,5
V2004	VV15N/2	DA	52	34	520	490	5,10	4,81	430	470	0,76	0,71	14,8	13,8	2	105	140	273	167	32	13	4	28,5	30	111	204	163	80	62,5	PG16
V2005	VV25N/2	EA	80	53	800	770	7,85	7,55	610	650	1,00	0,95	21	20	2	120	170	308	205	38	17	4	40	33	111	214,5	191	91,5	63	PG16
V2012	VV35N/2	GA	114	76	1150	1100	11,3	10,8	950	1100	1,60	1,60	37	36	2	120	170	436	210	60	17	4	22	47,5	111	243	223	115,5	118	PG16
V2006	VV38N/2	IB	159	104	1600	1500	15,7	14,7	1900	1900	3,20	2,80	43	41,5	2	140	190	422	230	81,5	17	4	22	45	111	235	224	104	83,5	PG16
V2007	VV40N/2	IB	234	155	2350	2250	23,1	22,1	2100	2100	3,40	2,90	53	51,5	2	140	190	458	230	81,5	17	4	22	45	111	235	224	104	101,5	PG16
V2008	VV45N/2	MA	324	220	3250	3200	31,9	31,4	3800	3800	6,20	5,40	105	101	2	155	255	590	310	103,5	23,5	4	30	60	155	335	309	160	140	PG21
V2009	VV55N/2	MA	399	261	4000	3800	39,2	37,3	3800	3800	6,20	5,40	110	103	2	155	255	590	310	103,5	23,5	4	30	60	155	335	309	160	140	PG21
V2013	VV67N/2	OA	636	445	6400	6450	62,8	63,3	5300	5300	8,80	7,70	188	181	2	200	320	662	390	111	28	4	32	75	155	381	384	189	151	PG21
V2011	VV71N/2	PA	895	621	9000	9000	88,3	88,3	9400	8800	17,0	12,3	217	211	2	200	320	624	392	111	28	4	35	75	155	403	402	199,5	132	PG21

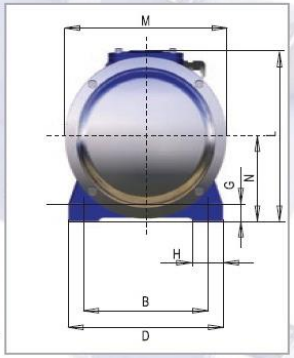

4 poles Three-phase electric vibrators - 1500/1800 rpm

DESCRIPTION			MECHANICAL SPECIFICATIONS						ELECTRICAL SPEC.				DIMENSIONAL SPECIFICATIONS																	
			STATIC MOMENT		CENTRIFUGAL FORCE				MAX. INPUT POWER (W)		MAX. INPUT CURRENT (A)		Weight (kg.)			Fixing distances				Fixing holes									
			kgmm		kg.f		kN				400V	460V																	
Code	Type	Size	50Hz	60Hz	50Hz	60Hz	50Hz	60Hz	50Hz	60Hz	50Hz	60Hz	50Hz	60Hz	Ref	A	B	C	D	E	ØF	N°	G	H	I	L	M	N	O	Cable gland
V4000	VV03B/4	BA	14,0	11,6	35	42	0,343	0,412	80	90	0,20	0,19	6,0	6,0	2	62-74	106	216	125	30,5	9	4	24	23	93	154	129	64	50	PG13,5
V4001	VV05B/4	BA	32,0	22,1	80	80	0,785	0,785	80	90	0,20	0,19	6,6	6,4	2	62-74	106	216	125	30,5	9	4	24	23	93	154	129	64	50	PG13,5
V4002	VV10B/4	CA	87,0	60,8	220	220	2,16	2,16	160	160	0,38	0,38	12,5	11,5	2	90	125	295	152	28,5	13	4	28	30	93	178	144	73	80	PG13,5
V4003	VV20B/4	DA	167	116	420	420	4,12	4,12	280	330	0,57	0,57	19	18	2	105	140	340	167	32	13	4	28,5	30	111	204	163	80	96	PG16
V4004	VV30B/4	EA	298	215	750	780	7,36	7,65	500	620	0,88	0,93	28	26	2	120	170	376	205	38	17	4	40	33	111	214,5	191	91,5	97	PG16
V4005	VV35B/4	GA	437	276	1100	1000	10,8	9,81	520	640	0,90	0,90	45,5	41	2	120	170	436	210	60	17	4	22	47,5	111	243	223	115,5	118	PG16
V4006	VV38B/4	HA	556	387	1400	1400	13,7	13,7	850	1000	1,37	1,43	55	52	2	140	190	438	230	72	17	4	25	45	111	257	241	124,5	103	PG16
V4007	VV40B/4	IA	714	483	1800	1750	17,7	17,2	1100	1200	1,91	1,83	61	57	2	140	190	486	230	72	17	4	25	45	111	257	241	124,5	127	PG16
V4016	VV41B/4	IA	833	566	2100	2050	20,6	20,1	1300	1400	2,40	2,20	72	70	2	140	190	557	230	72	17	4	25	45	111	257	241	124,5	162,5	PG16
V4008	VV50B/4	LA	992	691	2500	2500	24,5	24,5	1500	1600	3,00	2,90	85	79	2	155	225	522	275	79,5	22	4	28	55	111	283	271	140	129,5	PG16
V4017	VV53B/4	LA	1250	870	3150	3150	30,9	30,9	1800	1900	3,60	3,30	95	92	2	155	225	600	275	79,5	22	4	28	55	111	283	271	140	168,5	PG16
V4009	VV55B/4	MA	1508	1050	3800	3800	37,3	37,3	2100	2400	3,80	3,70	118	113	2	155	255	590	310	103,5	23,5	4	30	60	155	335	309	160	140	PG16
V4018	VV57B/4	MA	1746	1188	4400	4300	43,2	42,2	2400	2700	4,60	4,40	125	120	2	155	255	658	310	103,5	23,5	4	30	60	155	335	309	160	174	PG21
V4010	VV60B/4	NA	1984	1367	5000	4950	49,1	48,6	3400	3200	5,70	4,80	174	166	2	180	280	638	340	106	26	4	30	65	155	369	336	173	154	PG21
V4011	VV67B/4	OA	2619	1823	6600	6600	64,7	64,7	5700	5700	10,0	8,60	212	200	2	200	320	662	390	111	28	4	32	75	155	381	384	189	151	PG21
V4012	VV71B/4	PA	3175	2210	8200	8200	80,4	80,4	6600	7600	11,0	10,9	228	213	2	200	320	624	392	111	28	4	35	75	155	403	402	199,5	132	PG21
V4013	VV81B/4	QA	3373	2486	8600	9000	83,4	88,3	7100	8000	11,5	11,3	319	305	3	125	380	862	460	70	39	6	35	95	170	434,5	439	215	230	PG21

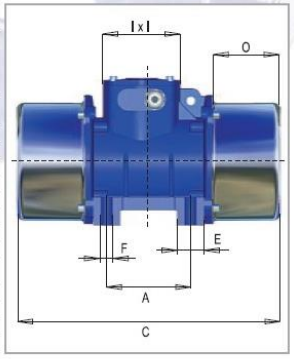

Certifications

Standard CSA C 22.2n° 100-95, file n° 216103, Class 4228 01; Class 1, Division 2, Groups A, B, C and D. Vibrators for use in hazardous locations

Standard CSA C 22.2n° 100-95, file n° 216103, Class 4211 01, Motors and generators

II 2G, D-Class EEx e II T4 and T3 - CENELEC EN 50014 - EN 50281.1.1 Certificate n° LCIE 02 ATEX 6129 X - European Directive 94/9/CE - Increased safety vibrators for potentially explosive gas atmosphere and combustible atmosphere.

II 2 D 120 °C (Operating temperture 40°C) 135°C (Operating temperature 55°C) CENELEC EN n° LCIE 03 ATEX 6067 X - European Directive 94/9/CE (ATEX) Electric vibrators for combustible dusts atmospheres.

Production quality assurance notification. (Directive 94/9/CE) n° CESI 02 ATEX 112 Q.

Appendix E Coil springs

SPRING CENTRE & ENG.

T/A Hi-Grade Spring works

674 Barlow Street
Germiston South
Telephone (011) 873 2512
(011) 873 2845 / 2851

P O Box 1554
Alberton 1450
Fax (011) 825 7669
E-mail: higrade@icon.co.za

TEST CERTIFICATE

Customer : Noordwes universiteit Date: 29 July 2019
Delivery note / Invoice: _____ Order No: _____

HEAT TREATMENT

This is to certify that the spring/s have been oil quenched and tempered (stress relieved), Salt bath curing, at a temperature of 320 centigrade for a time period of 10 min/ hrs Rockwell hardness _____.

MEASURING INSTRUMENTS

Vernier X Manual Testing Scale X Scragg Test X

Load – P1 13KG Deflection 10 mm
Load – P2 26 KG Deflection 20 mm

12753 N/m
design: 13587 N/m

MATERIAL CERTIFICATE
YES / NO

MATERIAL SPECIFICATION
_____

SPRING DETAILS

Material Diameter 6mm
Outside Diameter 60
Inside Diameter 48 mm
Length 100 mm
Number of Coils 8
Finish Square & Grind
Type comps
Drawing / Part No _____
Quantity Ordered 6
Job Card No 92957